

AD-A227 978

## REPORT DOCUMENTATION PAGE

Form Approved  
OMB No. 0704-0188

Public reporting burden for this collection of information is estimated to average 1 hour per response, including the time for reviewing instructions, searching existing data sources, gathering and maintaining the data needed, and completing and reviewing the collection of information. Send comments regarding this burden estimate or any other aspect of this collection of information, including suggestions for reducing this burden, to Washington Headquarters Services, Directorate for Information Operations and Outputs, 121 Jefferson Davis Highway, Suite 1204, Arlington, VA 22202-4302, and to the Office of Management and Budget's Paperwork Reduction Project (0704-0188), Washington, DC 20503.

1. AGENCY USE ONLY (Leave blank)	2. REPORT DATE	3. REPORT TYPE AND DATES COVERED	
	1990	THESIS/DISSERTATION	
4. TITLE AND SUBTITLE Wave-Mean Flow Interaction in the Storm-Time Thermosphere Using a Two-Dimensional Model		5. FUNDING NUMBERS	
6. AUTHOR(S) Douglas George Brinkman			
7. PERFORMING ORGANIZATION NAME(S) AND ADDRESS(ES) AFIT Student Attending: University of California, Los Angeles		8. PERFORMING ORGANIZATION REPORT NUMBER AFIT/CI/CIA- 90-24D	
9. SPONSORING/MONITORING AGENCY NAME(S) AND ADDRESS(ES) AFIT/CI Wright-Patterson AFB OH 45433-6583		10. SPONSORING, MONITORING AGENCY REPORT NUMBER	
11. SUPPLEMENTARY NOTES			
12a. DISTRIBUTION/AVAILABILITY STATEMENT Approved for Public Release IAW 190-1 Distributed Unlimited ERNEST A. HAYGOOD, 1st Lt, USAF Executive Officer		12b. DISTRIBUTION CODE	
13. ABSTRACT (Maximum 200 words)			
14. SUBJECT TERMS		15. NUMBER OF PAGES 107	
16. PRICE CODE			
17. SECURITY CLASSIFICATION OF REPORT	18. SECURITY CLASSIFICATION OF THIS PAGE	19. SECURITY CLASSIFICATION OF ABSTRACT	20. LIMITATION OF ABSTRACT

90 11 1 065

## GENERAL INSTRUCTIONS FOR COMPLETING SF 298

The Report Documentation Page (RDP) is used in announcing and cataloging reports. It is important that this information be consistent with the rest of the report, particularly the cover and title page. Instructions for filling in each block of the form follow. It is important to stay *within the lines* to meet optical scanning requirements.

Block 1 <u>Agency Use Only (Leave blank)</u>	Block 12a. <u>Distribution/Availability Statement</u>
Block 2. <u>Report Date</u> . Full publication date including day, month, and year, if available (e.g. 1 Jan 88). Must cite at least the year.	Denotes public availability or limitations. Cite any availability to the public. Enter additional limitations or special markings in all capitals (e.g. NOFORN, REL, ITAR).
Block 3. <u>Type of Report and Dates Covered</u> . State whether report is interim, final, etc. If applicable, enter inclusive report dates (e.g. 10 Jun 87 - 30 Jun 88).	DOD - See DoDD 5230.24, "Distribution Statements on Technical Documents." DOE - See authorities. NASA - See Handbook NHB 2200.2. NTIS - Leave blank.
Block 4. <u>Title and Subtitle</u> . A title is taken from the part of the report that provides the most meaningful and complete information. When a report is prepared in more than one volume, repeat the primary title, add volume number, and include subtitle for the specific volume. On classified documents enter the title classification in parentheses.	Block 12b. <u>Distribution Code</u> .
Block 5. <u>Funding Numbers</u> . To include contract and grant numbers; may include program element number(s), project number(s), task number(s), and work unit number(s). Use the following labels:	DOD - Leave blank. DOE - Enter DOE distribution categories from the Standard Distribution for Unclassified Scientific and Technical Reports. NASA - Leave blank. NTIS - Leave blank.
Block 6. <u>Author(s)</u> . Name(s) of person(s) responsible for writing the report, performing the research, or credited with the content of the report. If editor or compiler, this should follow the name(s).	Block 13. <u>Abstract</u> . Include a brief ( <i>Maximum 200 words</i> ) factual summary of the most significant information contained in the report.
Block 7. <u>Performing Organization Name(s) and Address(es)</u> . Self-explanatory.	Block 14. <u>Subject Terms</u> . Keywords or phrases identifying major subjects in the report.
Block 8. <u>Performing Organization Report Number</u> . Enter the unique alphanumeric report number(s) assigned by the organization performing the report.	Block 15. <u>Number of Pages</u> . Enter the total number of pages.
Block 9. <u>Sponsoring/Monitoring Agency Name(s) and Address(es)</u> . Self-explanatory.	Block 16. <u>Price Code</u> . Enter appropriate price code ( <i>NTIS only</i> ).
Block 10. <u>Sponsoring/Monitoring Agency Report Number</u> . ( <i>If known</i> )	Blocks 17. - 19. <u>Security Classifications</u> . Self-explanatory. Enter U.S. Security Classification in accordance with U.S. Security Regulations (i.e., UNCLASSIFIED). If form contains classified information, stamp classification on the top and bottom of the page.
Block 11. <u>Supplementary Notes</u> . Enter information not included elsewhere such as. Prepared in cooperation with..., Trans. of..., To be published in.... When a report is revised, include a statement whether the new report supersedes or supplements the older report.	Block 20. <u>Limitation of Abstract</u> . This block must be completed to assign a limitation to the abstract. Enter either UL (unlimited) or SAR (same as report). An entry in this block is necessary if the abstract is to be limited. If blank, the abstract is assumed to be unlimited.

UNIVERSITY OF CALIFORNIA

Los Angeles

Wave-Mean Flow Interaction in the Storm-Time Thermosphere  
Using a Two-Dimensional Model

A dissertation submitted in partial satisfaction of the  
requirements for the degree Doctor of Philosophy  
in Atmospheric Sciences

by

Douglas George Brinkman

1990

The dissertation of Douglas George Brinkman is approved

Arthur D. Richmond

Arthur D. Richmond

Richard L. Walterscheid

Richard L. Walterscheid

Robert L. McPherson

Robert L. McPherson

David A. Paige

David A. Paige

Richard M. Thorne

Richard M. Thorne

Richard P. Turco

Richard P. Turco

S. V. Venkateswaran

S. V. Venkateswaran, Committee Chair



University of California, Los Angeles

1990

Accession For	
NTIS	GRA&I <input checked="" type="checkbox"/>
DTIC TAB	<input type="checkbox"/>
Unannounced	<input type="checkbox"/>
Justification _____	
By _____	
Distribution/ _____	
Availability Codes	
Dist	Avail and/or Special
A-1	

This dissertation is dedicated to my Grandmother:

Mildred Ramsdale

Who always gave me encouragement and support during my studies at

UCLA

## TABLE OF CONTENTS

CHAPTER	I. INTRODUCTION	1
	Figure Captions	5
	Figures	6
CHAPTER	II. TWO-DIMENSIONAL THERMOSPHERIC MODEL	8
2.1	Model Equations	8
2.2	Model Description and Boundary Conditions	11
2.3	Model Initialization	12
2.4	Storm Simulation Conditions	15
	Figure Captions	17
	Figures	19
CHAPTER	III. STORM SIMULATION RESULTS	32
3.1	Evolution of Storm-Time Winds and Temperatures	32
3.2	Influence of Background Seasonal Winds and Temperatures on Mean Storm-Time Winds and Temperatures	34
3.3	Characteristics of Storm-Generated Wave Disturbances	36
3.4	Influence of Background Winds and Temperatures	39
3.5	Vertical Structure of the Wave Disturbances	42
3.6	Wave-Induced Heat and Momentum Fluxes	43

Figure Captions	46
Figures	48
CHAPTER IV. WAVE-MEAN FLOW INTERACTION	71
4.1 Effects On Circulation	71
4.2 Heat Sources and Sinks	75
Figure Captions	79
Figures	80
CHAPTER V. LAGRANGIAN MOTIONS, EULERIAN MOTIONS, AND STOKES DRIFT	86
5.1 Trajectory Calculations	86
5.2 Stokes Relations	88
Figure Captions	91
Figures	93
CHAPTER VI. DISCUSSION AND CONCLUSIONS	98
REFERENCES	101

## FIGURE LIST

Figure 1.1a. Typical thermospheric parameters: Temperature and air density.	6
Figure 1.1b. Typical thermospheric parameters: Coefficients of molecular viscosity and thermal conductivity.	7
Figure 2.1. Global mean temperature.	19
Figure 2.2. $Q_s$ , departure from the global mean heating rate and quiet-time high-latitude heating.	20
Figure 2.3a. Time history of temperature changes as system runs to steady-state.	21
Figure 2.3b. Time history of meridional winds as system runs to a steady-state.	22
Figure 2.3c. Time history of zonal winds as system runs to a steady-state.	23
Figure 2.4a. Steady-state solstitial temperature field and its difference from the global mean temperature.	24
Figure 2.4b. Background meridional winds.	25
Figure 2.4c. Background zonal winds.	26
Figure 2.5a. Estimated hemispheric energy inputs for the geomagnetic storms of 22 March 1979 and 13-14 March 1989.	27
Figure 2.5b. Energy input for model storm.	28
Figure 2.6a. Example of a Joule heating distribution pattern.	29
Figure 2.6b. Normalized colatitude heating profile for the model storm.	30

Figure 2.7. Normalized altitude heating profile for the model storm.	31
Figure 3.1a. Storm-time meridional winds at 2 hours.	48
Figure 3.1b. Storm-time meridional winds at 3 hours.	49
Figure 3.1c. Storm-time meridional winds at 7 hours.	50
Figure 3.1d. Storm-time meridional winds at 11 hours.	51
Figure 3.2a. Storm-time temperatures at 2 hours.	52
Figure 3.2b. Storm-time temperatures at 3 hours.	53
Figure 3.2c. Storm-time temperatures at 7 hours.	54
Figure 3.2d. Storm-time temperatures at 11 hours.	55
Figure 3.3a. Time-averaged storm-time meridional winds for model run with background winds and associated temperatures.	56
Figure 3.3b. Time-averaged storm-time meridional winds for model run without background winds and associated temperatures.	57
Figure 3.3c. Time-averaged storm-time zonal winds for the model run with background winds and associated temperatures.	58
Figure 3.3d. Time-averaged storm-time zonal winds for the model run without background winds and associated temperatures.	59
Figure 3.4a. Time-averaged storm-time temperatures for the model run with background winds and associated temperatures.	60

Figure 3.4b. Time-averaged storm-time temperatures for the model run without background winds and associated temperatures.	61
Figure 3.5a. Disturbances in vertical velocity.	62
Figure 3.5b. Disturbances in meridional velocity.	63
Figure 3.6. Influence of solstitial background winds and temperatures on disturbance propagation.	64
Figure 3.7. Background solstitial meridional winds.	65
Figure 3.8a. Vertical structure of disturbances as shown by vertical velocity response and temperature change.	66
Figure 3.8b. Vertical structure of disturbances as shown by meridional velocity and temperature change.	67
Figure 3.9a. Vertical heat flux.	68
Figure 3.9b. Meridional heat flux.	69
Figure 3.9c. Vertical flux of meridional momentum.	70
Figure 4.1. Mean linear circulation.	80
Figure 4.2. Mean induced circulation.	81
Figure 4.3. Heat sources and sinks due to the mean Eulerian circulation.	82
Figure 4.4. Heat sources and sinks due to the mean linear circulation.	83
Figure 4.5. Heat sources and sinks due to the mean induced circulation.	84
Figure 4.6. Heat sources and sinks due to the mean eddy heat flux convergences (divergences).	85

Figure 5.1. Trajectory of fluid marker influenced by storm-generated waves alone.	93
Figure 5.2a. Trajectory of fluid marker during the period of passage of the first storm-generated wave.	94
Figure 5.2b. Trajectory of fluid marker during the period of passage of the first two waves.	95
Figure 5.3a. Examples of Lagrangian and Eulerian trajectories for storm-generated waves and circulation.	96
Figure 5.3b. Examples of Lagrangian and Eulerian trajectories including also background winds.	95

#### ACKNOWLEDGEMENTS

This dissertation would not have been completed without the help of many people.

First, I would like to thank my advisor and friend Dr. S.V. Venkateswaran (Ven.i) whose encouragement and guidance has kept me on track for the last 4.5 years. I also wish to thank Dr(s). Richard Walterscheid and Art Richmond for their immense guidance, help and friendship during this study.

In addition, I would like to thank Dr(s). Bob McPherron, David Paige, Richard Thorne, and Richard Turco for serving on my committee and providing useful comments that improved this dissertation. Also, I thank Dr. Christine Mazaudier for getting me involved in thermospheric research.

I am grateful to the United States Air Force for the time and financial support necessary to complete this work. In addition, I would like to acknowledge use of the following non-copyrighted material: Figure 2.6a from Knipp (1989).

Special thanks to my office mates (and friends) Tim Alsruhe, Dr. Delores Knipp, Kevin Lunn, and Tim Springer, who kept my spirits up and put up with me. Also, thanks to Tom Christian, Fabrice Cuq, Dr. John Farrara, Randy Fix, Penny Kuhn, David Kratz, Kurt and Joyce Moore, L.V. Oliver, Anna Orrhede, Wes Radlein, Marty Ralph, Tammy Weckwerth, and Clara Wong for their friendship and support.

And finally, I would like to give thanks for my "West Coast Family"

at the West Los Angeles Methodist Church (especially, the Choir, Virtue Ishihara, Jeanie Takeshita, Ken Ho, Steve and Marilyn Fujii, Naoto Tashiro, Stan Morita, Sue Seto, and Rev. Se Hee Han) for their encouragement, support, and Love.

ABSTRACT OF THE DISSERTATION

Wave-Mean Flow Interaction in the Storm-Time Thermosphere  
Using a Two-Dimensional Model

by

Douglas George Brinkman

Doctor of Philosophy in Atmospheric Sciences  
University of California, Los Angeles, 1990

Professor S. V. Venkateswaran, Chair

A two-dimensional pole-to-pole numerical model with background solstitial winds has been used to study the global dynamical response of the thermosphere to high-latitude energy inputs associated with a model geomagnetic storm. This model storm, consisting of a series of substorms, has four distinct pulses of heat input over a 12-hr period.

The storm generated six groups of wave disturbances in the form of internal gravity waves. Characteristics of these disturbances such as their vertical structure, phase propagation speeds, and influences of dispersion and dissipation are illustrated. The disturbances in the velocity field and in the temperature field are shown, along with their mutual phase relationship with regard to the meridional and vertical transport of heat and momentum.

In addition to the generation of disturbances, the thermospheric response to the sustained part of the heat input is to consist of the establishment of a global meridional circulation which is initiated in about 3 to 4 hours after storm commencement and never quite reaches steady-state in the simulation. The time development of this circulation and its associated temperature field are described.

The main purpose of this study is to investigate the interaction between the disturbances and the mean flow associated with the storm. It is shown that this interaction can be represented in terms of an induced circulation. This induced circulation is forced by the time-dependent nature of the eddy flux convergences (divergences) of heat and momentum. The influence of this induced circulation is detectable most noticeably in the heat sources and sinks set up by the Eulerian mean circulation. At altitudes above 150 km, in the equatorial region, the equivalent temperature changes due to such sources and sinks resulting from the induced circulation are 1/3 to 1/4 of the changes due to the Eulerian mean circulation.

Spatial and temporal variations of the storm-time winds are responsible for the differences between Lagrangian and mean Eulerian trajectories. Trajectory calculations also, show that fluid material transported from the source regions does not reach equatorial latitudes. However, storm-generated waves, reaching the equator within three hours of storm onset, initiate fluid motions at low-latitudes

CHAPTER I  
INTRODUCTION

The thermosphere is a region of low air density, and high values of thermal conductivity, molecular viscosity, and static stability (Figures 1.1a and 1.1b). In particular, it is a region characterized by its quick dynamic response to energy inputs. A major source of energy for the thermosphere is solar radiation in EUV and UV wavelengths, which is variable with solar cycle, season, and time of day. In addition, there is an important source of energy at high latitudes resulting from the dissipation of electrical currents in the auroral region and, to a lesser extent, from the precipitation of energetic particles (Banks, 1977). This high-latitude energy source is believed to be present at all times, but its strength increases considerably during geomagnetic storms. (Killeen, 1987; Richmond, 1983; Roble, 1977.)

The global dynamic response of the thermosphere during geomagnetic storms has been the subject of considerable interest. Earlier studies have indicated that this response consists of several parts: 1) A localized zonal jet with associated vertical circulations in the region of intensified auroral currents. The zonal jet arises as a result of collisions of electrically neutral air molecules with ions which are, in turn, accelerated by polar cap electric fields. Such electric fields are generated by magnetospheric convection and mapped onto the ionosphere along highly conducting geomagnetic field lines. Killeen et. al., 1984; Killeen et. al., 1986; Larsen and Mikkelsen, 1983;

Mikkelsen et. al., 1981; Walterscheid and Boucher, 1984). 2) Internal gravity waves, generated especially in the initial phases of a storm and propagating to low latitudes (Francis, 1975; Georges, 1968; Hernandez and Roble, 1978; Hines, 1960, 1974; Hunsucker, 1982; Richmond, 1978, 1979a; Rees et. al., 1984; Roble et. al., 1978; Testud, 1970). 3) A global meridional circulation driven by the sustained heating maintained at high latitudes (Babcock and Evans, 1979; Buonsanto et. al., 1989; Burnside et. al. 1983; Crowley et. al., 1989b; Hays and Roble, 1971; Hernandez and Roble, 1976, 1984; Mazaquier et. al., 1985).

These dynamical responses have been studied using both two- and three-dimensional models. Dickinson et. al. (1975, 1977), and Roble et. al. (1977), used a time-dependent two-dimensional model to obtain the steady-state circulation forced by solar heating and high-latitude heating for various levels of magnetic activity. They also investigated the effects of seasonal and solar cycle variations in maintaining the steady-state circulation.

Richmond and Matsushita (1975) used a time-dependent two-dimensional single-hemisphere model to examine the response to an isolated sub-storm. This response consisted primarily of equatorward propagating gravity waves along with strong vertical and zonal winds at high latitudes. In later papers, Richmond (1978, 1979a) used this model to study gravity wave generation, propagation, and dissipation. Furthermore, Richmond (1979b) made a quantitative comparison of heating due to viscous dissipation of gravity waves with heating due to the meridional circulation.

There is increasing recognition in recent years that the full complexity of the storm-time response can only be handled by three-dimensional models. Several studies using models such as the NCAR-TIGCM and UCL-TGCM have become available. (Crowley et. al., 1989a; Dickinson et. al., 1980; Dickinson et. al., 1984; Fuller-Rowell and Rees, 1981; Fuller-Rowell and Rees, 1984; Roble et. al., 1982; Roble et. al., 1983; and Roble et. al., 1987;) However, the results from such models are complex and are not readily interpreted. Consequently, two-dimensional models may still play a complementary role in the diagnostics of specific results from three-dimensional models. Alternatively, they may serve as test-beds for preliminary simulation of physical processes that await inclusion into three-dimensional models.

The present paper is concerned with the nature and importance of wave-mean flow interaction under storm-time conditions, and the consequences of such interaction for the Lagrangian and Eulerian descriptions of the storm-time circulation. The model used is a generalization of the model of Richmond and Matsushita (1975), referred to earlier. The generalization consists of the extension of the model domain from pole-to-pole and the inclusion of seasonal background winds. As a consequence, the model enables us to study solstitial conditions when the winds are hemispherically asymmetric. The influence of such winds on the propagation of storm-induced wave disturbances is an additional interest of this study.

This study of the wave-mean flow interaction for the thermosphere in general and under storm-time conditions, in particular, is believed

to be new. It shows that, although the disturbances generated during the storm are of large amplitude, the phase speeds of the disturbances (~500 m/s) are also large compared to the background wind speeds (50 m/s) so that critical levels (where the phase speeds match the background wind speeds) are not encountered in the thermosphere. This is in contrast to the situation at lower levels in the atmosphere where most wave-mean flow interactions occur at such locations (Booker and Bretherton, 1967). However, other favorable conditions for the interactions, like wave transience and dissipative effects (which increase rapidly with height), are available in the thermosphere. The strength of the interactions is, nevertheless, moderated by the large vertical and horizontal scales of the disturbances.

The layout of the rest of the dissertation is as follows: In Chapter 2 we give model details, closely following the work of Richmond and Matsushita. Chapter 3 presents several model results of the global circulation and of the waves resulting from our storm model. Chapter 4 deals with wave-mean flow interactions. Chapter 5 draws a distinction between the Lagrangian and Eulerian mean circulations and gives examples of Stokes drift calculations for several locations. Finally, Chapter 6 summarizes the major conclusions of this study.

FIGURE CAPTIONS FOR CHAPTER I

FIG. 1.1. Typical thermospheric parameters: a) Temperature ('K) (solid line) and log density (KG/M<sup>3</sup>) (dashed line). b) Coefficient of molecular viscosity (X10<sup>-5</sup> KG/MS) (solid line) and coefficient of molecular thermal conductivity (X10<sup>-2</sup> W/M°K) (dashed line). All from Richmond and Matsushita (1975), Table 1.

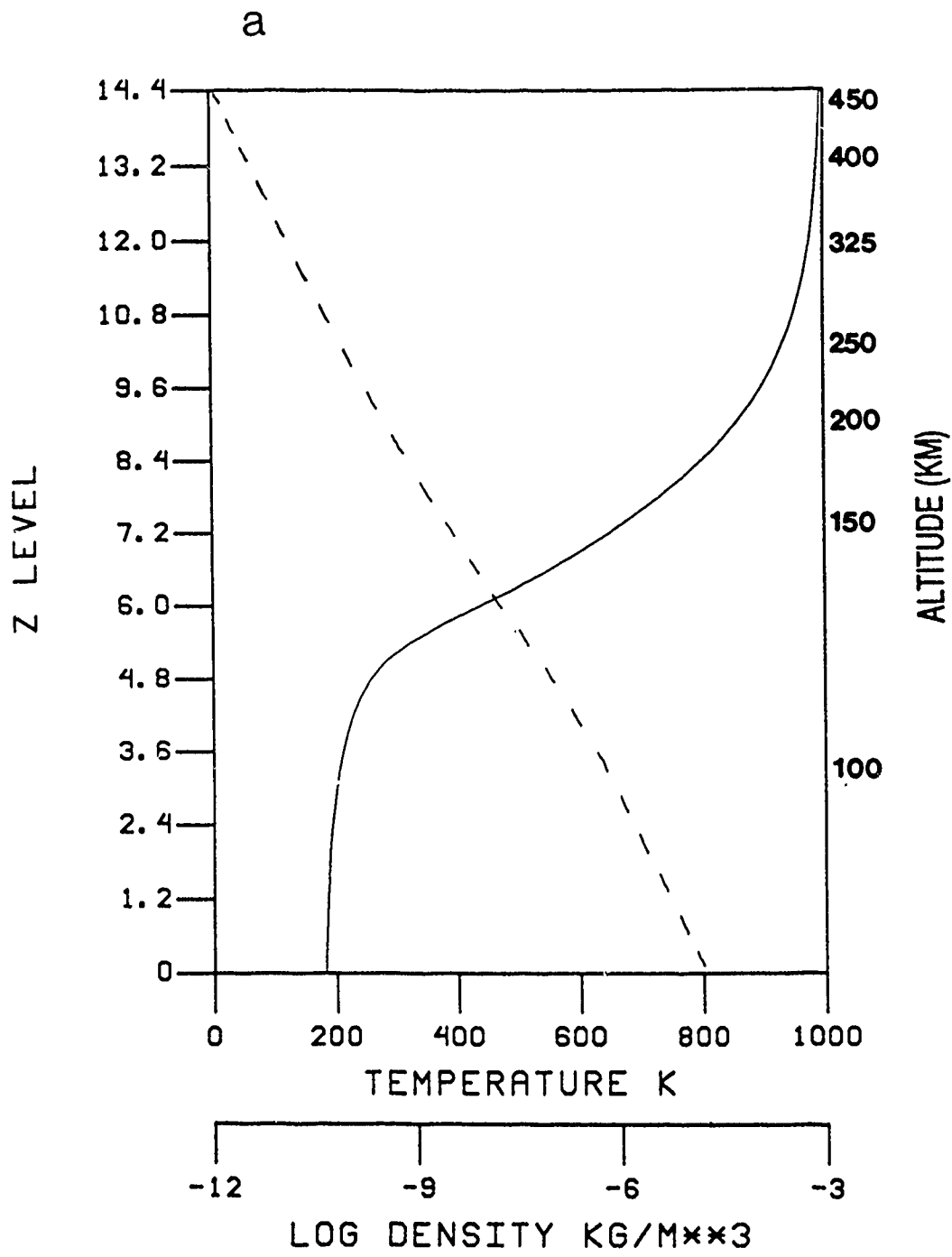


Figure 1.1a

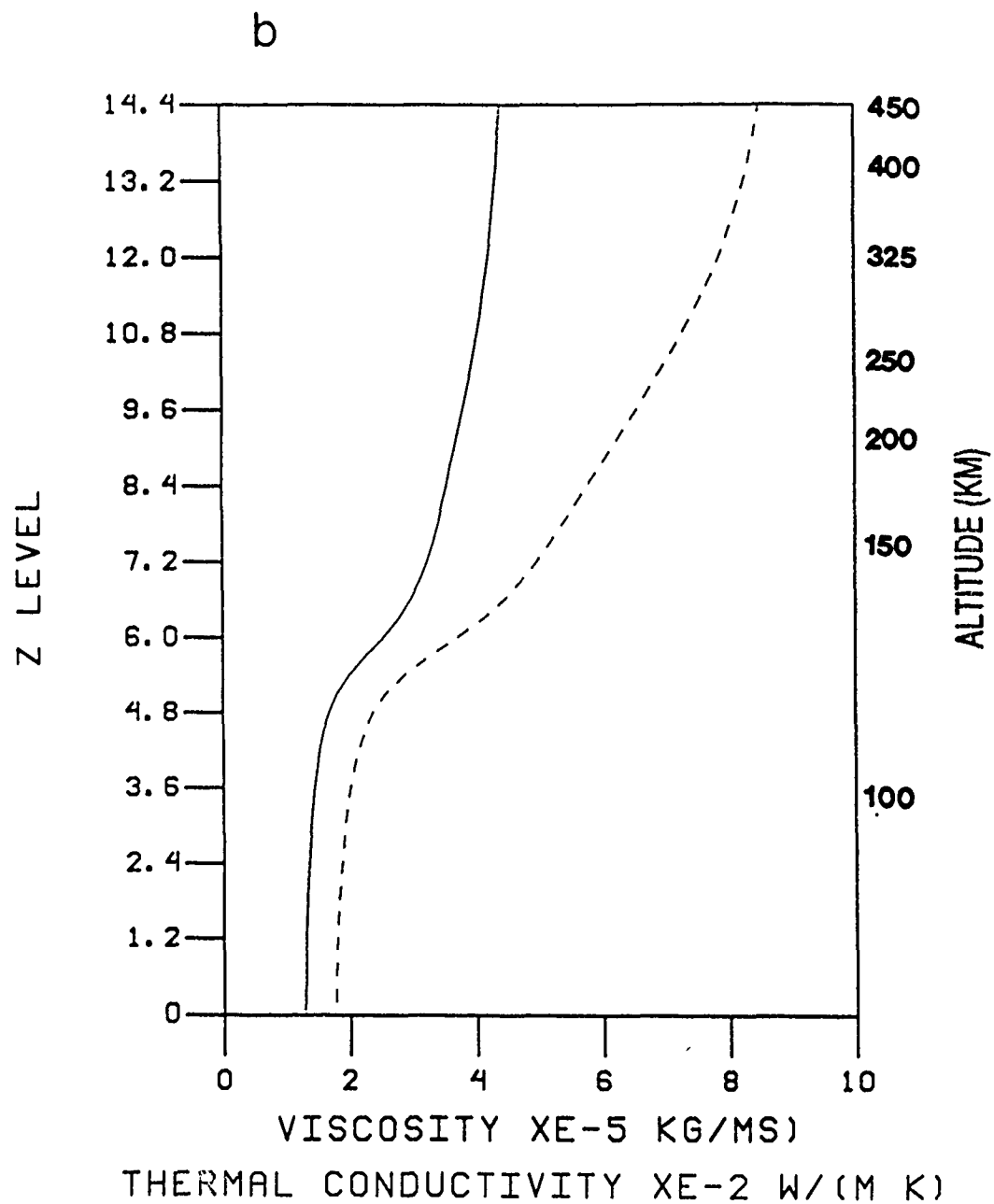


Figure 1.1b

CHAPTER II  
TWO-DIMENSIONAL THERMOSPHERIC MODEL

2.1 MODEL EQUATIONS

As in Richmond and Matsushita (1975), hereafter abbreviated as RM, our model equations written in the log-pressure coordinate system are:  
Zonal momentum equation:

$$\frac{DV_\phi}{Dt} = - \left( 2\Omega \cos\theta + \frac{V_\phi}{a} \cot\theta \right) v_\theta + X \quad (2.1)$$

Meridional momentum equation:

$$\frac{DV_\theta}{Dt} = - \frac{1}{a} \frac{\partial \Phi}{\partial \theta} + \left( 2\Omega \cos\theta + \frac{V_\phi}{a} \cot\theta \right) v_\phi + Y \quad (2.2)$$

Hydrostatic equation:

$$\frac{\partial \Phi}{\partial z} = RT \quad (2.3)$$

Continuity equation:

$$\frac{1}{a \sin\theta} \frac{\partial}{\partial \theta} (v_\theta \sin\theta) + \frac{1}{p} \frac{\partial}{\partial z} (p_w) = 0 \quad (2.4)$$

Thermodynamic energy equation:

$$\frac{D}{Dt} (C_p T) + R w T = Q + K \quad (2.5)$$

and the Equation of State:

$$p = \rho \frac{\partial \Phi}{\partial z} = \rho g H \quad (2.6)$$

The meanings of symbols in the model equations are:

- a = radius of earth.  
g = gravity  $9.81 \text{ m/s}^2$ .  
p = pressure.  
 $p_s$  = reference pressure at 80 km ( $1.031 \text{ Pa}$ ).  
t = time  
 $w \equiv \frac{dz}{dt}$ , a measure of vertical velocity, positive upward.  
z = height.  
 $C_p$  = specific heat at constant pressure.  
H = scale-height ( $RT/g$ ).  
R = gas constant.  
T = temperature.  
 $(V_\phi, V_\theta)$  = (zonal, meridional) velocity.  
w = vertical velocity (in m/s)  
z = log-pressure coordinate,  $\ln(p_s/p)$ .  
 $\rho$  = density.  
 $(\phi, \theta)$  = (longitude, colatitude).  
 $\Omega$  = angular velocity of the earth.  
 $\Phi$  = geopotential ( $gz$ ) and  $\frac{\partial \Phi}{\partial z} = RT$ .

and

$$\frac{D}{Dt} = \frac{\partial}{\partial t} + \frac{v_\theta}{a} \frac{\partial}{\partial \theta} + w \frac{\partial}{\partial z} .$$

In addition, X and Y in the momentum equations are:

$$X = - \frac{1}{p} \frac{\partial}{\partial z} ( g \tau_\phi ) - I_\phi$$

and

$$Y = - \frac{1}{p} \frac{\partial}{\partial z} ( g \tau_\theta ) + I_\theta$$

where

$$( \tau_\phi, \tau_\theta ) = - \left( \frac{\mu_m + \mu_t}{H} \right) \frac{\partial}{\partial z} ( v_\phi, v_\theta )$$

and

$$( I_\phi, I_\theta ) = \text{Ion drag in the } (\phi, \theta) \text{ directions.}$$

In the above,  $\mu_m$  and  $\mu_t$  are coefficients of molecular and eddy viscosity, respectively. A typical value of  $\mu_m + \mu_t$  at 250 km (middle thermosphere) is  $4.0 \times 10^{-5}$  kg/(m s). Values at other heights are obtained from Table 1 of RM (p.2841).

In calculating the ion drag, the model assumes that the ions are not influenced by electric fields of magnetospheric or ionospheric origin. They do, however, collide with neutrals and provide a retard-

ing force on air motion.

Similarly, in the thermodynamic energy equation:

$$Q = Q_0 + Q_S + Q_A$$

and

$$K = -\frac{1}{p} \frac{\partial}{\partial z} (gq)$$

with

$$q = -\frac{\kappa_m}{C_p H} \frac{\partial}{\partial z} (C_p T) - \frac{\kappa_t}{C_p H} \left( \frac{\partial}{\partial z} (C_p T) + gH \right)$$

where  $Q$  is the diabatic heating rate (per unit mass) split into three parts: global mean ( $Q_0$ ) due to solar heating only; departure from the global mean solar heating plus heating from high-latitude auroral sources ( $Q_S$ ); and storm-time auroral heating ( $Q_A$ ).  $K$  is the heating rate due to thermal conductivity consisting of both molecular (coefficient,  $\kappa_m$ ) and eddy (coefficient,  $\kappa_t$ ) conductivities. A typical value for molecular conductivity at 250 km is .09 W/(m °K). Eddy conductivity is negligible above about 125 km. Values for coefficients of molecular and eddy thermal conduction are shown in Table 1 of RM (p.2841).

## 2.2 MODEL DESCRIPTION AND BOUNDARY CONDITIONS

The model is two-dimensional in altitude and colatitude and extends from 80 km ( $z=0$ ) to 450 km ( $z=14.4$ ) in the vertical, and from the north ( $\theta=0^\circ$ ) to the south ( $\theta=180^\circ$ ) poles in the horizontal. The grid spacing is uniform in the vertical with  $\Delta z=0.3$ . In the horizontal the colatitude spacing varies from 1.2 degrees near the poles (for a more detail-

ed representation of the region of storm-time heating) to 2.4° colatitude near the equator.

The boundary conditions for the model are:

$$v_\phi = v_\theta = 0 \quad \text{at } \theta = 0^\circ \text{ and } 180^\circ .$$

$$w = 0 \quad \text{at } z = 14.4.$$

$$z = 80 \text{ km} \quad \text{at } z = 0.$$

$$T = 180^\circ \text{ K} \quad \text{at } z = 0.$$

The only difference in the boundary conditions of the model from RM is the extension of the model domain from pole-to-pole.

### 2.3 MODEL INITIALIZATION

The model thermosphere is initially at rest and has the global mean temperature field shown in Figure 2.1. As in RM, this temperature field is prescribed according to Jacchia's (1971) model atmosphere with an exospheric temperature of 1000° K. The prescription for the neutral atmospheric composition and for the vertical distribution of electron density is the same as in RM i.e., both are held constant throughout the simulation.

Background wind and temperature fields are generated prior to starting the storm simulation. The global mean heating rate  $Q_0$  is just large enough to maintain the initial temperature field (Figure 2.1) from cooling off due to thermal conduction (see also RM). In addition, the model incorporates EUV and UV solar heating appropriate to the solstitial season and quiet-time high-latitude heating appropriate to solar maximum. Following Dickinson et. al. (1977), the magnitude of

the high-latitude heating was adjusted to be 2.5 times as large in the summer hemisphere as in the winter hemisphere. Figure 2.2 shows the distribution of  $Q_S$  which is the departure from the global mean heating rate. The hemispherical asymmetry in  $Q_S$  arises from the greater amount of sunlight in the summer hemisphere as well as from the assumed asymmetry in high-latitude heating just mentioned.

In quantitative terms,  $Q_S$  is approximately 80% of the values used by Dickinson et. al.(1977). (See Figure 9b of Dickinson et. al., p.189.) It should be noted that  $Q_S$  provides the thermal drive for the quiet-time solstitial circulation.

Using  $Q_S$ , we run the system to a steady-state. This takes approximately 5.5 days of simulation time. Figure 2.3 shows the time histories of: a) the temperature change, b) the meridional winds, and c) the zonal winds at three altitudes at  $40^\circ$  colatitude, as these parameters approach a steady-state. It can be seen that both the temperature and the meridional winds reach steady-state comparatively quickly (within 2 to 3 days) at all altitudes as opposed to the zonal winds which take between 5 to 6 days at the lowest altitudes shown.

Figure 2.4 shows the background temperatures and wind fields at steady-state. Figure 2.4a shows the steady-state temperature field (solid contour) and the difference temperature field (dashed contour), which is the difference between the global mean temperature (Figure 2.1) and the steady-state temperature field. The steady-state temperatures are a result of a balance between solar and high-latitude heating, adiabatic warming, and thermal conduction. The difference tempe-

rature field (dashed contour) shows warming by as much as 200°K above 150 km in the summer hemisphere. However, below 150 km, there is a dipole-like pattern of temperature change with a maximum decrease of 40° K between 150 km and 110 km, and a maximum increase of 40° K below. A dipole-like pattern of the opposite sense exists in the winter hemisphere with a change of  $\pm 60^{\circ}$  K.

Figure 2.4b shows a streamline plot of the meridional wind field. The plot shows rising air at high latitudes in the summer hemisphere. The flow proceeds nearly horizontal towards the winter hemisphere, crossing the equator, and sinking at approximately 140°-150° colatitude. The maximum wind speed of 130 m/s is reached at 30° colatitude at the highest altitudes. A reversed circulation also exists at high latitudes and altitudes in the winter hemisphere. It extends from the pole (180°) to 140-150° colatitude and exhibits a maximum wind speed of 15 m/s. Below 120 km, the winds blow directly from summer to winter hemispheres.

Figure 2.4c shows the zonal winds. Below 150 km, a two-celled pattern develops with maximum winds of 60-70 m/s, westward in the summer hemisphere and eastward in the winter hemisphere. Above 150 km, the zonal winds are considerably weaker. In this region the ion drag force dominates the Coriolis force in the wind balance. The summer hemisphere winds above 150 km maximize at 30 m/s in the westward direction.

Our winds for the quiet-time solstitial circulation are similar to the earlier two-dimensional model results of Dickinson et. al. (1977) as well as the later zonally averaged results from the three-dimen-

sional model results of Dickinson et. al. (1980). However, the magnitudes of our winds are smaller, owing to the fact that our values of  $Q_S$  are also somewhat smaller.

#### ~ \* STORM SIMULATION CONDITIONS

As in Blanc and Richmond (1980), it is assumed that the major source of heat input for our thermospheric storm was due to the Joule dissipation of auroral electrojet currents. Joule dissipation occurs when a current flows perpendicular to the geomagnetic field, but parallel to the electric field. Such currents are known as Pedersen currents and the corresponding component of the ionospheric electrical conductivity is known as the Pedersen conductivity,  $\sigma_1$  (Rishbeth and Garriot, 1969).

In deriving a reasonable storm-time heat input model for our simulations, we have consulted two geomagnetic storms, occurring on 22 March 1979 and 13 March 1989, respectively. These storms were chosen because they showed evidence of oscillations in the auroral activity index (AE) for an extended period. The energy inputs for these storms (Figure 2.5a) were obtained from an empirical relation (Mazaudier et. al., 1987) between the hemispheric Joule heating and the auroral activity index (AE). In this manner, it was found that the energy inputs varied between  $10^{10}$  and  $10^{12}$  Watts with periods of 2-4 hours (typical periods of substorms). The 22 March 1979 storm lasted for 8 hours and the 13 March 1989 storm for 36 hours.

Based on the characteristics of the two storms mentioned above,

the model storm energy input was chosen as shown in Figure 2.5b. The model storm lasts for 12 hours. It shows four oscillations with periods of 2-4 hours and peak values of  $8.0 \times 10^{11}$  Watts in energy input.

Our model for the colatitudinal distribution of storm-energy inputs is also based on available information on Joule dissipation over the polar regions for typical storms (Ahn et. al., 1983; Kamide et. al., 1986; Knipp, 1989). Figure 2.6a is an example of this distribution (from Knipp, 1989), showing that most of this dissipation occurs in a narrow region of colatitudes centered on the auroral electrojet currents. We have incorporated this feature in our model by selecting the colatitudinal heating profiles to be Gaussian in shape, having widths of 10° in colatitude and centered at 21° and 159° colatitude, respectively (Figure 2.6b).

The altitude profile for the storm-energy input (Figure 2.7) is essentially that of  $\sigma_1/p$  (where  $\sigma_1$  is the Pedersen conductivity) which when multiplied by  $E^2$ , the square of the electric field assumed to be constant with height, gives the heating rate per unit mass. Because of the higher air density at lower altitudes, it is found that more than 80% of the thermal drive for the thermospheric storm-time circulation is provided by the lower maximum in this profile. Notice that, for reasons of simplicity the high-latitude heat inputs for the storm are assumed to be hemispherically symmetric.

FIGURE CAPTIONS FOR CHAPTER II

Fig. 2.1. The global mean temperature  $T_0$  ('K).

Fig. 2.2.  $Q_S$  ( $10^{-8}$  Watts/Kg) is the departure from the global mean heating rate of the solar heating at EUV and UV wavelengths and quiet-time high-latitude heating at solar maximum.

Fig. 2.3. Time histories of: a) Temperature changes ('K), b) Meridional winds (m/s), and c) Zonal winds (m/s) as the system is run to a steady-state. These time histories are shown at altitudes of 250 km (top panel), 150 km (middle panel), and 100 km (bottom panel) at  $40^\circ$  colatitude.

Fig. 2.4. Steady-state solstitial background temperature and wind fields:

a) Steady-state temperature (solid line) and its difference from the global mean temperature (dashed line) ('K), b) Background meridional winds with streamlines (m/s), c) Background zonal winds (m/s) with E for eastward and W for westward. For the meridional winds the barb notation is as follows: short barb (5 m/s); long barb (10 m/s); and flag (50 m/s). This notation is also followed in subsequent figures.

Fig. 2.5. a) The estimated hemispheric energy inputs (in units of  $10^{11}$  Watts) for the geomagnetic storms of 22 March 1979 (solid line)

and 13-14 March 1989. For the second storm lasting for 36 hours, the inputs for the first 12 hours (dashed line) and the second 12 hours (dotted line) are shown separately. b) Hemispheric energy input for the model storm (in units of  $10^{11}$  Watts).

Fig. 2.6. a) Example of the colatitudinal distribution of Joule heating from Knipp (1989), and b) Normalized colatitude heating profile for the model storm.

Fig. 2.7. Normalized altitude heating profile (per unit mass) for the model storm.

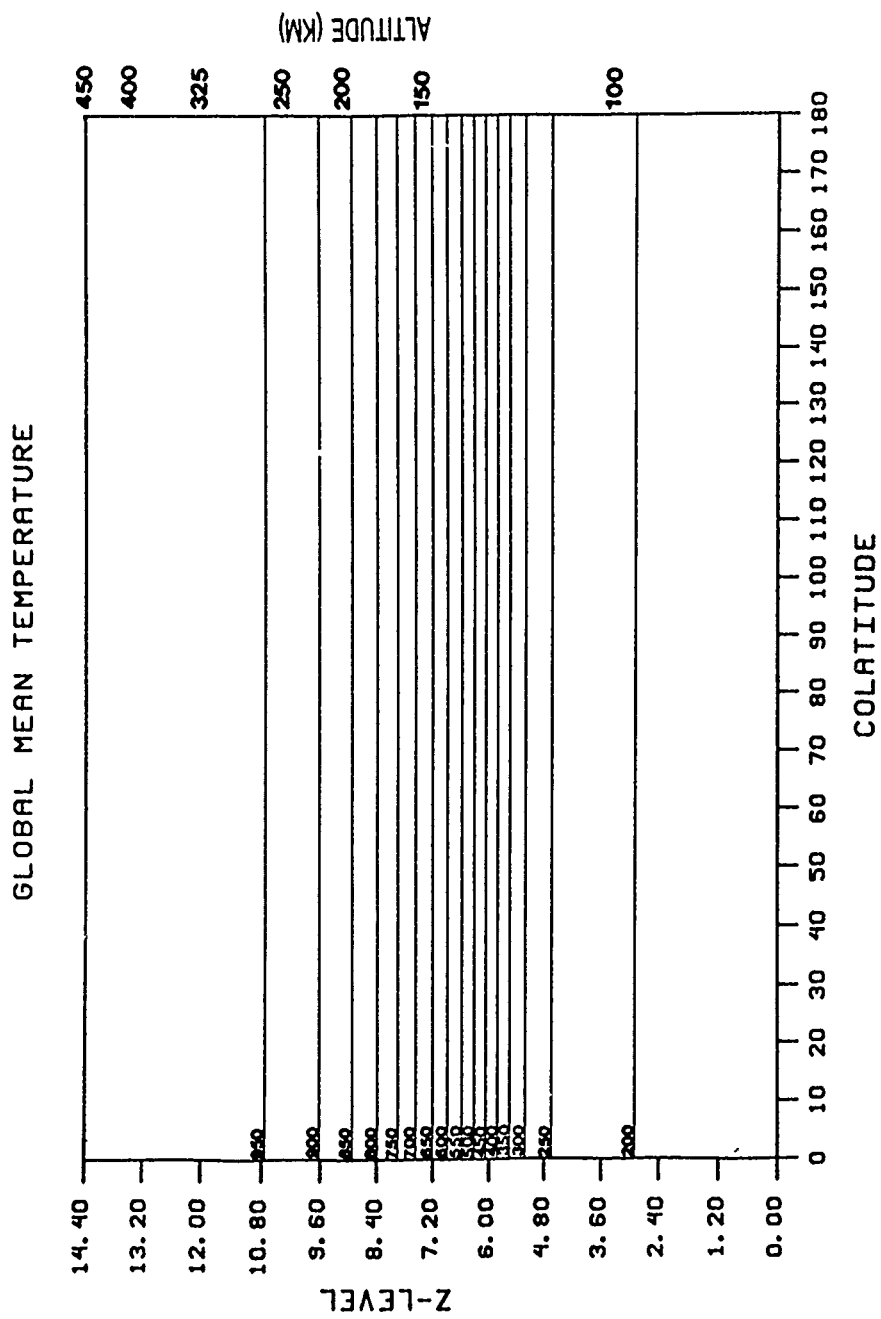


Figure 2.1

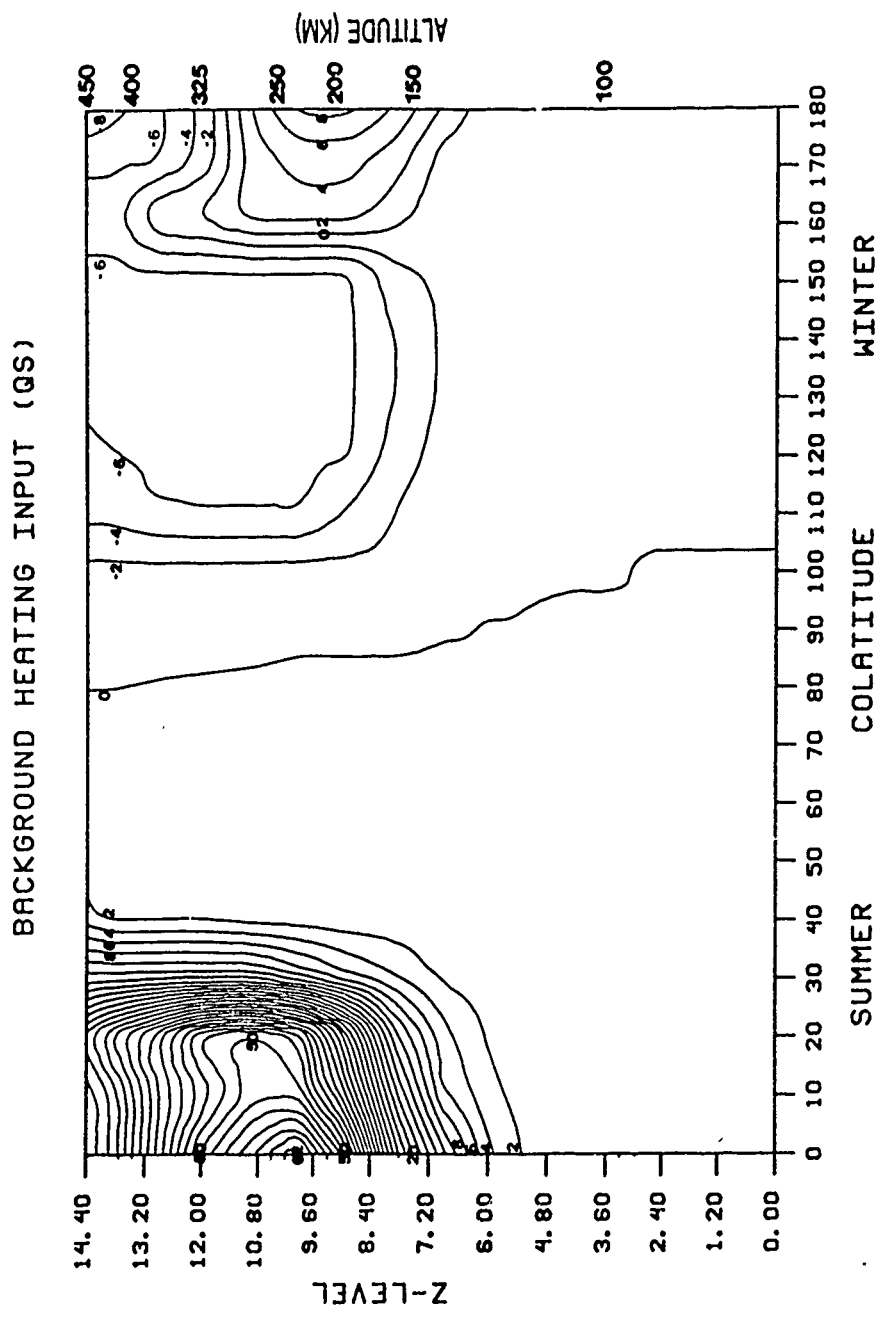


Figure 2.2

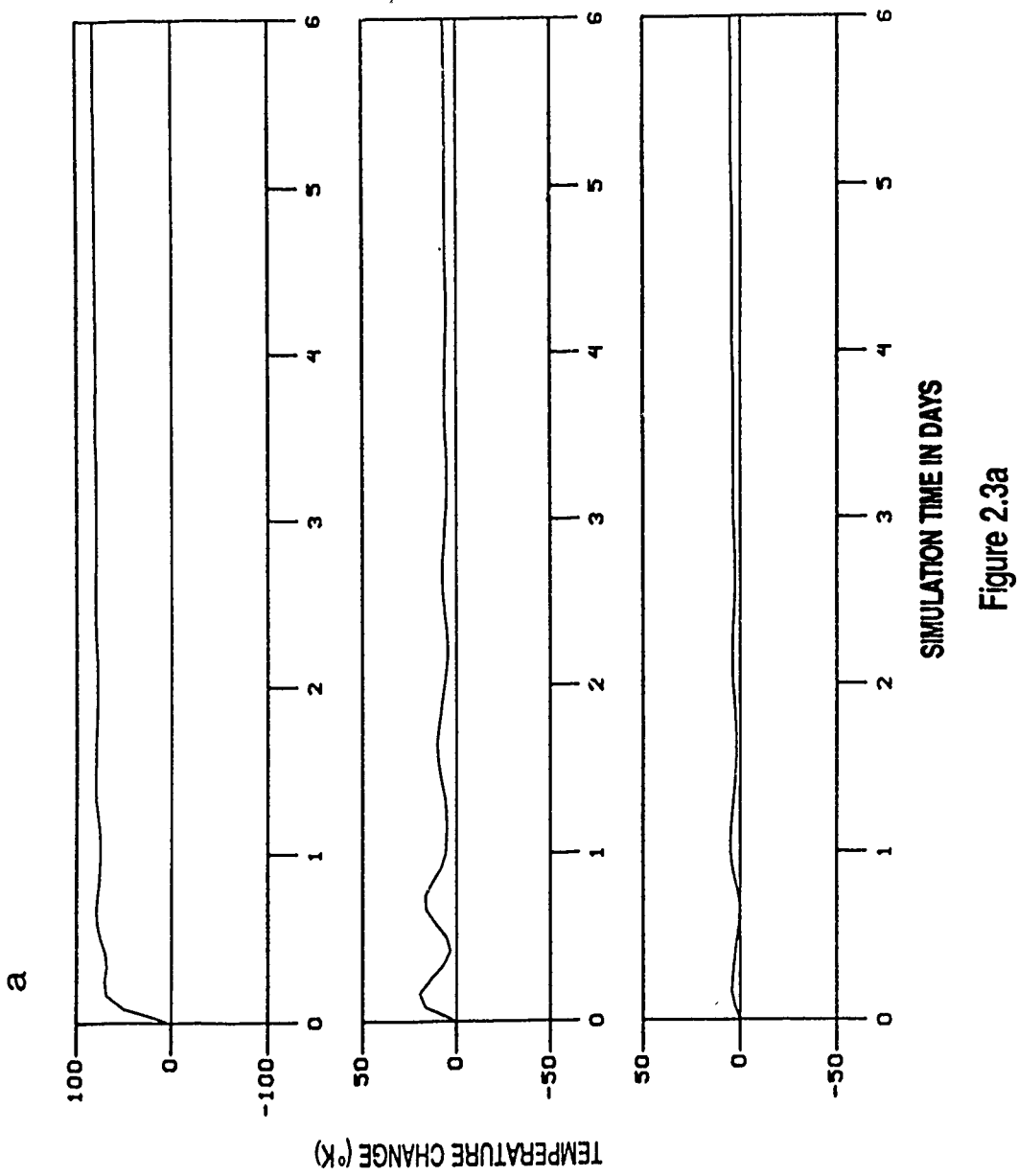


Figure 2.3a

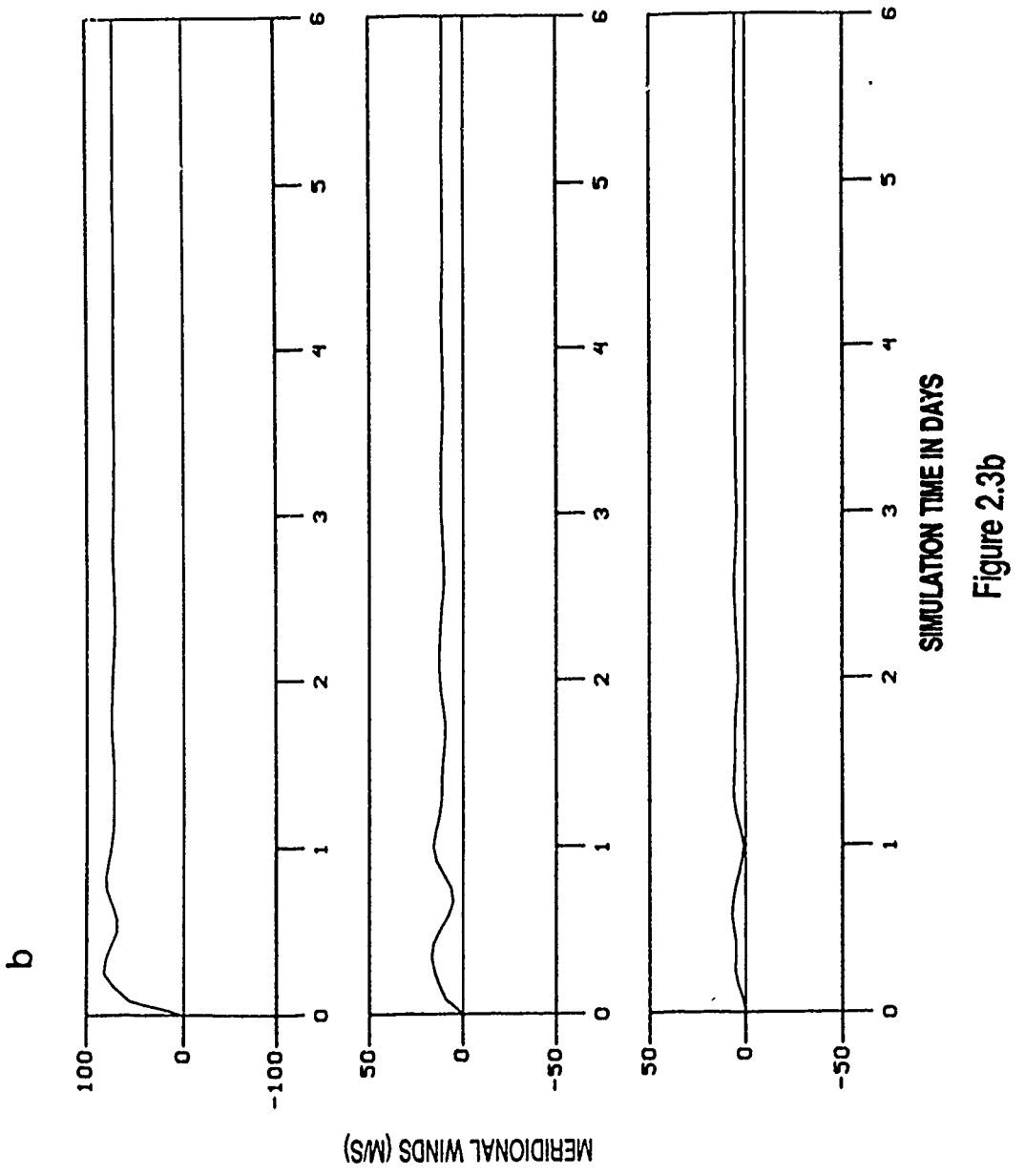


Figure 2.3b

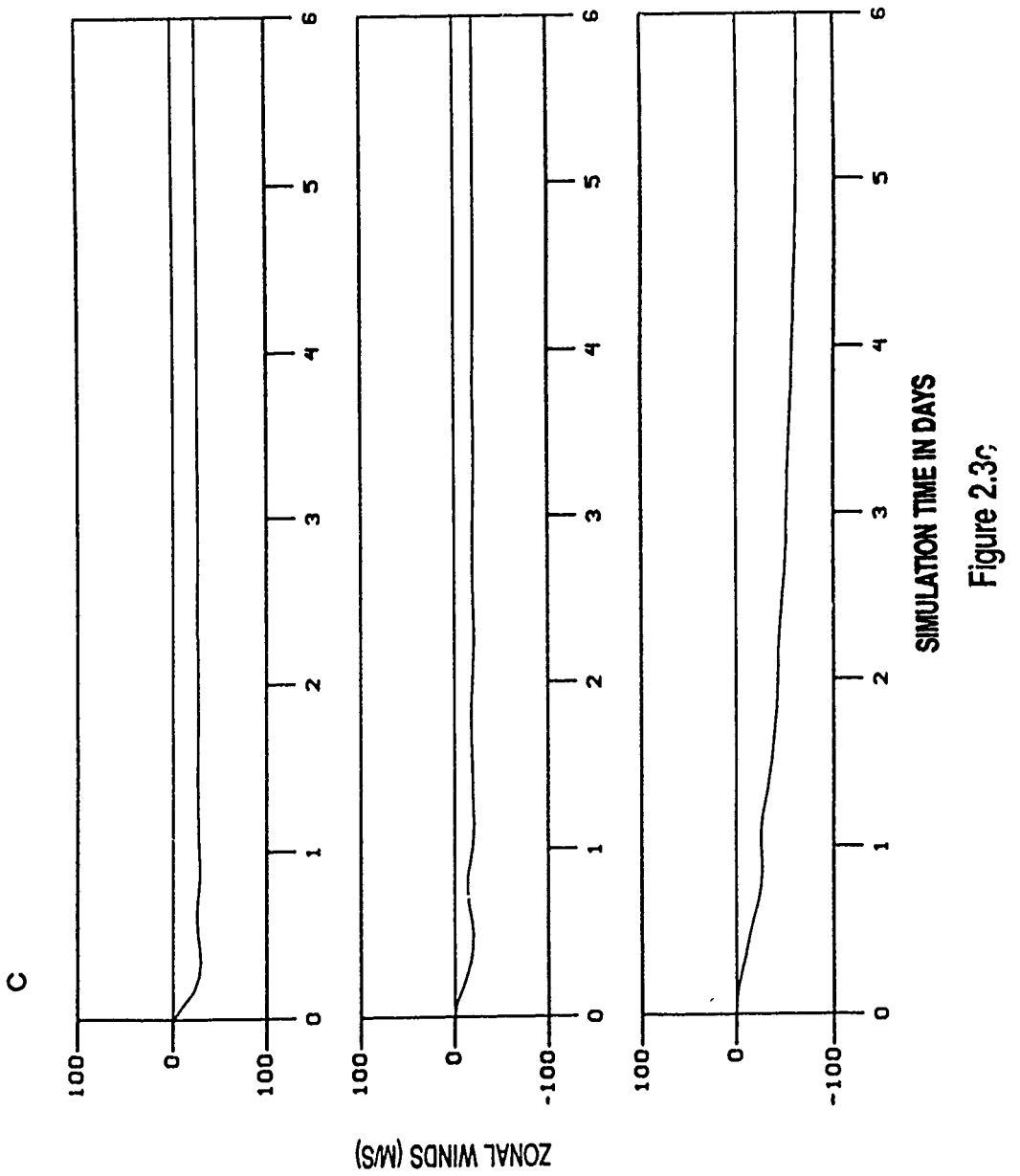


Figure 2.3c;

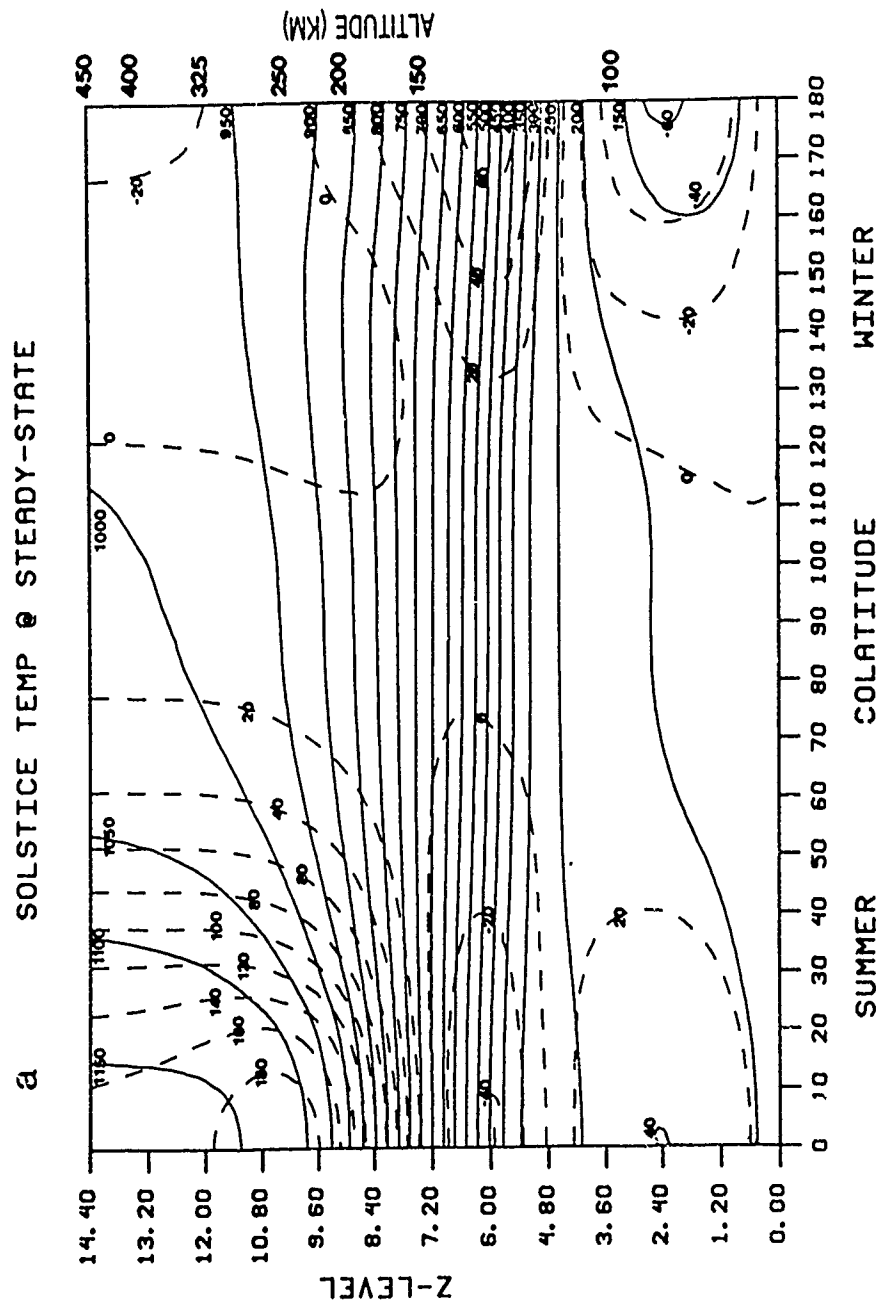
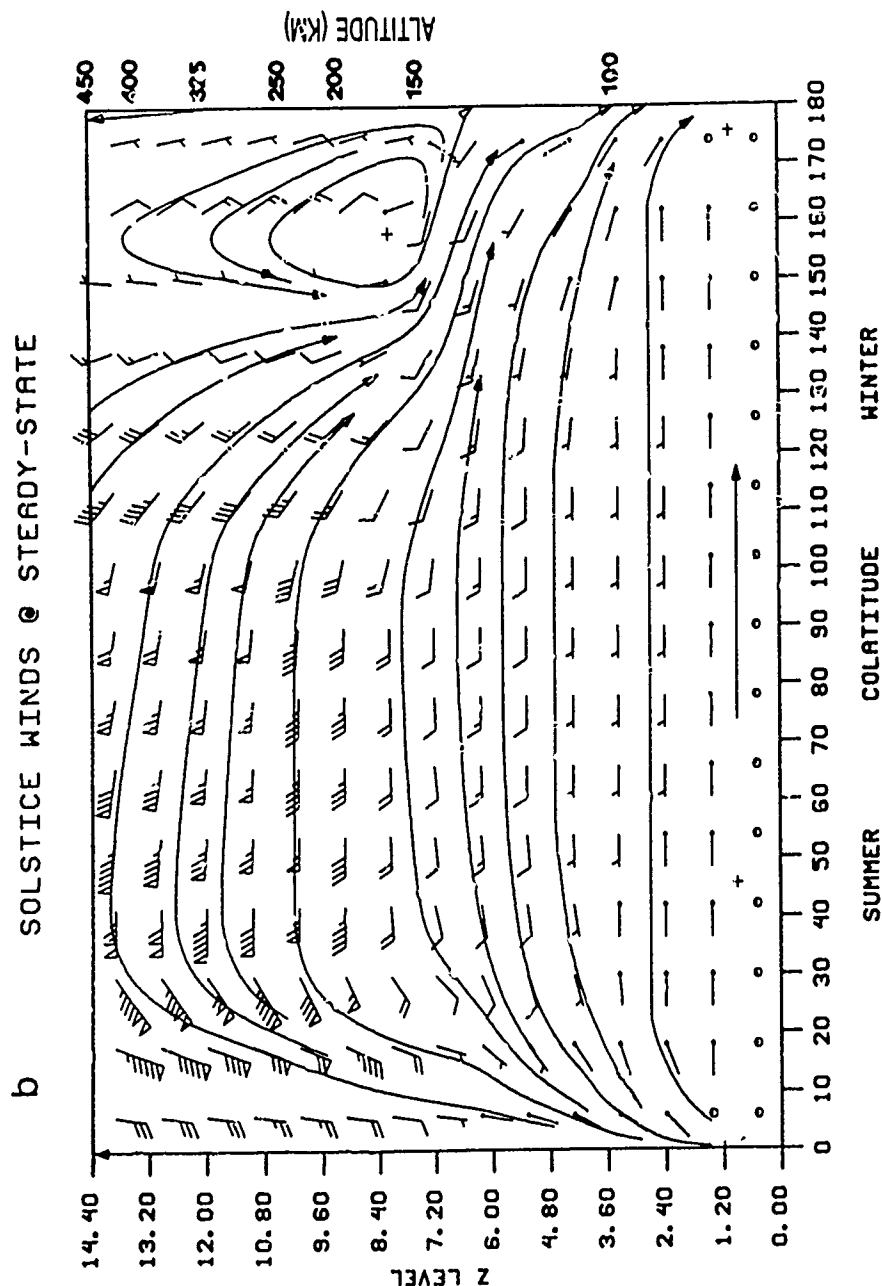


Figure 2.4a



**Figure 2.4b**

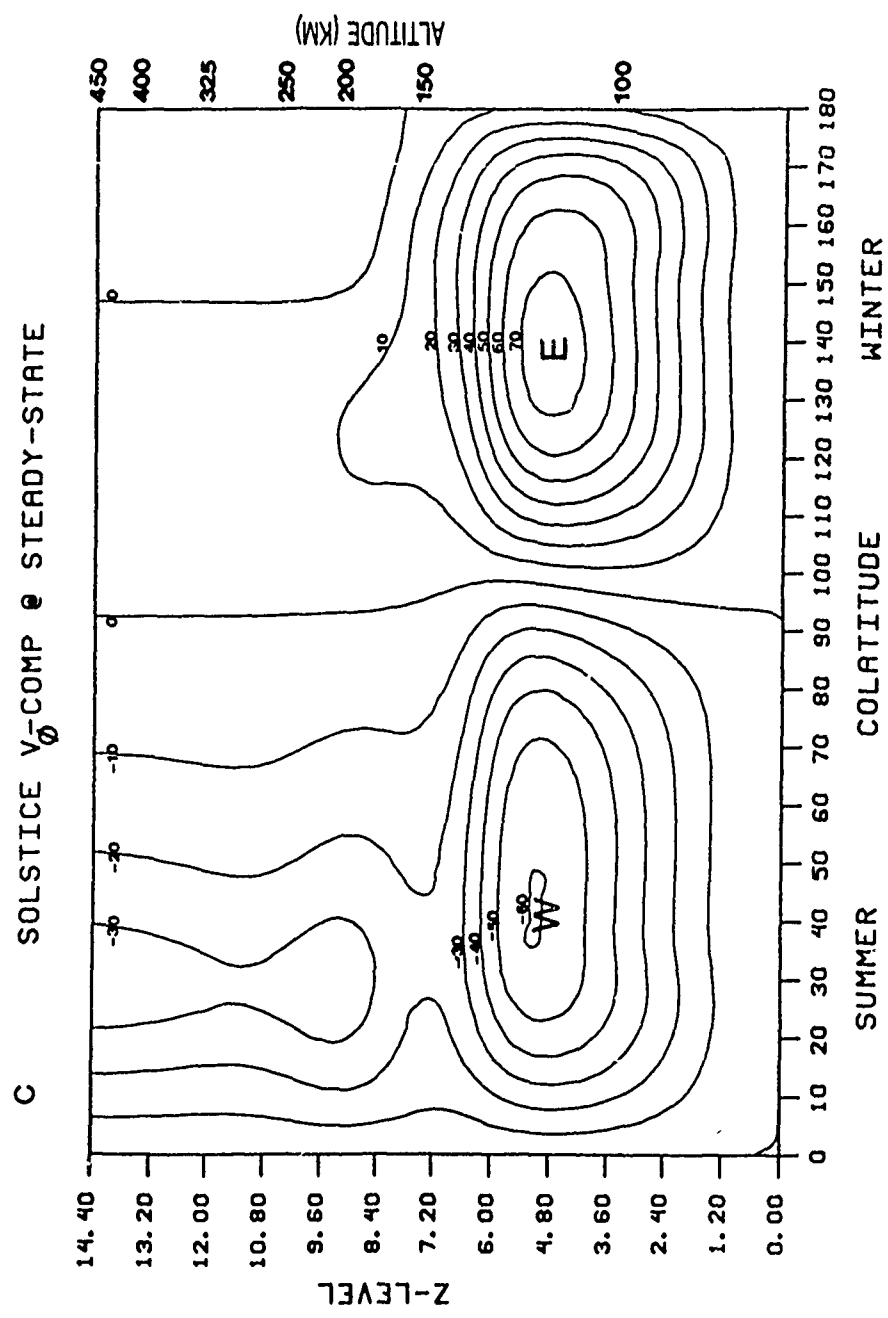


Figure 2.4c

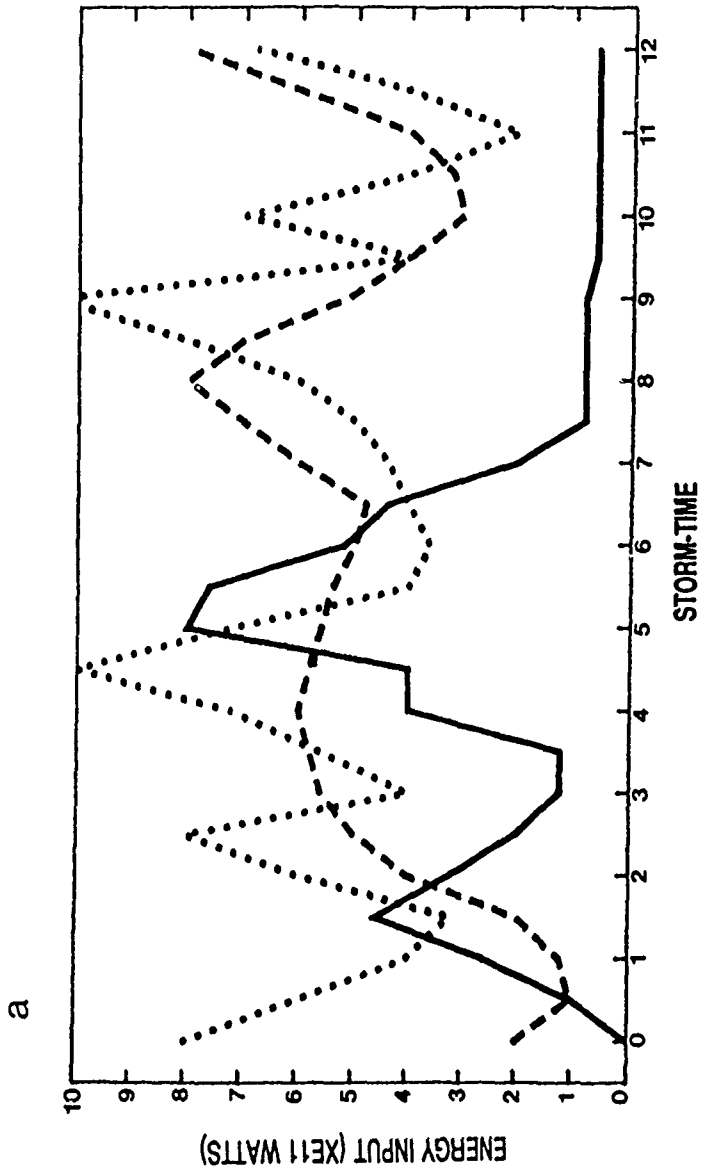
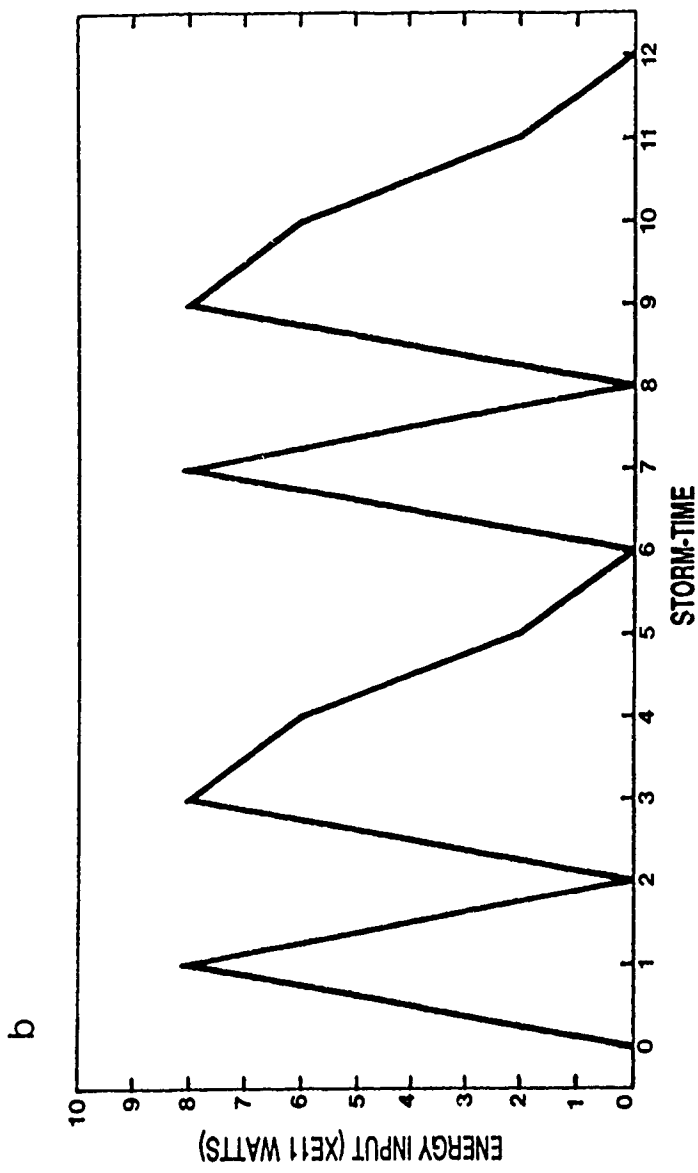


Figure 2.5a

Figure 2.5b



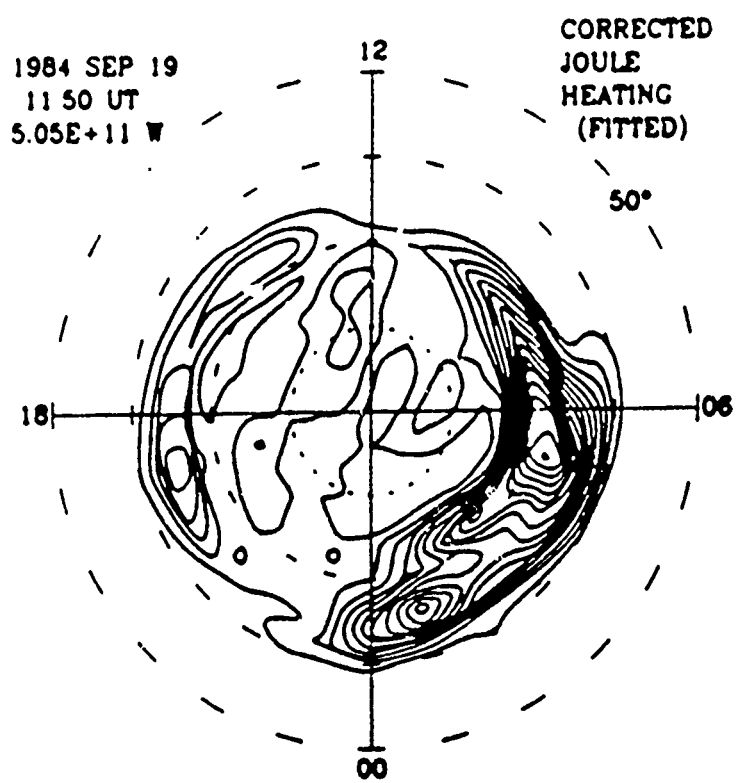


Figure 2.6a

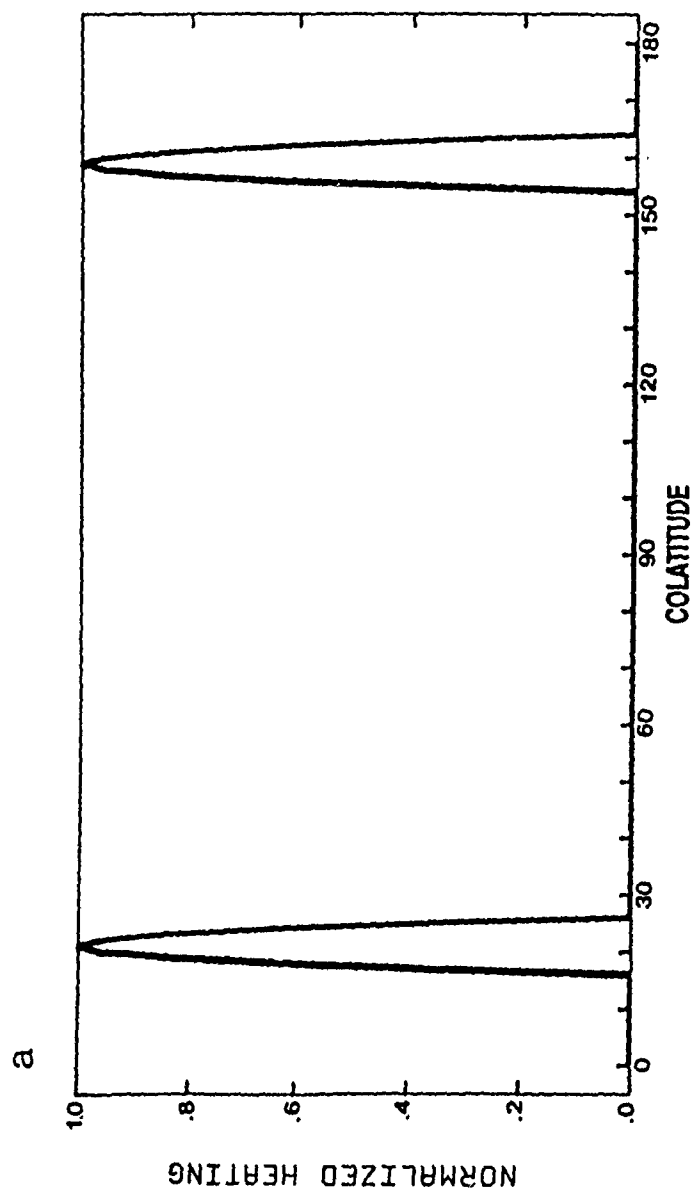


Figure 2.6b

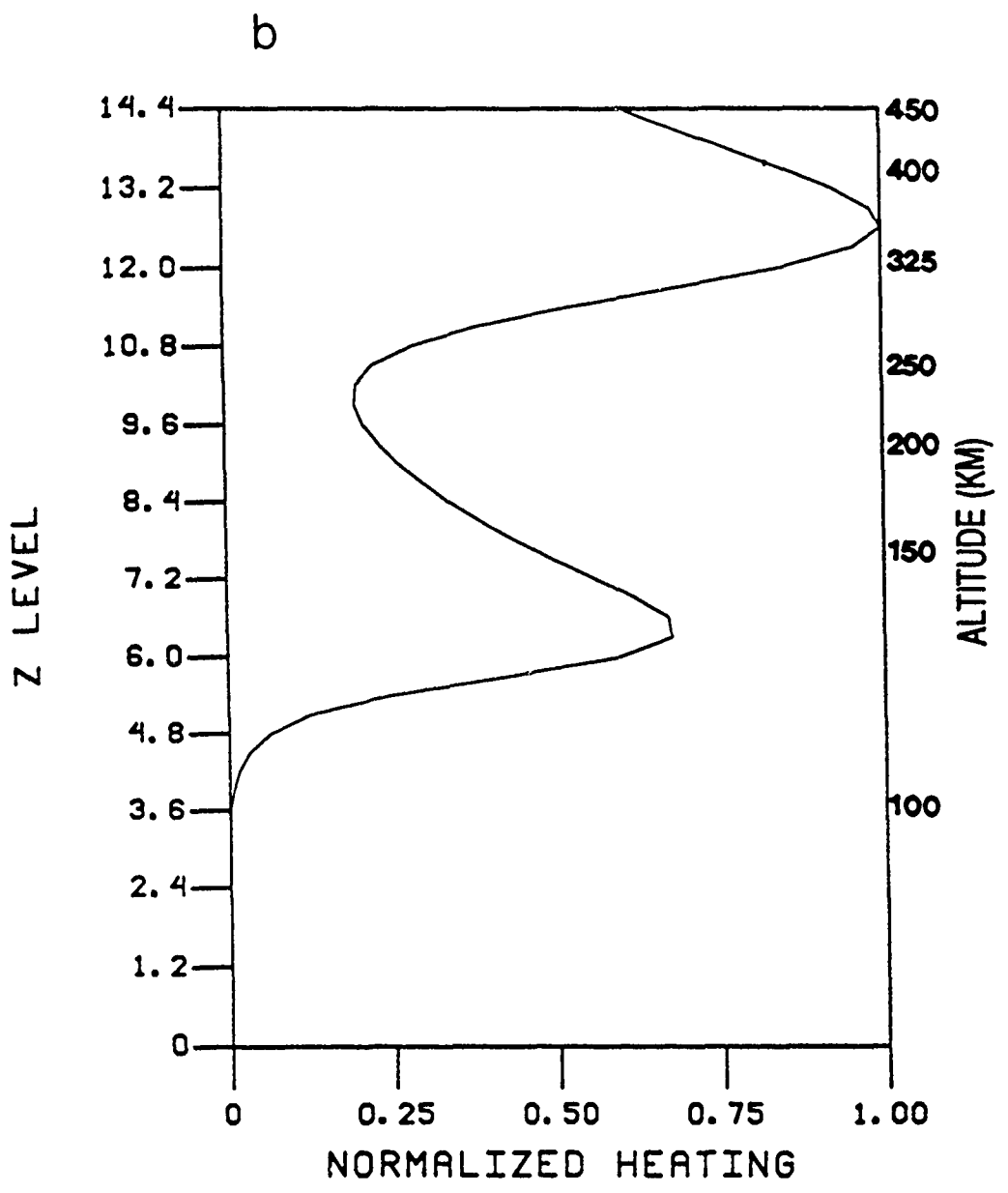


Figure 2.7

## CHAPTER III

### STORM SIMULATION RESULTS

#### 3.1 EVOLUTION OF STORM-TIME WINDS AND TEMPERATURES

The onset of a geomagnetic storm results in the sudden enhancement of auroral currents. The Joule dissipation of these currents leads to both impulsive heating which generates equatorward propagating gravity wave disturbances in both summer and winter hemispheres as well as longer-lasting heating that drives a global meridional circulation. The global circulation arises from the raising of the geopotential heights in the source regions resulting in a pole-to-equator pressure gradient in each hemisphere. In this chapter, we will describe these two features of the model response to a geomagnetic storm.

Figure 3.1 shows the storm-time winds at 2, 3, 7, and 11 hours after storm onset. At 2 hours (Figure 3.1a) the earliest wind disturbances have travelled, at high altitudes, a distance of approximately  $30^\circ$  in colatitude from the regions of high-latitude heating in either hemisphere. Above 250 km, in the region of high viscosity, the phases of the disturbances are uniform with height. Below 250 km, the phase tilt with height is clearly seen, the direction of the tilt being perpendicular to the direction of wave energy propagation which is upward and away from the source region (Hines, 1960; Holton, 1975). In the summer hemisphere, wind speeds associated with the disturbances exceed 150 m/s in places, which is approximately 50-100 m/s above the background wind speed (Figure 2.3b). In the winter hemisphere, the distur-

bance wind speeds are weaker.

At 3 hours (Figure 3.1b), the disturbances from both hemispheres have reached the equator. At 7 hours (Figure 3.1c) the disturbances from the summer hemisphere have penetrated well into the winter hemisphere. Large-scale meridional circulation patterns are also evident, with the summer hemisphere cell extending to 140° colatitude. This cell is greatly perturbed by the disturbances above 150 km. The winter hemisphere cell is reversed in direction, extending to 110° colatitude at 120 km and to 140° colatitude at higher altitudes.

At 11 hours (Figure 3.1d), the disturbances still persist above 200 km, but below this altitude the meridional circulations have become better defined. The summer hemisphere cell meets the winter hemisphere cell at approximately 110° colatitude. The circulation patterns continue to change in response to the rapidly varying heat sources assumed in the model.

Figure 3.2 features the storm-time temperature field at times corresponding to the wind fields in Figure 3.1. At 2 hours, above 200 km, temperatures have generally increased at high-latitudes, in direct response to storm-time heating (Figure 3.2a). More importantly, the figure shows temperature perturbations of 50°K at 40-50° colatitude and 120-140° colatitude, respectively. Comparing Figures 3.1a and 3.2a, it can be seen that the temperature perturbations are approximately 90° out of phase with the vertical velocities. In the equatorial region between 60° and 140° colatitudes, the temperature field is undisturbed at this time.

At 3 hours, however, the temperature oscillations have reached the equator (Figure 3.2b), and mirror the vertical velocity oscillations (Figure 3.1b) with the aforementioned phase shift. At the same time, at high latitudes, evidence for adiabatic cooling resulting from strong upward motion above the heat source can be seen in the decrease of temperature above 200 km.

At 7 hours (Figure 3.2c) the temperature perturbations have crossed over the equator as was the case for the wind perturbations. Below 250 km, there is an increase in temperature on the order of 100°K at mid and low latitudes. This increase is apparently associated with the establishment of the meridional circulation (Figure 3.1c).

At 11 hours (Figure 3.2d) we see similar features in the temperature field as at 7 hours below 250 km. Above this height, additional regions of warming of 50-100°K due to the persistence of wind disturbances are also observed.

### 3.2 INFLUENCE OF BACKGROUND SEASONAL WINDS AND TEMPERATURES ON MEAN STORM-TIME WINDS AND TEMPERATURES

Figure 3.3 shows the 12-hour-averaged storm-time wind fields for model runs with and without background seasonal winds and associated temperatures (Figures 3.3a and b). The averaged wind fields are obtained from the instantaneous wind fields at 10 minute intervals over the 12 hour span of our model storm.

With background winds, the storm-time meridional circulation shows a two-celled structure with a larger summer hemisphere cell extending

to 110-130° colatitude. Both cells show increases in wind speed over the background solstice winds (Figure 2.3b). This is best shown by the reversed winter hemisphere cell which exhibits winds averaging 50 m/s compared to 10-15 m/s for the background winds alone. The latitudinal extent of this cell is also greater, extending to 110° colatitude at 150 km. In addition, the vertical extent of this cell has increased and the center of the cell has shifted downward from 175 km to 120 km.

In comparison, the storm circulation without background winds shows a two-celled structure, with the two cells being symmetric about the equator. This symmetry merely mirrors the corresponding symmetry in the heat sources (Figure 2.6b).

The zonal winds generated by the storm consist of strong westward jets equatorward of the heat sources and much weaker eastward flows poleward (Figure 3.3d). This storm-time zonal wind system enhances the background winds, as can be seen by comparison of Figures 3.3c and 2.3c. This enhancement leads to the intensification and poleward migration of the westward jet normally present in the summer hemisphere during the solstitial season. In the winter hemisphere, we have a regime with a storm-time westward jet located overhead of the seasonal eastward jet with strong shears in the intermediate zone.

Lacking direct observational support, it is not clear to what extent the double-jet structure of the zonal wind system and the intermediate region of strong shears calculated for the winter hemisphere are, in fact, realistic. It should also be recalled that there are additional storm-time winds generated by ion drag effects near the

auroral electrojet region which are not included in our model (Hernandez and Roble, 1976; Killeen et. al. 1984, Killeen et. al., 1986).

Figure 3.4 shows corresponding results for the 12-hour-averaged storm-time temperature fields with background winds (Figure 3.4a) and without background winds (Figure 3.4b). Careful inspection shows that for both these cases, there is an average increase of 50° K in the storm-time temperatures at middle and low latitudes. This temperature increase is due to downward velocities of the storm-generated part of the meridional circulation, whose strength is nearly the same with or without background winds.

### 3.3 CHARACTERISTICS OF STORM-GENERATED WAVE DISTURBANCES

We next turn our attention to the disturbances generated by the storm. Figures 3.5a and 3.5b exhibit the storm-generated disturbances at two colatitudes at an altitude of 325 km. The top panel of Figure 3.5a shows the heat input profile (in units of  $10^{11}$  Watts), the middle panel shows the vertical velocity component of the wind response at 40° colatitude, and the bottom panel shows the vertical velocity response at 70° colatitude. In Figure 3.5b, the meridional component of the wind response is shown instead of the vertical velocity component.

The oscillating heat source generates wave disturbances throughout the 12-hour period of storm simulation. We define a disturbance, somewhat arbitrarily, as a full cycle of the oscillation in vertical velo-

city. Six disturbances are identified in this manner and are numbered in Figures 3.5a and b. The beginning and ending times of each disturbance are also indicated by vertical markers. At 40° colatitude these times are 0:30-2:00 storm-time (ST) for the first disturbance, 2:00-4:00 ST for the second, 4:00-6:00 ST for the third, 6:00-7:50 ST for the fourth, 7:50-10:00 ST for the fifth, and finally 10:00-12:00 ST for the sixth disturbance.

The first disturbance, which arrives at 40° colatitude as early as 0:30 ST, must have originated from the first heat pulse in the form of a spectrum of gravity waves with speeds up to 900 m/s. The initial part of the second disturbance before 2:30 ST must also have originated from the comparatively slower gravity waves generated by the first heat pulse. At 2:30 ST the fastest wave from the second heat pulse should have arrived at this colatitude, if its velocity was the same (~900 m/s) as of the first wave from the initial pulse. Hence, waves from both the first and second heat pulses would contribute to the subsequent portions of the second disturbance. The most probable interpretation for the third disturbance between 4:00 and 6:00 ST is that it results from the slower waves from both the first and second heat pulses. Similar to the first two disturbances, the fourth and fifth disturbances consist of waves mostly from the third and fourth heat pulses, respectively, and to a lesser extent, from the earlier pulses. The interpretation of the sixth disturbance is similar in nature to that for the third disturbance.

In the bottom panel of Figure 3.5a for 70° colatitude, much of the

finer structure in the disturbances has disappeared. Comparison of the middle and bottom panels in this figure show that the disturbances travel from 40° to 70° colatitude with a time delay of 70-120 minutes.

The meridional velocity disturbances in Figure 3.5b, whose durations are assumed to be the same as the corresponding vertical velocity disturbances in Figure 3.5a, have certain peculiar features. For instance, the latter part of the second disturbance after 5:00 ST and all of the third disturbance at 70° colatitude are considerably depressed in magnitude from their magnitudes at 40° colatitude. In addition, the fourth disturbance (6:00-7:50 ST) and the earlier part of the fifth disturbance (8:00-8:50 ST) passing 40° colatitude are depressed in magnitude compared to their magnitudes at 70° colatitude. These features are most likely explained as due to a disturbance launched in the southern hemisphere, which is propagating in the opposite direction to the other disturbances. As this southern hemispheric disturbance propagates from 70° to 40° colatitude with a speed of 900 m/s, it is successively superposed on the equatorward propagating disturbances causing the "depression" in magnitude of the second and third disturbances at 70° colatitude and later the fourth and fifth disturbances at 40° colatitude.

Figure 3.5a also gives information concerning the phase speeds, dispersion and dissipation characteristics of the disturbances. The phase speed of the leading edge of the first disturbance is approximately 790 m/s as it propagates from 40° to 70° colatitude. Other wave disturbances in Figure 3.5a exhibit slower phase speeds averaging

450-550 m/s, which is in line with the observations of Hernandez and Roble (1978) for storm-generated disturbances at middle latitudes. We also see evidence of dispersion by the increase of the periods of the disturbances as they travel from 40° to 70° colatitude. For example, the first disturbance at 40° colatitude has a period of 90 minutes. When this disturbance reaches 70° colatitude, its period has increased to 120 minutes. Similarly, the second disturbance has a period of 120 minutes at 40° colatitude and a period of 145 minutes at 70° colatitude. Furthermore, Figure 3.5a also shows that fast-moving, long-period waves tend to maintain their identities over longer distances, as compared to slower-moving high-frequency waves because they are less affected by dissipation (Hines, 1960; Richmond, 1978a). This can be seen most clearly in the longer period of the disturbances in regions further away from the source region.

#### 3.4 INFLUENCE OF BACKGROUND WINDS AND TEMPERATURES

The influence of the background meridional winds and temperatures on the wave disturbances is illustrated in Figure 3.6, where we observe velocity disturbances that started in the summer and winter hemispheric source regions and reached 40° (solid line) and 140° (dashed line) colatitudes, respectively, having travelled the same meridional distance.

In the summer hemisphere, the disturbances are propagating in the direction of the background meridional wind (Figure 3.7). In the winter hemisphere, the disturbance propagation is opposite to the direction of meridional winds. In addition, the disturbances in the

summer hemisphere are propagating in a region of warmer temperatures than the disturbances in the winter hemisphere. As a result, the disturbances in the summer hemisphere are observed to arrive at 40° colatitude, earlier than the arrival of the disturbances in the winter hemisphere at 140° colatitude. This time difference, however, amounts to no more than about 12 minutes in a travel time of nearly an hour, even at the highest altitude (325 km) shown in Figure 3.6.

In order to understand the observed time difference, mentioned above, one may start with the simplified expression for the intrinsic frequency for a gravity wave in a hydrostatic and isothermal atmosphere. For our log p coordinate system (Chapter 2) with  $Z=\ln(p_s/p)$ , this frequency is given by:

$$\omega^2 = N^2 H^2 \left( \frac{\ell^2}{m^2 + \frac{1}{4}} \right) \quad (3.1)$$

where  $N$  is the buoyancy frequency,  $H$  is the scale-height, and  $\ell$  and  $m$  are the meridional and vertical wave numbers, respectively. The above expression for the intrinsic frequency is the same as that found in Andrews et. al. (1987) provided we note that in the log p coordinate system used by these authors  $Z=H \ln(p_s/p)$ .

Using the isothermal value  $N^2 = \kappa g/H = \kappa R T / H^2$ , where  $\kappa=R/C_p$ , we obtain the intrinsic phase velocity in the meridional direction as:

$$v_{ph} = \left( \frac{\omega}{\ell} \right) = \left( \frac{-\kappa R}{m^2 + \frac{1}{4}} \right)^{1/2} T^{1/2} \quad (3.2)$$

which shows that the intrinsic phase velocity varies directly as the square root of the temperature.

We observe from Figure 2.4a that the average temperature at 325 km between the source region and 40° colatitude in the summer hemisphere is 1080° K. Similarly, the average temperature between the source region and 140° colatitude in the winter hemisphere is 960° K. Using these temperatures values in the above expression for the phase velocity, we find that the ratio of the phase velocities of the waves travelling equal distances in the two hemispheres is in the ratio  $(1080/960)^{1/2} = 1.06$ , accounting for a 3.6 minute difference in travel times in a period of one hour due to the temperature difference between the hemispheres.

In addition, the intrinsic phase velocities of the waves (~500 m/s) are Doppler-shifted by the background winds. This Doppler-shift is positive in the summer hemisphere (where the background meridional winds, as pointed out earlier, are in the same direction as the direction of wave propagation (equatorward), and have an average speed of 100 m/s along the wave path at 325 km. In the winter hemisphere, the wind direction changes along the wave path, averaging out to almost zero. Because of the Doppler-shift effect, the resultant phase velocities of the waves in the summer and winter hemispheres are, therefore, in the ratio  $600/500 = 1.2$ , accounting for a 12 minute difference in a travel time of one hour.

Our simple calculation, therefore, gives a total sixteen minute time difference in the travel times of the disturbances at 325 km as

against the twelve minute difference more accurately calculated in our model. At lower altitudes, where most of the wave energy resides, both the wind and temperature effects on phase velocities and travel times become negligible.

Figure 3.6 also shows that the amplitudes of the disturbances in the summer hemisphere travelling in the direction of the background meridional wind are less than for disturbances in the winter hemisphere travelling against the background flow. This is to be expected based on the approximate tendency for the waves in the disturbances to conserve wave action density  $A = E / (\omega - \ell \bar{v})$ , where  $E$  is the wave energy density,  $\omega$  is the intrinsic frequency,  $\ell$  is the wave number,  $\bar{v}$  in the wind in the direction of wave propagation, and  $\ell - k\bar{v}$  is the Doppler-shifted frequency (Andrews et. al., 1987; Bretherton and Garrett, 1968). As  $\omega - \ell \bar{v}$  decreases, as in the example of summer hemispheric disturbances, the wave energy (and hence amplitude) must decrease, as is observed. The net effect is small because the phase speeds of the disturbances are much larger than the background wind velocity.

### 3.5 VERTICAL STRUCTURE OF THE WAVE DISTURBANCES

As illustrative of the vertical structure of the disturbances, Figure 3.8a shows the first two vertical velocity disturbances (solid line) and the corresponding temperature disturbances (dashed line) at 70° colatitude for altitudes between 100 and 450 km. For the velocity disturbances, the distance between two consecutive altitude markers also represents a vertical velocity of 5 m/s. The maximum amplitude

of the velocity disturbances is  $\pm 7.5$ m/s. For the temperature disturbances the same distance between the altitude markers corresponds to  $50^{\circ}$ K. The maximum amplitude of the temperature disturbances is  $50^{\circ}$ K. The amplitudes of the velocity disturbances do not increase as rapidly as the inverse-root of air density because of the increasing importance of viscous dissipation with height. Increasing dissipation is also responsible for the decrease of phase tilt with height (Hines, 1968), the phase becoming uniform above 250 km (see also Figure 3.1). We further notice that the phase difference between the vertical velocity disturbances and the temperature disturbances is close to  $90^{\circ}$ , as would be the case if adiabatic heating (cooling) due to the vertical motions of the velocity disturbances is the cause of the temperature disturbances.

Figure 3.8b shows the same disturbances in meridional velocity (solid line) with the distance between the altitude markers equal to 50 m/s (positive equatorward). The meridional velocity disturbances show a similar increase of amplitude with height and a similar phase tilt as the vertical velocity disturbances. The meridional velocity disturbances are different, however, in that they are nearly in phase with the temperature disturbances. This means that the vertical and meridional velocities are out of phase by  $90^{\circ}$ , which follows from the well-known polarization relations (Gossard and Hooke, 1977; Hines, 1960).

### 3.6 WAVE-INDUCED HEAT AND MOMENTUM FLUXES

Both the vertical and meridional velocity disturbances can, over the period of the disturbances, produce net fluxes of heat and meridional momentum in the vertical and meridional directions, respectively. For example, a net heat flux is produced if the vertical (meridional) velocity disturbances and the temperature disturbances are not in exact quadrature (i.e. phase difference is not 90°) or if the disturbances are not exactly symmetric (i.e., the average velocity or the net temperature change over the period of the disturbance is not zero) either due to dissipation or non-stationarity (i.e., change in wave amplitude over a wave period).

Figures 3.9a,b, and c show the vertical and meridional heat fluxes, and the vertical flux of meridional momentum generated at 250 km by the disturbances shown in Figures 3.8a and 3.8b. Figure 3.9a shows the vertical velocity disturbances (top), the temperature disturbances (middle), and the vertical heat fluxes (bottom). The starting and ending times of the disturbances to be referred to below, are with respect to the vertical velocity disturbance as observed at the specific altitude of 250 km. The first vertical velocity wave (1:40-4:00 ST) is nearly in quadrature with its corresponding temperature wave. In addition, it is only slightly asymmetric in shape. Hence, its net vertical heat flux appears to be close to zero. The second vertical velocity wave (4:00-6:15 ST) is also nearly in quadrature with its corresponding temperature wave. However, this wave is more asymmetric in shape (i.e. the downward velocities are larger than the upward velocities) and yields a net downward flux of heat.

Correspondingly, Figure 3.9b shows the meridional velocity disturbances (top), the temperature disturbances (middle), and the meridional heat fluxes (bottom). As previously mentioned (Chapter 3.3, Figure 3.5b) during the period (4:00-6:15 ST) of the second disturbance, there is indication of superposition effects from a poleward travelling disturbance as well. What we notice is that, the meridional velocity disturbances are asymmetric in shape although in phase with the corresponding temperature disturbances, resulting in a net equatorward heat flux.

Similarly, Figure 3.9c shows the vertical velocity (top), the meridional velocity (middle) disturbances, and the vertical flux of meridional momentum (bottom). The first vertical velocity disturbance and the corresponding meridional velocity disturbance (1:40-4:00 ST) are neither in quadrature with each other nor are symmetric in shape. This results in a net upward meridional momentum flux.

Between 4:00 and 6:15 ST, when the second disturbance is also influenced by a poleward travelling disturbance toward the end of its period, it is the downward velocity peak that is closer in time to the positive peak in the meridional velocity and, as a result, the net vertical flux of meridional momentum is downward.

FIGURE CAPTIONS FOR CHAPTER III

Fig. 3.1. Time evolution of storm-time winds. The winds (m/s) are shown at: a) 2 hours, b) 3 hours, c) 7 hours, and d) 11 hours after storm onset.

Fig. 3.2. Same as Figure 3.1 except for storm-time temperatures ('K).

Fig. 3.3. Time-averaged storm-time meridional winds: a) With background winds and b) Without background winds. Time-averaged storm-time zonal winds: c) With background winds and d) Without background winds. (See text for definitions of with and without background winds.)

Fig. 3.4. Same as Figure 3.3 except for storm-time temperatures: a) With background winds and b) Without background winds.

Fig. 3.5. Storm-generated wave disturbances: a) Disturbances in vertical velocity at 325 km are shown at 40° colatitude in the middle panel and at 70° colatitude in the bottom panel. The top panel is the storm-time hemispheric heat input (in units of  $10^{11}$  Watts) profile shown for the purpose of relating the waves to their sources. b) Same as a) except for disturbances in meridional velocity.

Fig. 3.6. Influence of background seasonal winds and associated tem-

peratures on vertical velocity disturbances propagating from the summer and winter hemispheric source regions (see text). The disturbances at 40° colatitude (solid line) and at 140° colatitude (dashed line) are shown at 325 km (top panel), 250 km (middle panel), and 150 km (bottom panel).

Fig. 3.7. Background meridional winds for the solstitial season. The corresponding zonal winds are shown in Figure 2.4c.

Fig. 3.8. Vertical structure of the first two waves at 70° colatitude (see text): a) Vertical velocity (solid line) and temperature change (dashed line). b) Meridional velocity (solid line) and temperature change (dashed line).

Fig. 3.9. Transport of heat and momentum by the first two wave disturbances at 250 km. The parameters shown in this figure are: a) Vertical velocity (top panel), Temperature change (middle panel), and Vertical heat flux (bottom panel). b) Meridional velocity (top panel), Temperature change (middle panel), and Meridional heat flux (bottom panel). c) Vertical velocity (top panel), Meridional velocity (middle panel), and Vertical flux of meridional momentum (bottom panel).

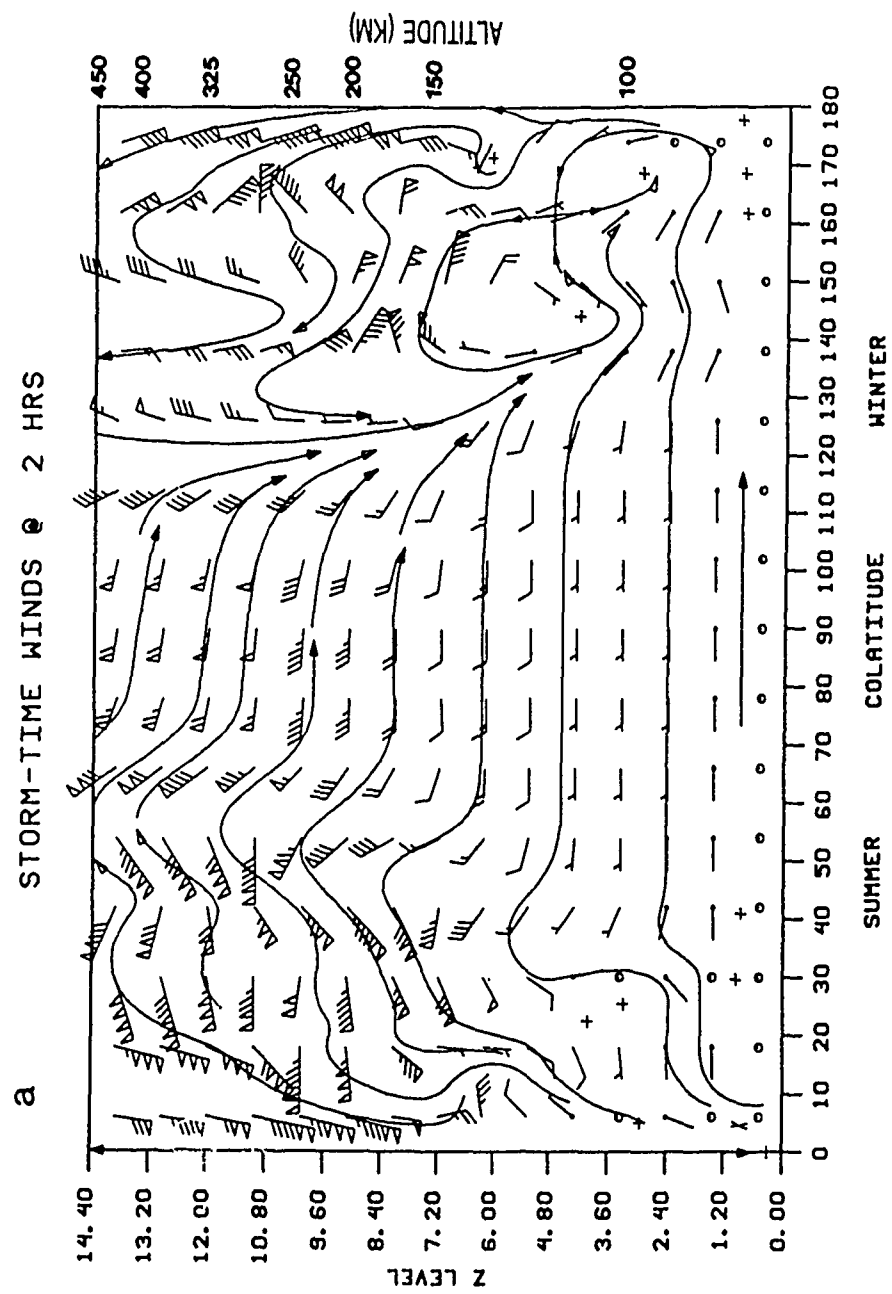
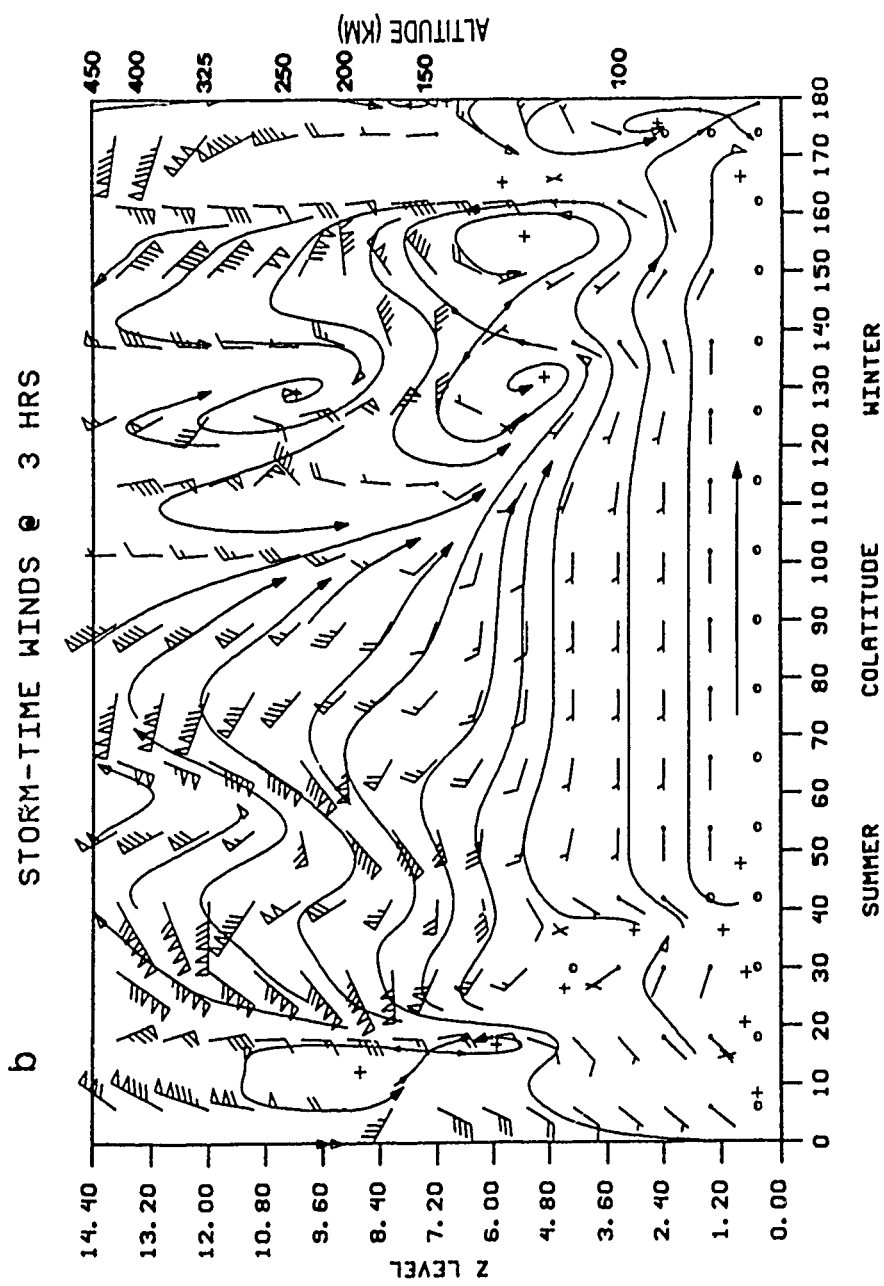


Figure 3.1a



**Figure 3.1b**

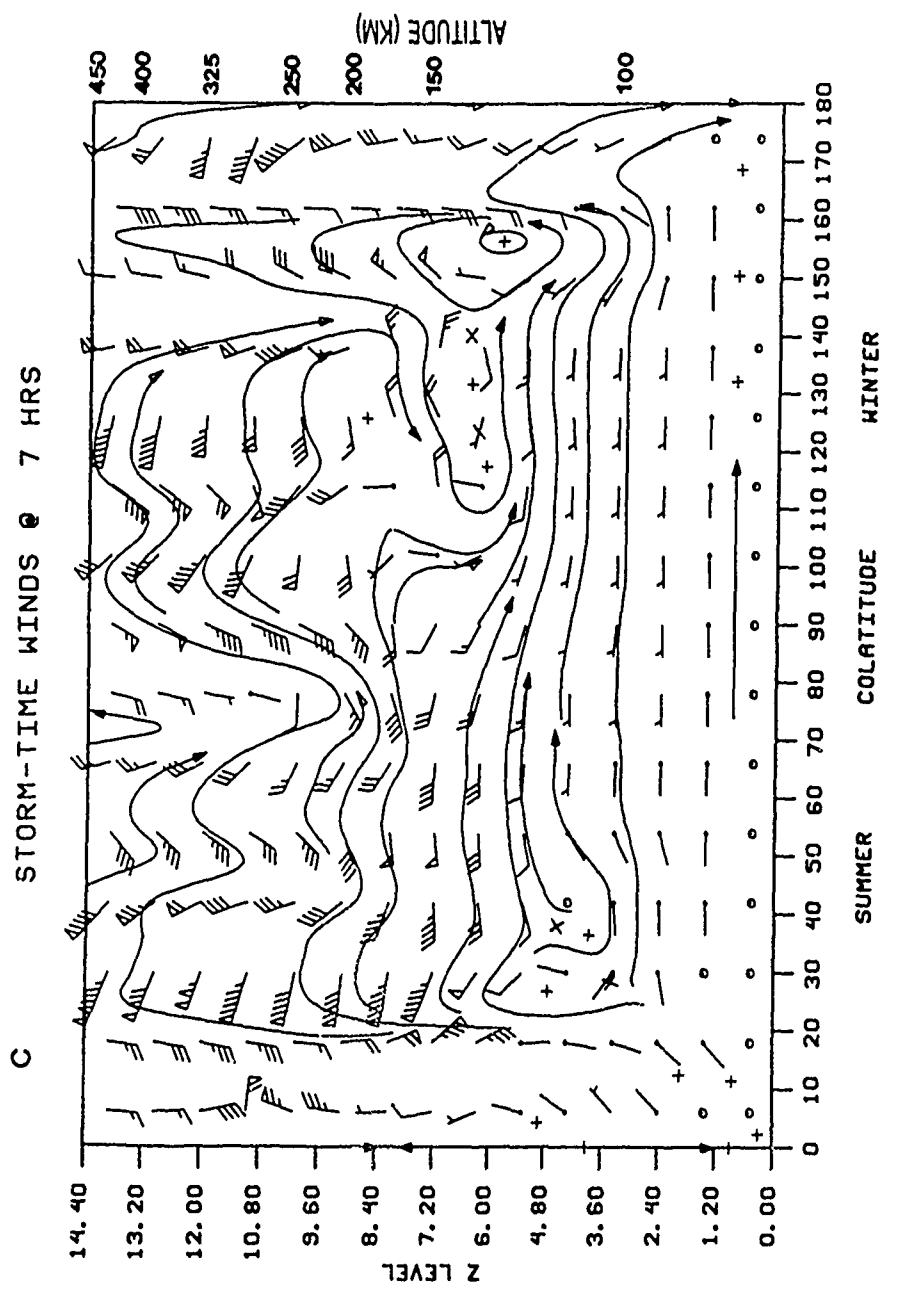


Figure 3.1c

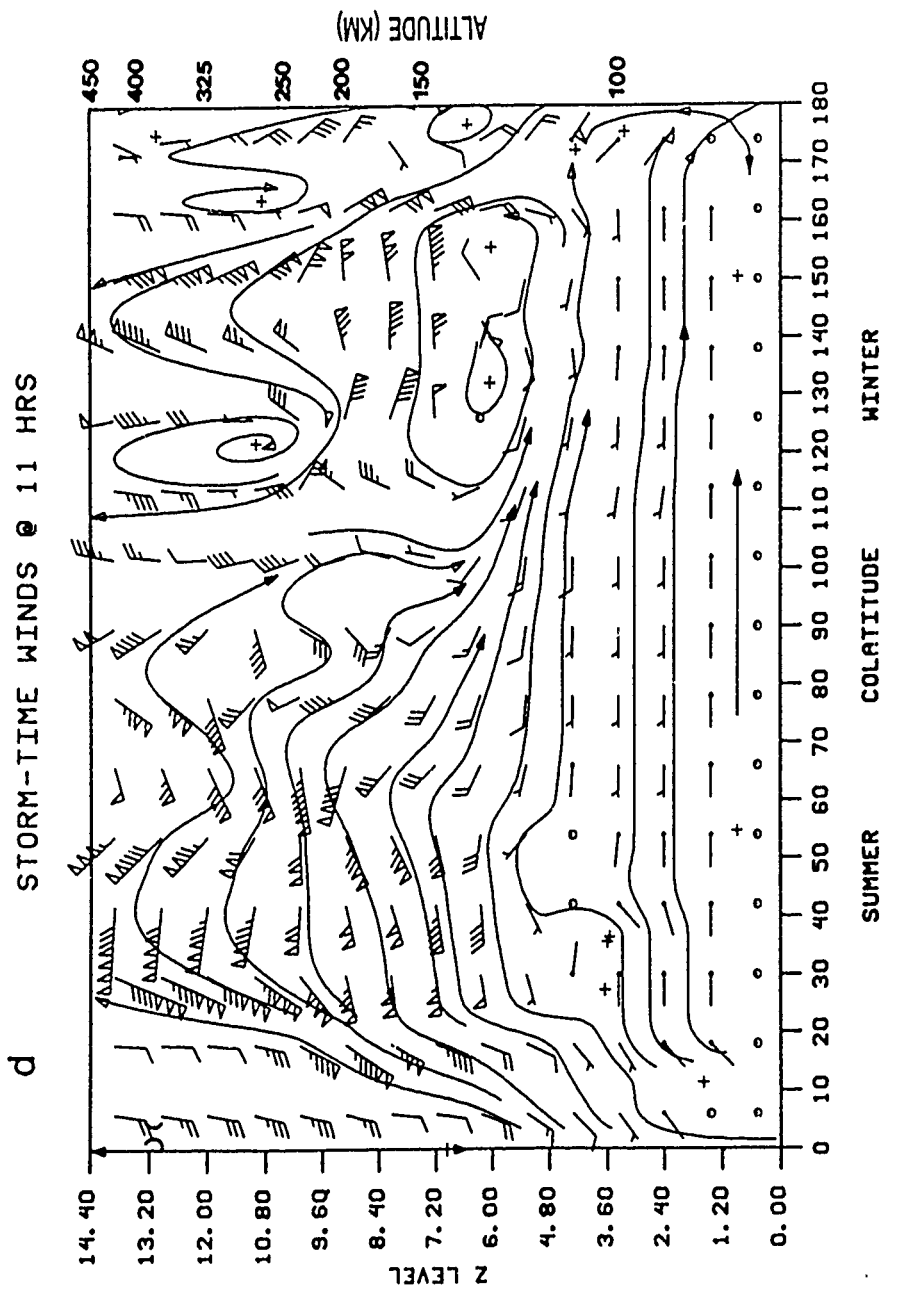
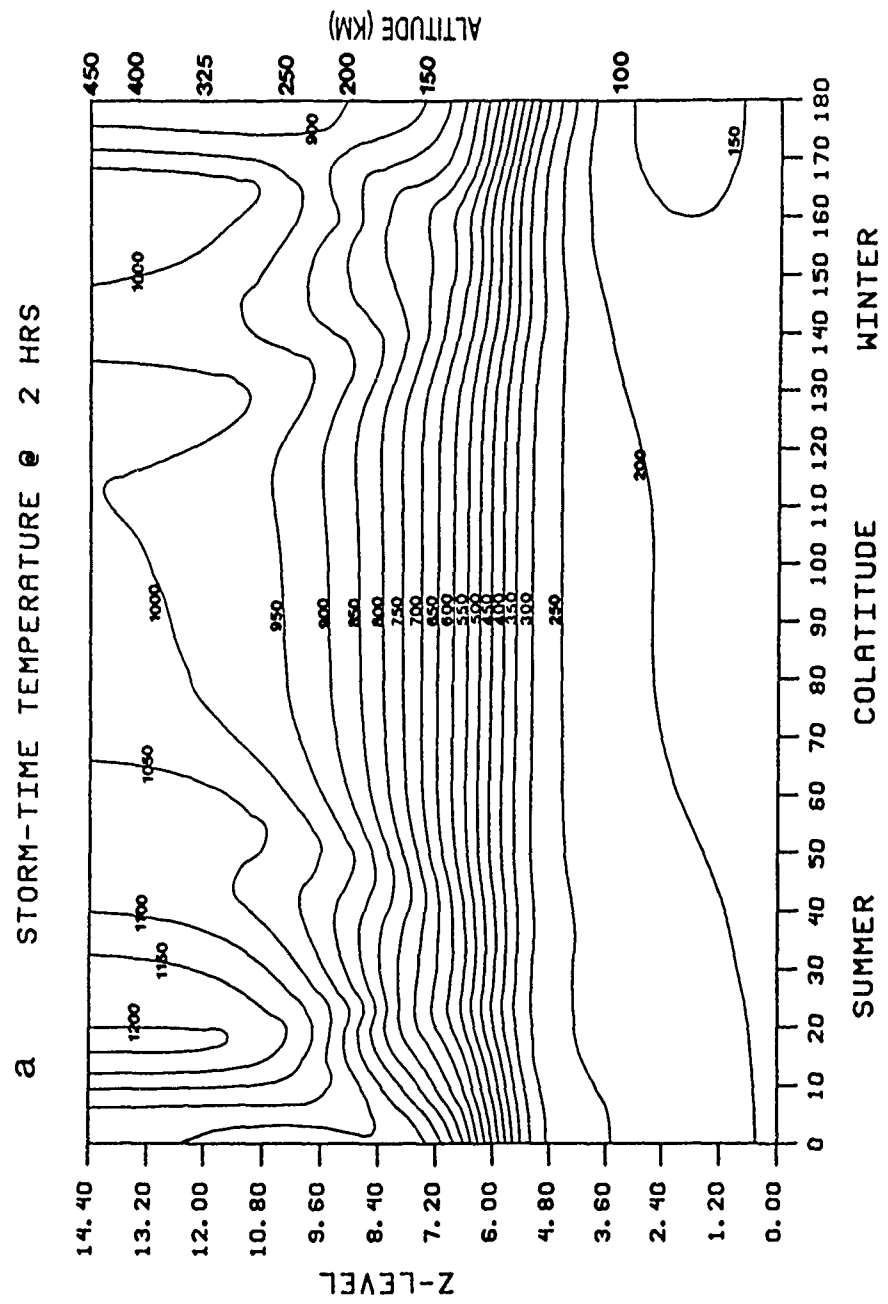


Figure 3.1d



**Figure 3.2a**

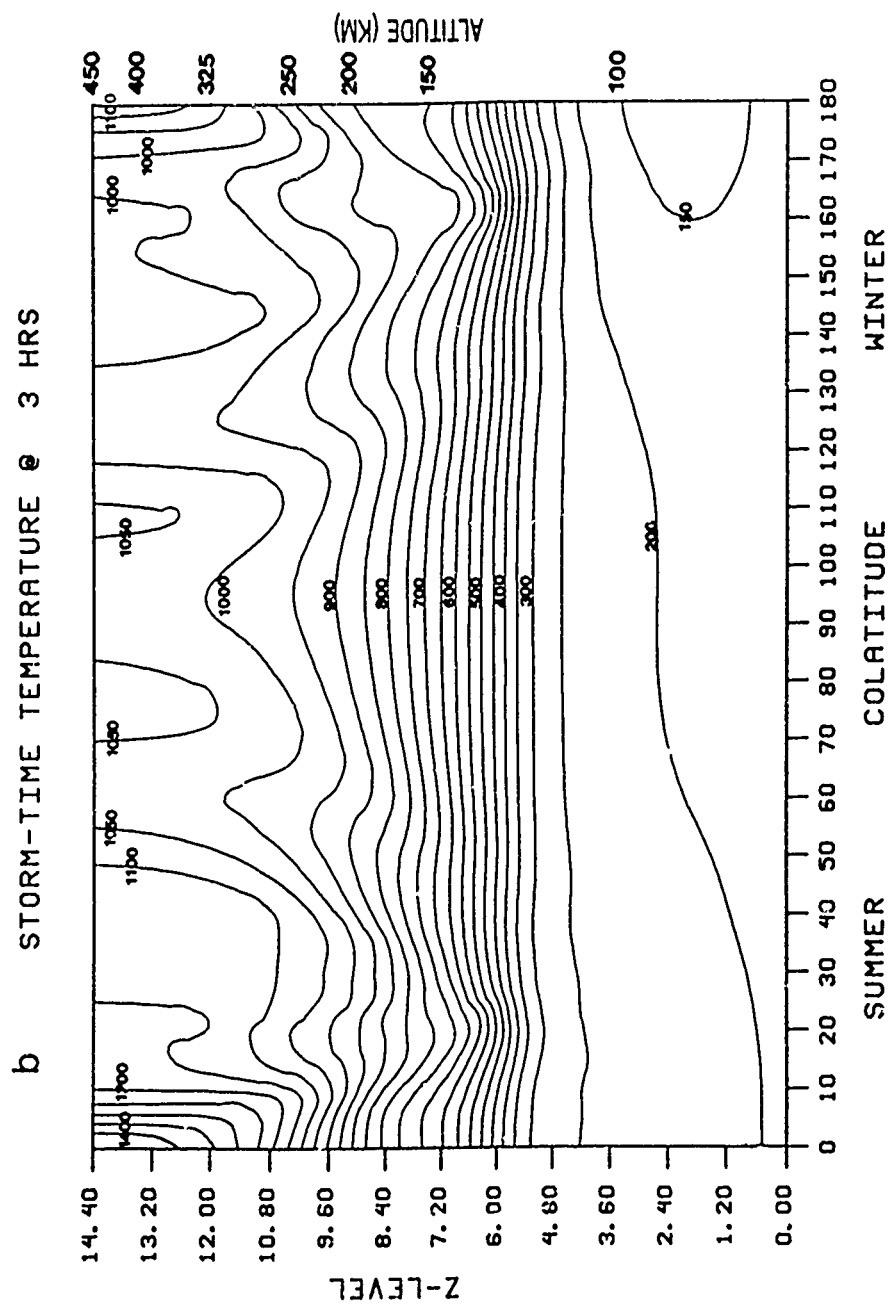


Figure 3.2b

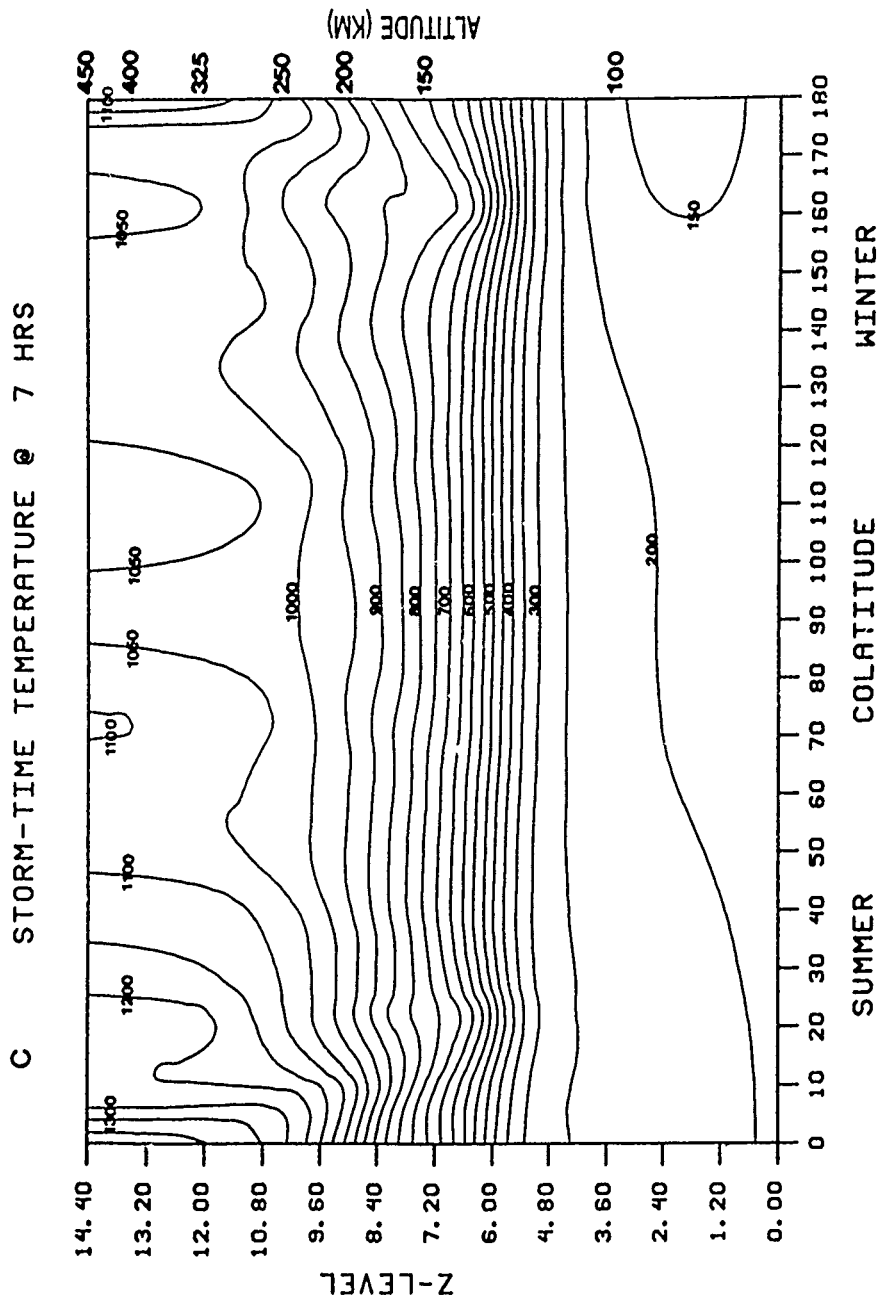


Figure 3.2c

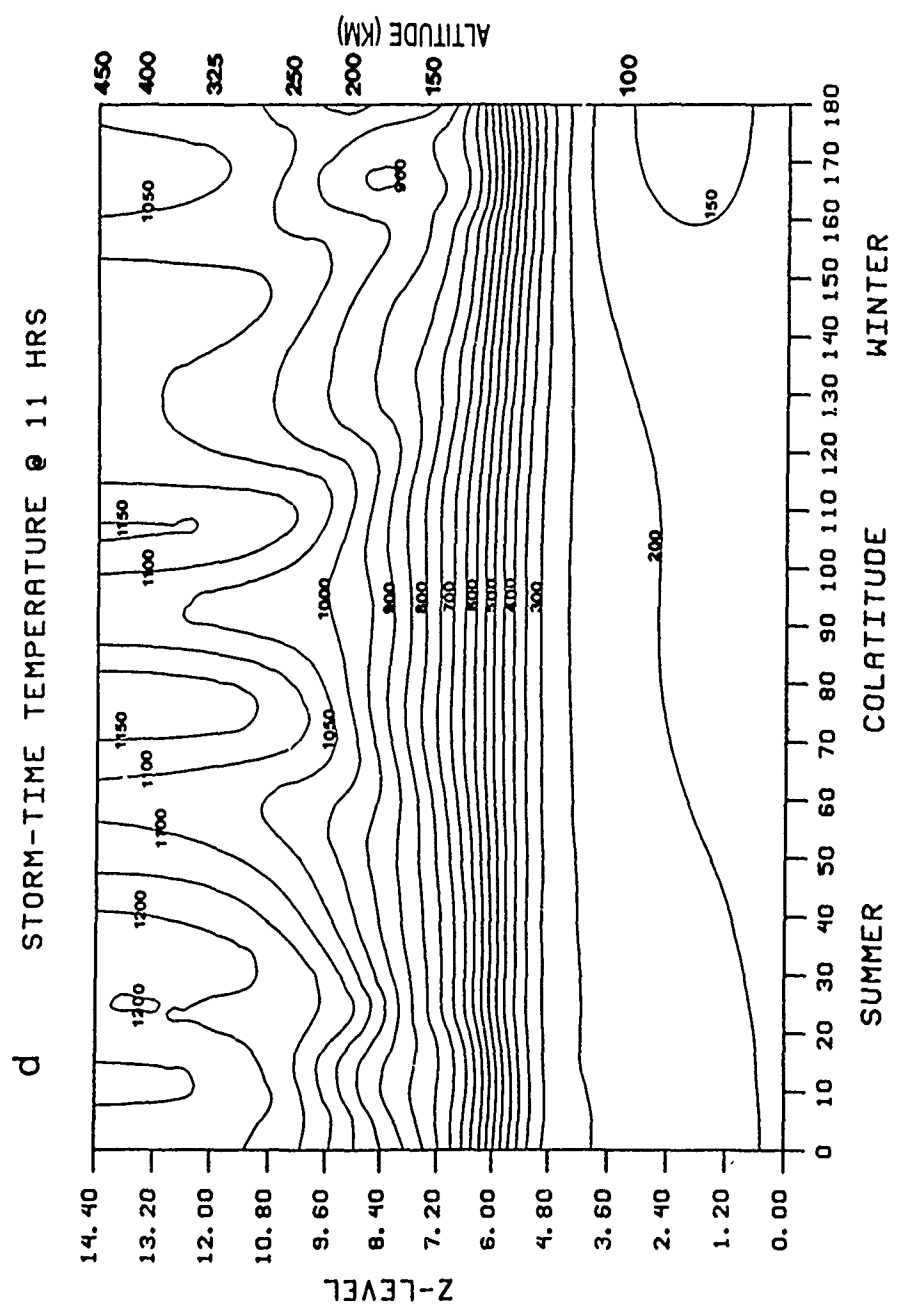


Figure 3.2d

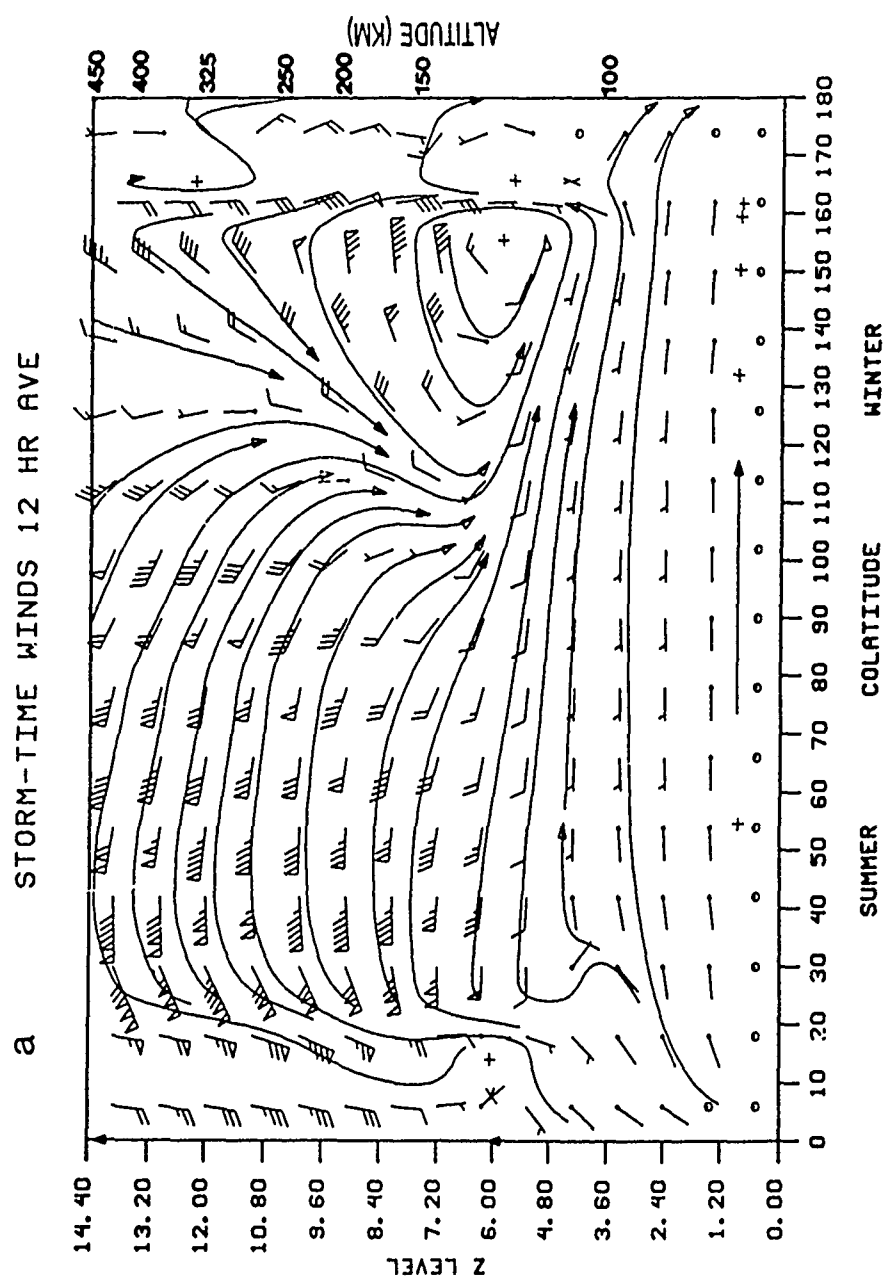


Figure 3.3a

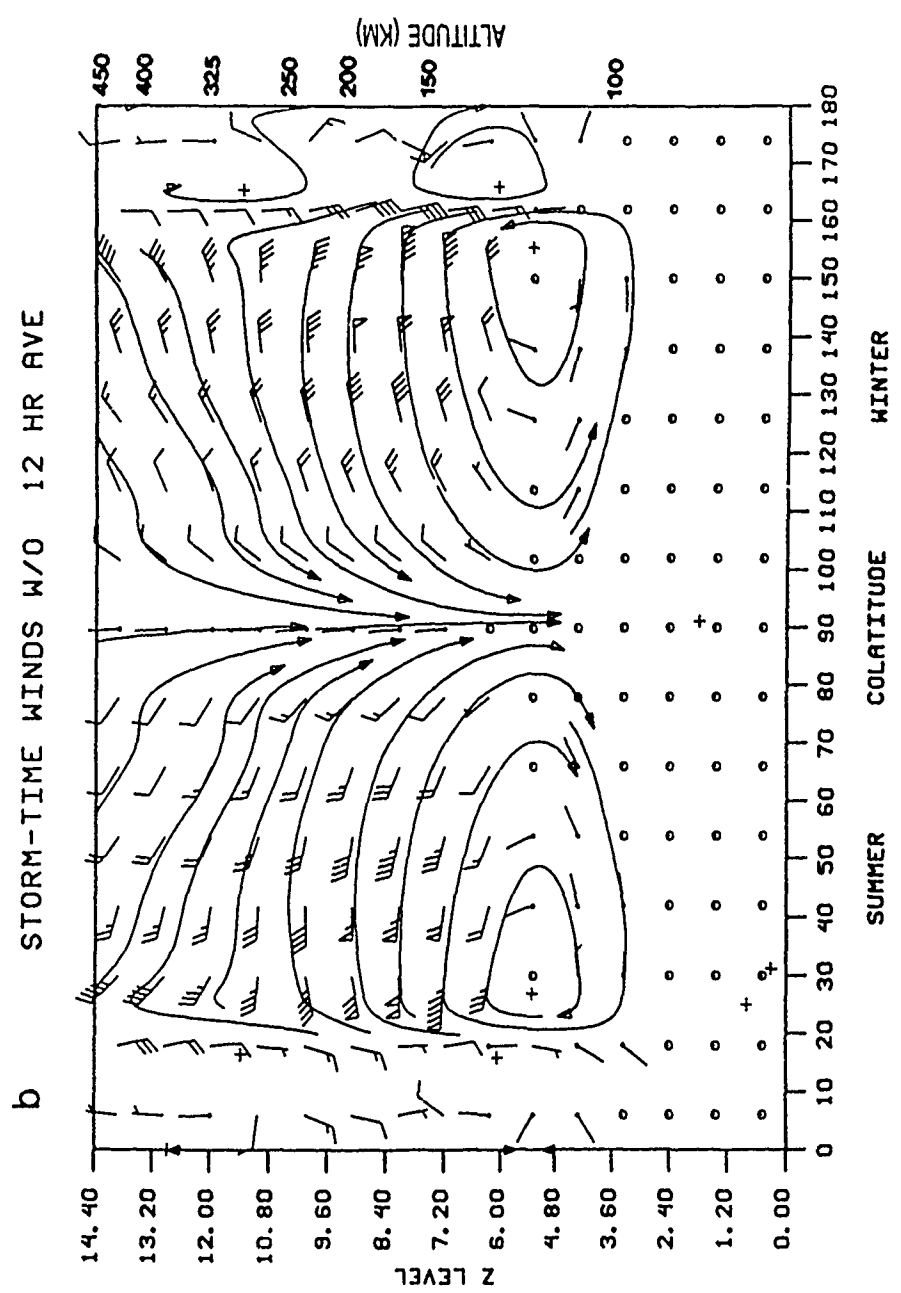


Figure 3.3b

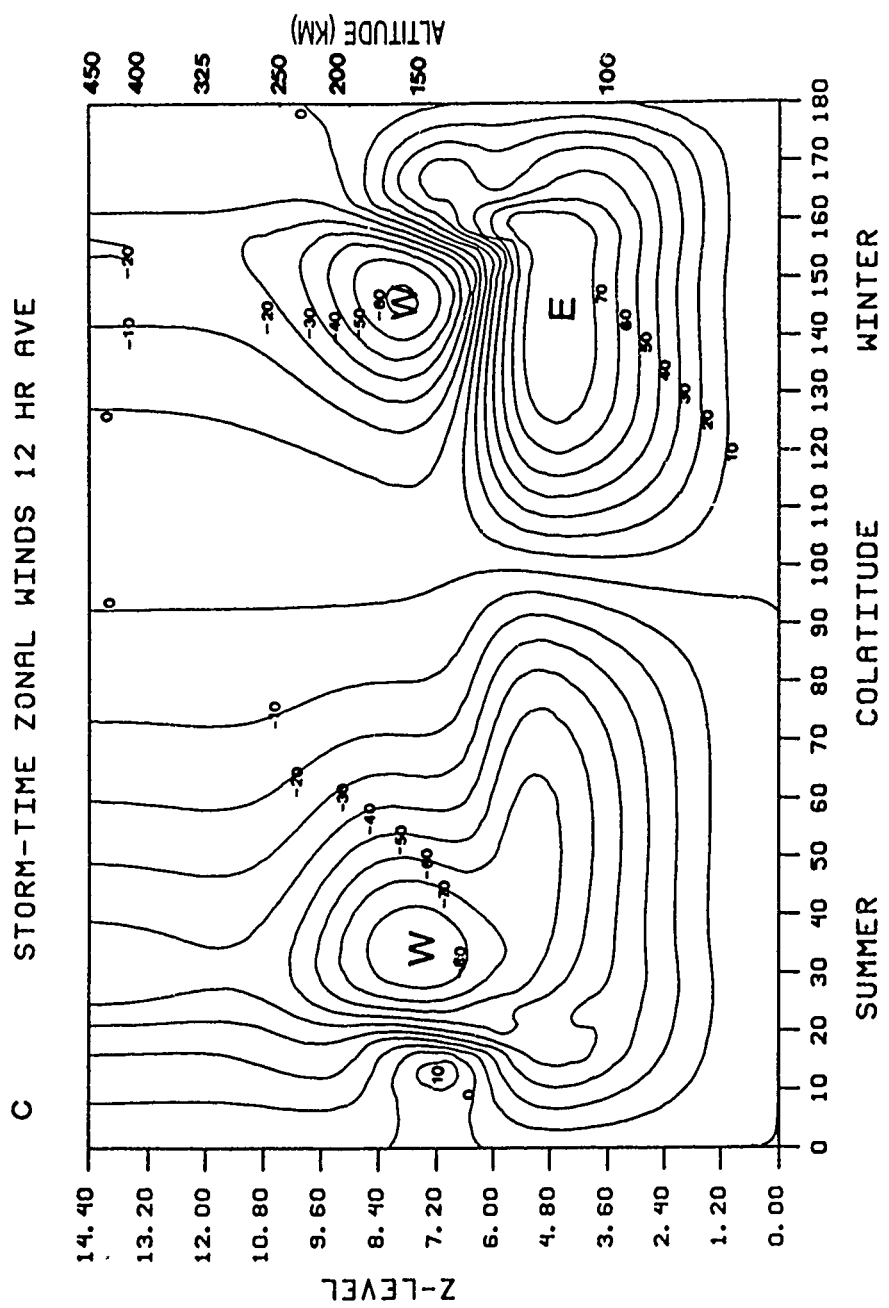


Figure 3.3c

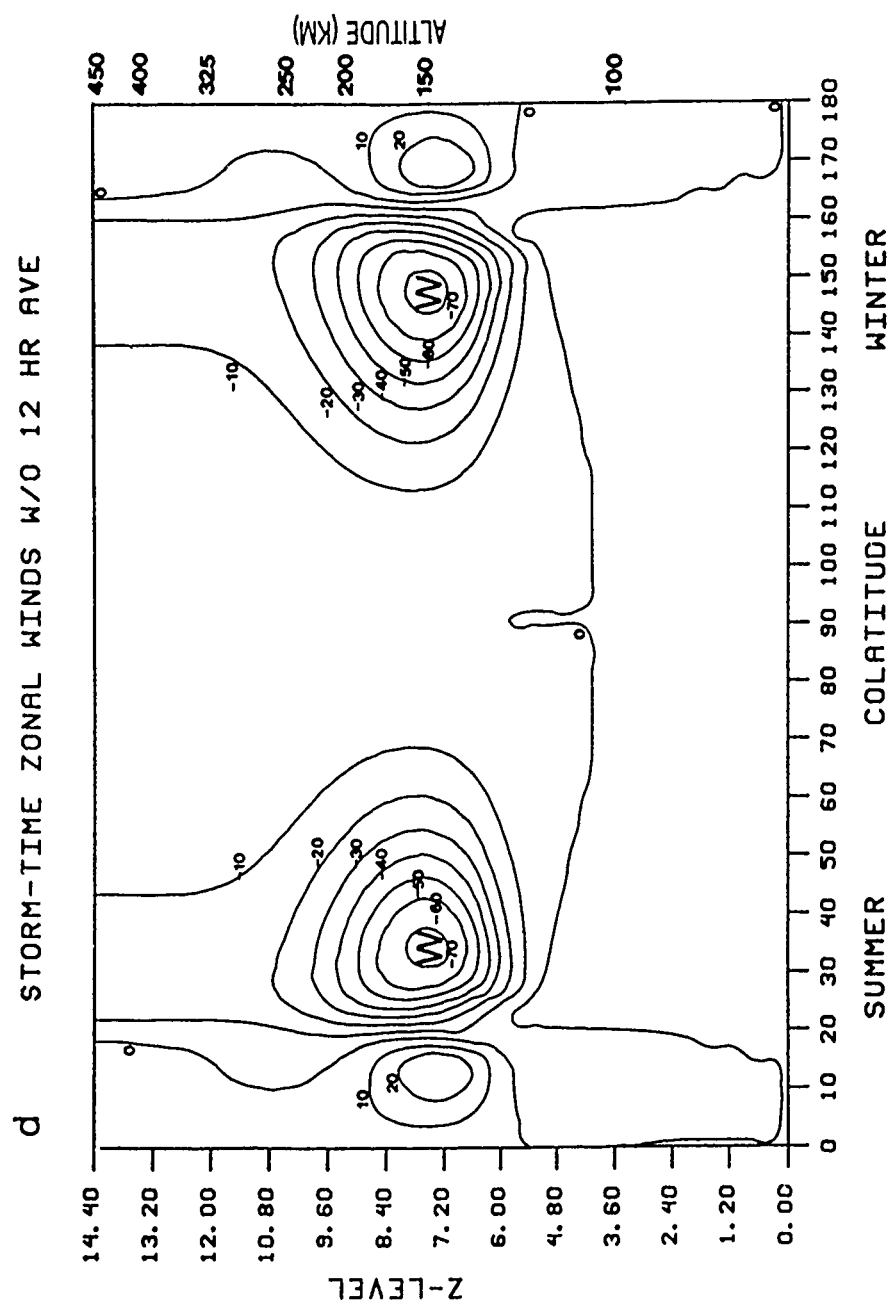


Figure 3.3d

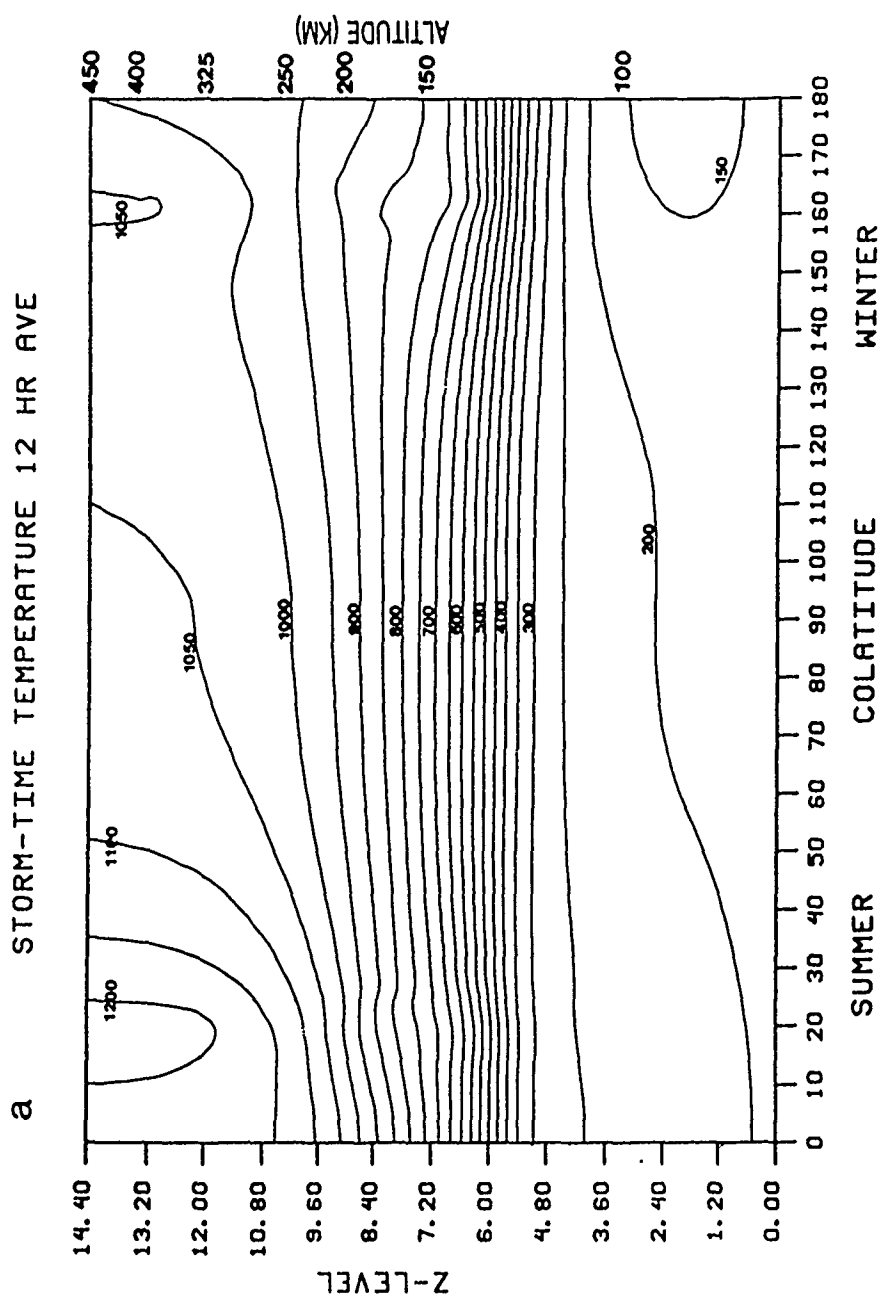


Figure 3.4a

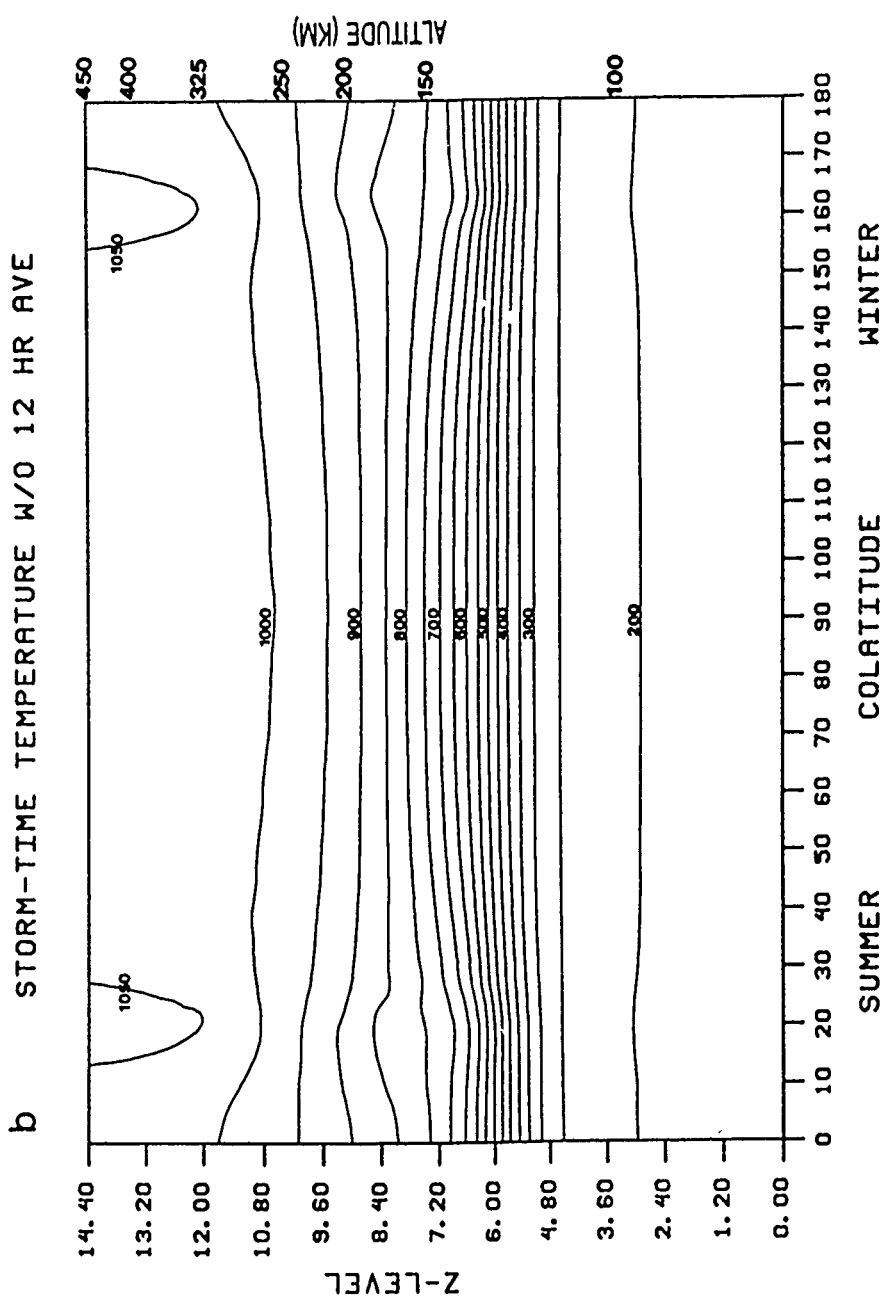


Figure 3.4b

STORM GENERATED WAVES W-COMPONENT

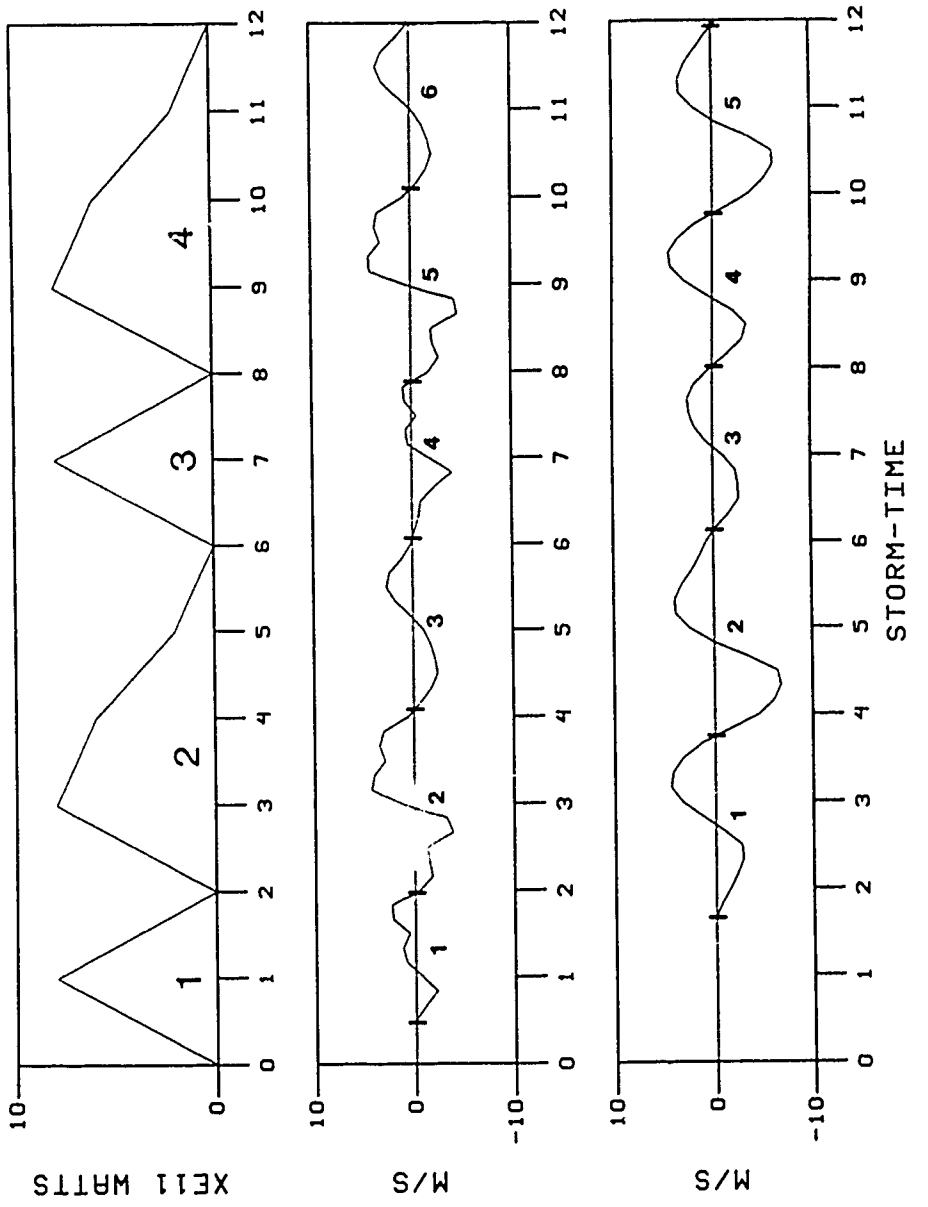


Figure 3.5a

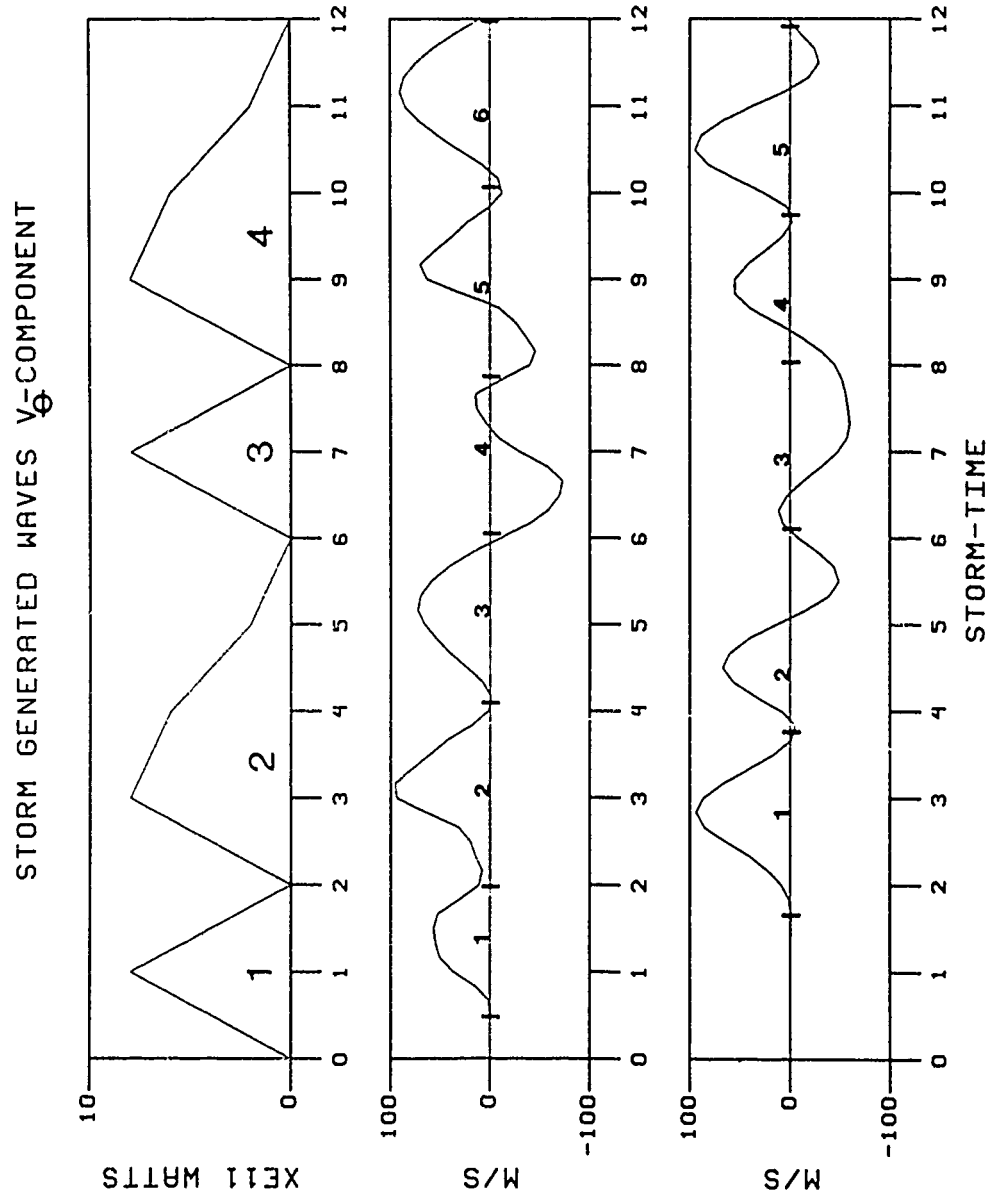


Figure 3.5b

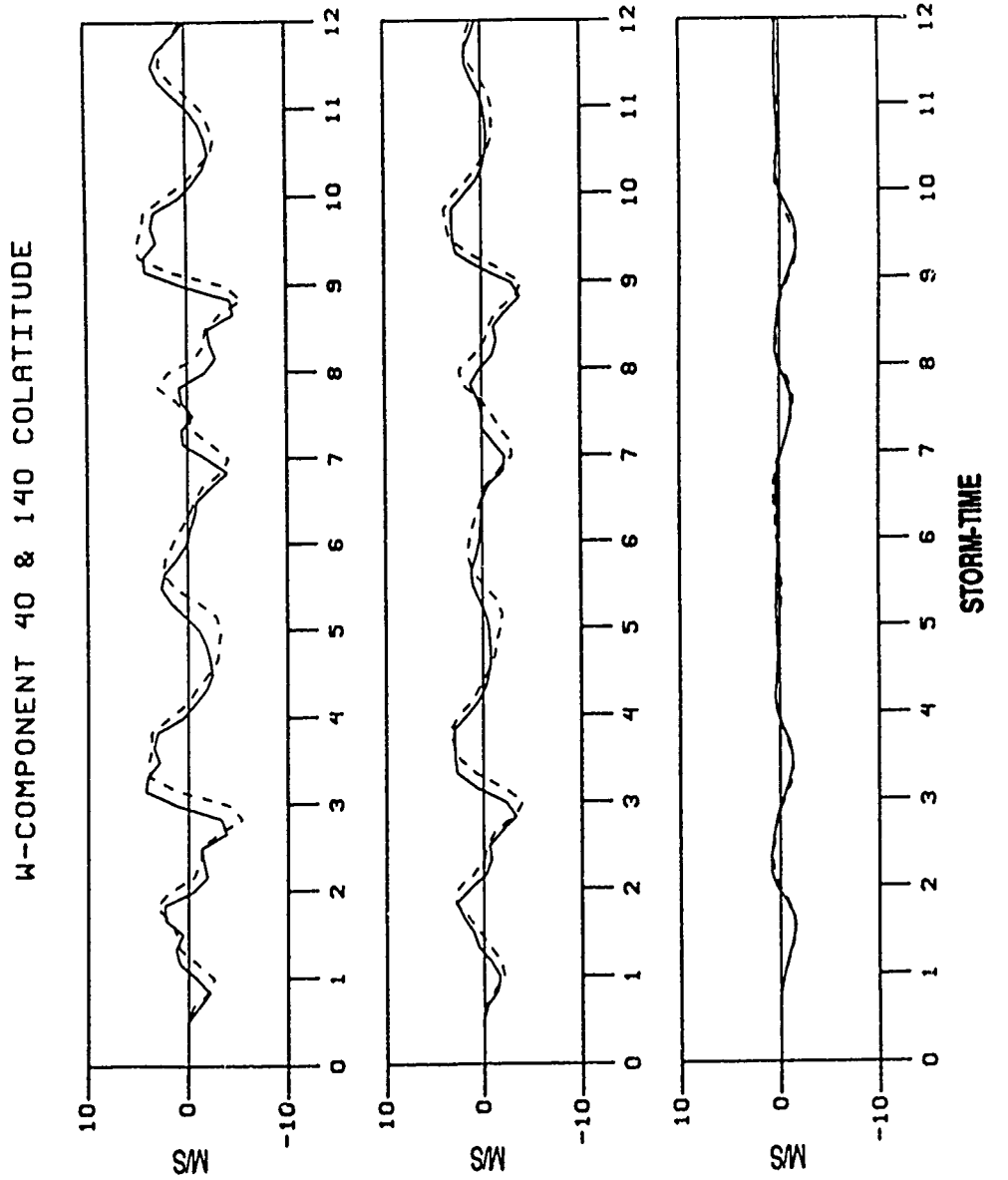
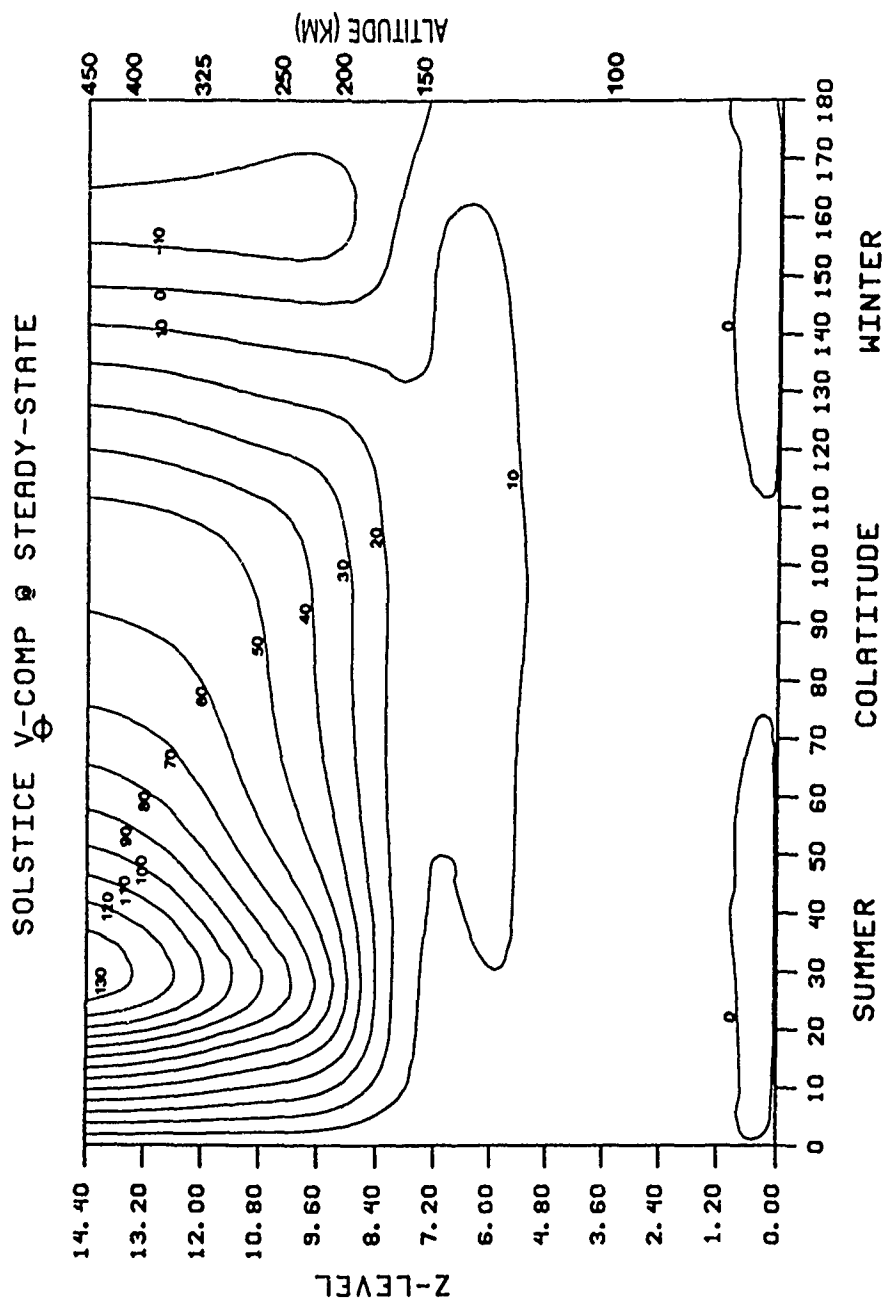


Figure 3.6



**Figure 3.7**

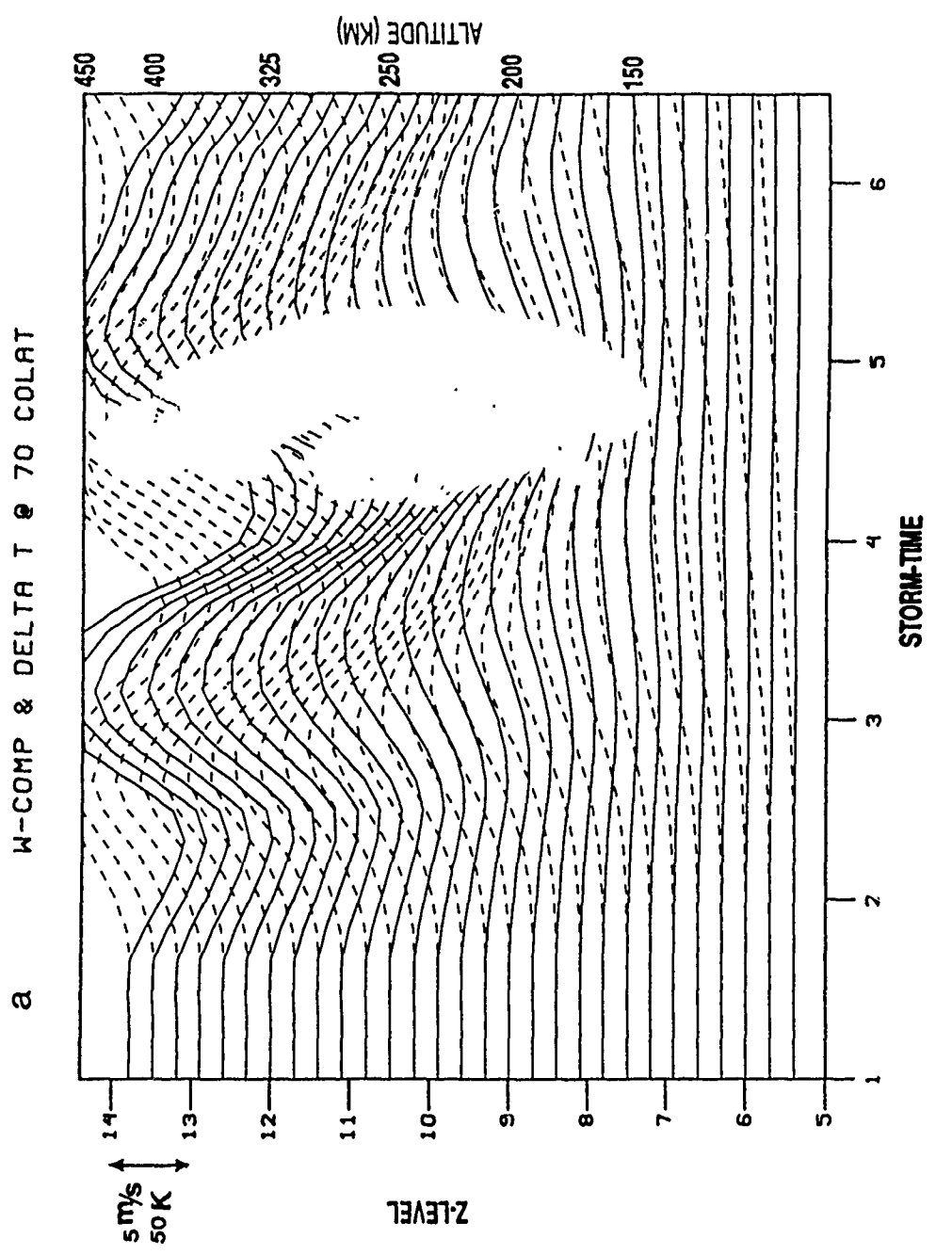


Figure 3.8a

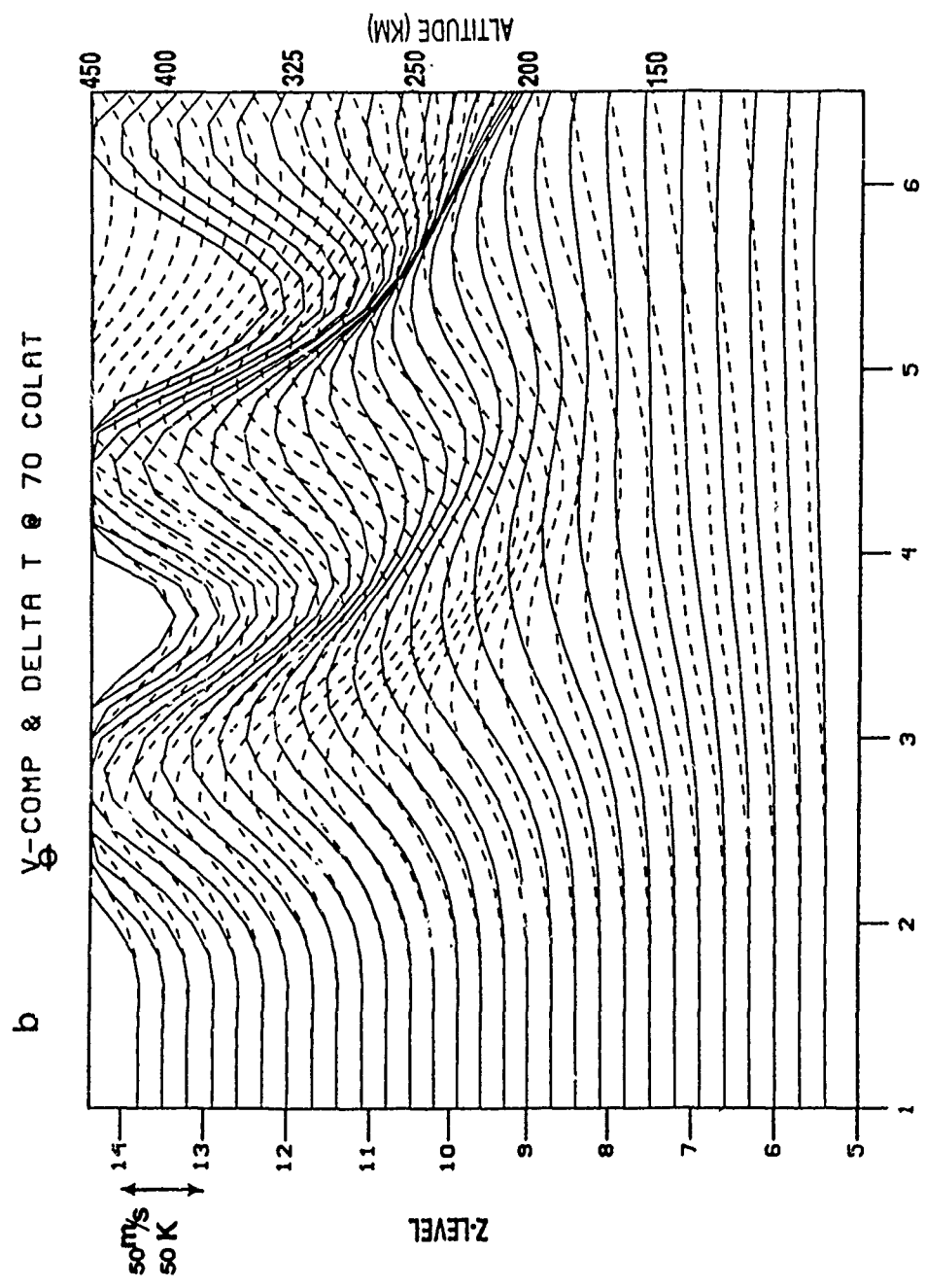


Figure 3.8b

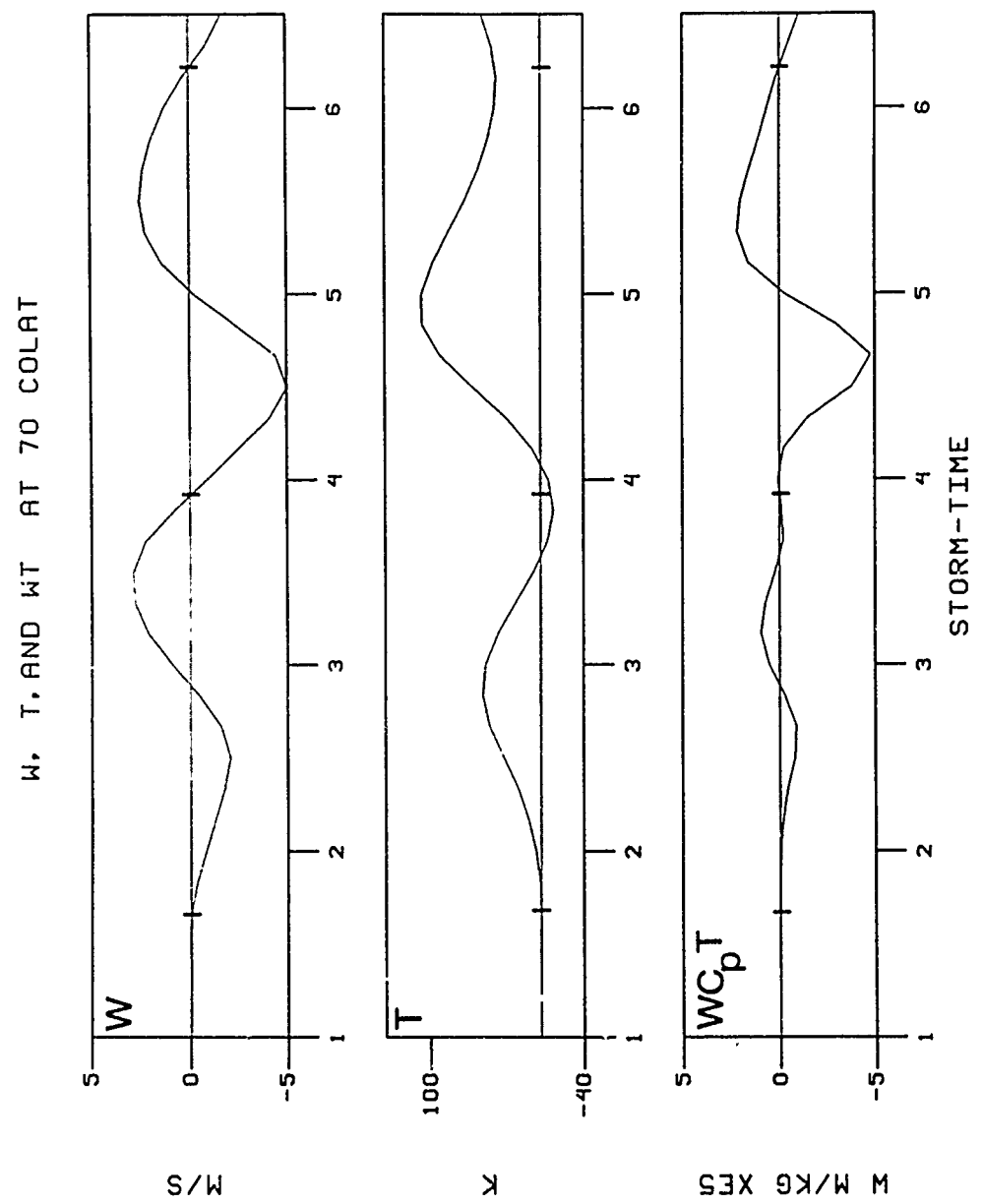


Figure 3.9a

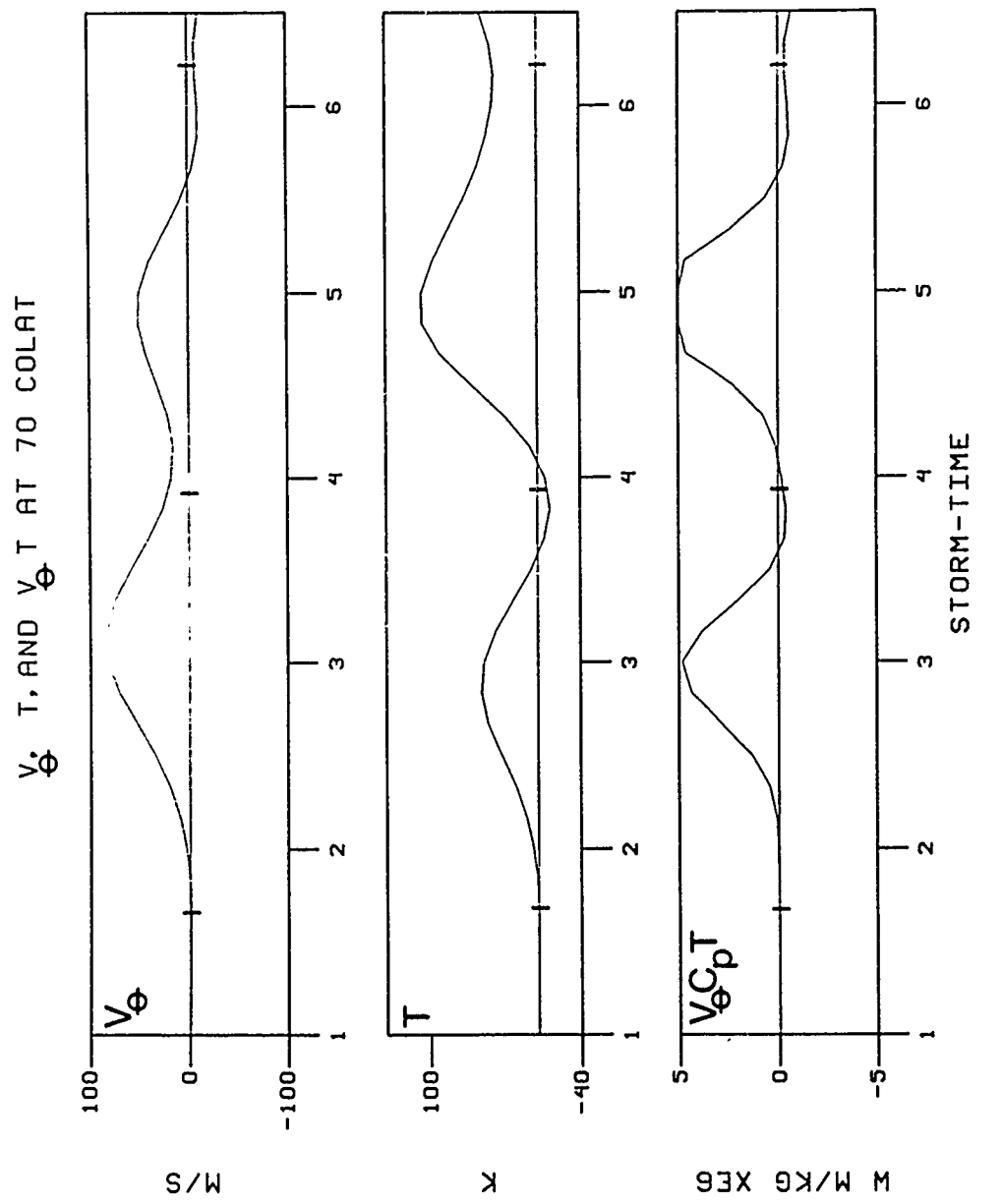


Figure 3.9b

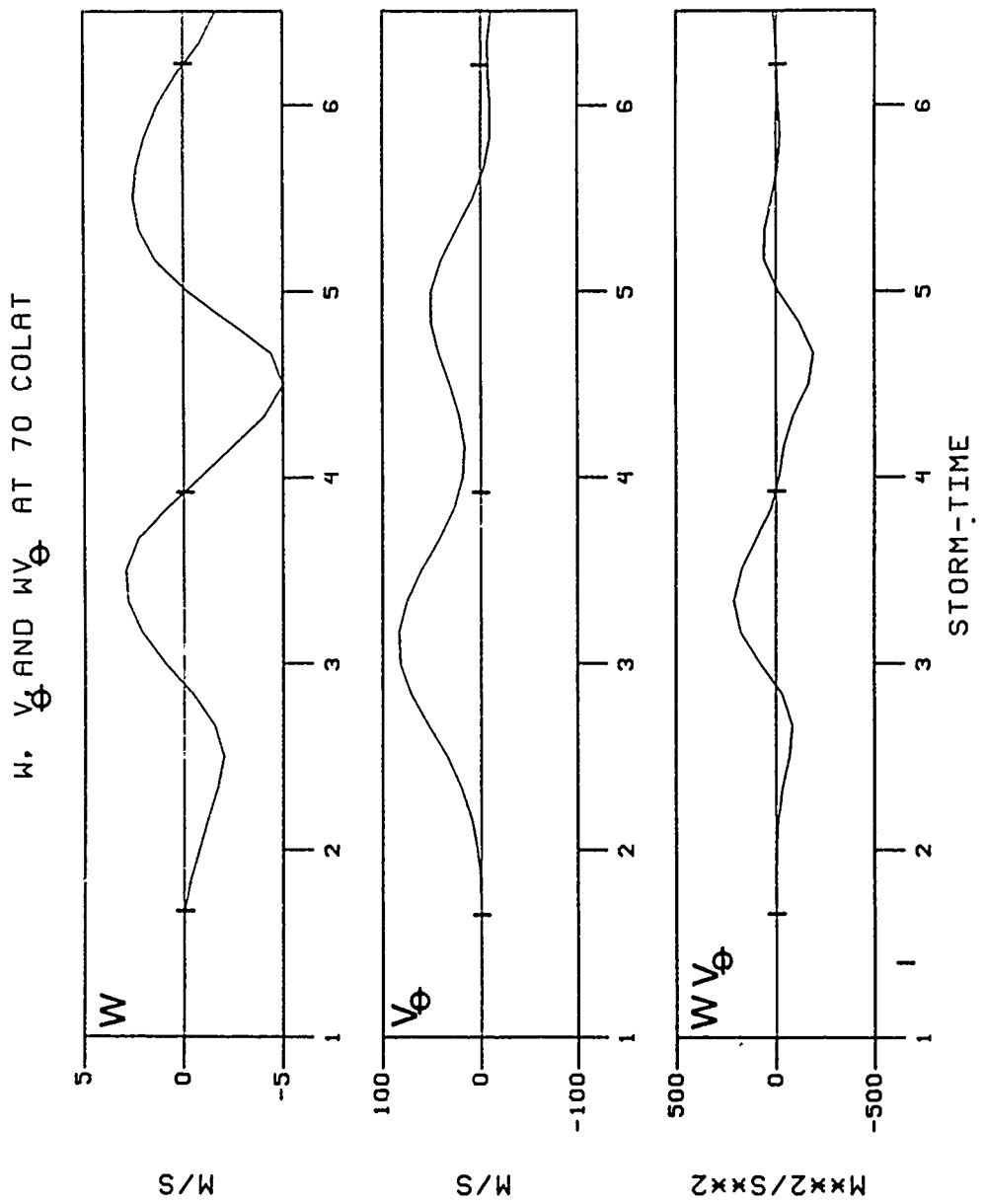


Figure 3.9c

## CHAPTER IV

## WAVE-MEAN FLOW INTERACTION

## 4.1 EFFECTS ON CIRCULATION

To investigate the effects of wave-mean flow interaction for our model storm, we partition the dependent variables ( $v_\phi$ ,  $v_\theta$ ,  $w$ , and  $T$ ) in the momentum and thermodynamic energy equations into a time-averaged part and an eddy part, defined as the deviation from the time-average. The time-averaged part is taken to be the storm-time response, averaged over 12 hours, of the thermosphere with seasonal background winds and temperatures. (In the following discussion, we use the words eddies and waves interchangeably.) This partition yields:

$$\begin{aligned} v_\phi &= \bar{v}_\phi + v'_\phi \\ v_\theta &= \bar{v}_\theta + v'_\theta \\ w &= \bar{w} + w' \\ T &= \bar{T} + T' \quad \text{with } \bar{T} = T_0 + \bar{T}_1 \end{aligned} \tag{4.1}$$

where the overbar represents the time average and the prime represents the deviation from this average. In addition,  $\bar{T}_1$  is the difference between the time-averaged ( $\bar{T}$ ) and initial ( $T_0$ ) temperatures.

We then substitute the dependent variables into the equations of motion (Eq. 2.1, 2.2, and 2.4) and the thermodynamic energy equation (Eq. 2.5), and average over a 12-hour period. With slight rearrangement the resulting time-averaged equations are;

The zonal momentum equation:

$$\begin{aligned}\frac{\partial \bar{v}_\phi}{\partial t} = & - \frac{\bar{v}_\theta}{a} \frac{\partial \bar{v}_\phi}{\partial \theta} - \frac{w}{a} \frac{\partial \bar{v}_\phi}{\partial z} - 2\Omega \bar{v}_\theta \cos \theta - \frac{\bar{v}_\phi \bar{v}_\theta}{a} \cot \theta \quad (4.2) \\ & - \frac{1}{a \sin \theta} \frac{\partial}{\partial \theta} (\bar{v}_\theta \bar{v}_\phi \sin \theta) - \frac{1}{p} \frac{\partial}{\partial z} (p w \bar{v}_\phi) - \frac{\bar{v}_\phi' v_\theta'}{a} \cot \theta \\ & + \bar{x}\end{aligned}$$

The meridional momentum equation:

$$\begin{aligned}\frac{\partial \bar{v}_\theta}{\partial t} = & - \frac{\bar{v}_\theta}{a} \frac{\partial \bar{v}_\theta}{\partial \theta} - \frac{w}{a} \frac{\partial \bar{v}_\theta}{\partial z} - \frac{1}{a} \frac{\partial \bar{\Phi}}{\partial \theta} - 2\Omega \sin \theta \bar{v}_\phi + \frac{\bar{v}_\phi^2}{a} \cot \theta \quad (4.3) \\ & - \frac{1}{a \sin \theta} \frac{\partial}{\partial \theta} (\bar{v}_\theta'^2) - \frac{1}{p} \frac{\partial}{\partial z} (p w \bar{v}_\theta') + \frac{\bar{v}_\phi'^2}{a} \cot \theta \\ & + \bar{y}\end{aligned}$$

Continuity equation:

$$\frac{1}{a \sin \theta} \frac{\partial}{\partial \theta} (\bar{v}_\theta \sin \theta) + \frac{1}{p} \frac{\partial}{\partial z} (p \bar{w}) = 0 \quad (4.4)$$

Thermodynamic energy equation:

$$\begin{aligned}\frac{\partial}{\partial t} (C_p T) = & - \frac{\bar{v}_\theta}{a} \frac{\partial}{\partial \theta} (C_p \bar{T}) - \frac{w}{a} \frac{\partial}{\partial z} (C_p \bar{T}) - R \bar{w} \bar{T} \quad (4.5) \\ & - \frac{1}{a \sin \theta} \frac{\partial}{\partial \theta} (C_p \bar{v}_\theta \bar{T} \sin \theta) - \frac{1}{p} \frac{\partial}{\partial z} C_p (p \bar{w} \bar{T}) - R \bar{w} \bar{T}'\end{aligned}$$

$$+ \bar{Q} + \bar{K} .$$

In practice, the time-averaged meridional circulation ( $\bar{V}_\theta$ ,  $\bar{w}$ ) described by the above equations was obtained as the average at fixed grid points of the instantaneous solutions of the model equations. This circulation, also referred to as the mean Eulerian circulation, is shown in Figure 3.3a. We can now alternatively consider the mean Eulerian circulation as driven by the forcing terms on the right-hand sides of the equations above. In doing so, it is convenient to separate the linear and non-linear forcing terms, and think of these terms as driving a mean linear circulation and a mean induced circulation, respectively.

The procedure that was adopted to obtain the mean linear circulation ( $\bar{V}_\theta^1$ ,  $\bar{w}^1$ ) was to run the model with storm-time energy inputs reduced to 1/100th of their original strength. It was assumed that the resulting model response would be essentially linear. This response is scaled back up by a factor of 100 and is shown in Figure 4.1 as the mean linear circulation

We notice that the mean Eulerian circulation (Figure 3.3a) and the mean linear circulation are remarkably similar in both structure and magnitude. Both circulations exhibit a two-celled structure with the larger summer hemisphere cell extending across the equator, meeting a reversed winter cell at 100-120° colatitude, and resulting in a region of strong downward motion there. The similarity of these circulations

implies that the mean linear circulation accounts for a major part of the mean Eulerian circulation.

The difference between the mean Eulerian and mean linear circulations is the mean induced circulation  $(\bar{v}_\theta^*, \bar{w}^*)$  shown in Figure 4.2. The mean induced circulation results from the non-linear forcing terms on the right-hand sides of the time-averaged momentum and thermodynamic energy equations (4.2, 4.3, 4.5). The non-linear terms consist of two types: those involving the products of two mean quantities (e.g.  $\bar{w} \frac{\partial}{\partial z} \bar{v}_\theta$ ) and those involving the products of two eddy quantities (e.g.  $\frac{1}{p} \frac{\partial}{\partial z} (\bar{p} \bar{w}' \bar{v}_\theta')$ ). Detailed calculations show, however, that the eddy non-linear terms are considerably more important in forcing the induced circulation than the mean non-linear terms, except in the region of storm-time forcing. Neglecting the mean non-linear terms, the governing equations for the induced circulation are:

$$\begin{aligned} \overline{\frac{\partial v_\theta^*}{\partial t}} &= - \frac{1}{a} \frac{\partial \bar{\Phi}^*}{\partial \theta} - \frac{1}{a \sin \theta} \left( \overline{v_\theta'^2} \sin \theta \right) - \frac{1}{p} \frac{\partial}{\partial z} \left( \bar{p} \overline{v_\theta' w'} \right) \\ &\quad + \frac{\overline{v_\theta'^2}}{a} \cotan \theta, \quad \text{where } \overline{\Phi^*} = \int \overline{R T^*} dz . \end{aligned} \quad (4.6)$$

$$\frac{1}{a \sin \theta} \frac{\partial}{\partial \theta} \left( \overline{v_\theta^*} \sin \theta \right) + \frac{1}{p} \frac{\partial}{\partial \theta} \left( \overline{w^* p} \right) = 0 . \quad (4.7)$$

$$c_p \overline{\frac{\partial T^*}{\partial t}} = - \overline{R w' T'} + \frac{1}{p} \frac{\partial}{\partial z} c_p \left( \overline{p w' T'} \right) - \frac{1}{a \sin \theta} \left( c_p \overline{v_\theta' T' \sin \theta} \right) . \quad (4.8)$$

Figure 4.2 shows that the most prominent features of the induced circulation are the two cells on either side of the equator, at altitudes below 200 km. These cells have the same sense of rotation as the storm-time mean Eulerian circulation cells (Figure 3.3) and therefore, make a contribution to the strengths of the latter. Above 200 km, the induced circulation tends to split into three or more cells of more limited extent in colatitude. It is important to remark, in this context, that the above mentioned features of the induced circulation do not substantially change if we adopt somewhat different averaging periods from the 12 hour period chosen here. They are, therefore, robust features of the storm-time dynamics.

#### 4.2 HEAT SOURCES AND SINKS

The mean Eulerian, the mean linear, and the mean induced circulations set up their own heat sources and sinks. These heat sources and sinks generated by the vertical and horizontal motions associated with these circulations are expressed, in what follows, as equivalent temperature changes and are compared with one another.

The equivalent temperature change ( $\Delta T$ ) produced by the mean Eulerian circulation ( $\bar{V}_\theta$ ,  $\bar{w}$ ) over a period  $\Delta t = 12$  hours is:

$$\Delta T = \frac{\Delta t}{C_p} \left( -R\bar{w}T - \bar{w} \frac{\partial}{\partial z} (C_p \bar{T}) - \frac{\bar{v}_\theta}{a} \frac{\partial}{\partial \theta} (C_p \bar{T}) \right) \quad (4.9)$$

The resulting pattern shown in Figure 4.3 exhibits alternating regions of comparatively large and small temperature changes, forming three

"couplets", above 200 km between 40° and 140° colatitudes. For example, one such couplet pattern with maximum and minimum temperatures of 220° K and 160° K, respectively, occur over the equator.

For the mean linear circulation, the equivalent temperature changes over the 12-hour period can be similarly expressed as:

$$\Delta T^1 = \frac{\Delta t}{C_p} \left( -\bar{R} \bar{w}^1_T - \bar{w}^1 \frac{\partial}{\partial z} (\bar{C}_p \bar{T}) - \frac{\bar{v}_\theta^1}{a} \frac{\partial}{\partial \theta} (\bar{C}_p \bar{T}) \right) \quad (4.10)$$

The resulting pattern in Figure 4.4 shows an overall correspondence to temperature changes due to the mean Eulerian circulation. This includes the large temperature increase associated with the main region of descent at 110-120° colatitude. However, the couplet patterns of temperature changes associated with the mean Eulerian circulation at higher altitudes are not reproduced in the temperature changes due to the mean linear circulation.

The differences between Figures 4.3 and 4.4 are the equivalent temperature changes to be attributed to the induced circulation, and is shown in Figure 4.5. This difference pattern should capture the couplet patterns of temperature changes associated with the mean Eulerian circulation. The couplet patterns are, therefore, judged to be the signature of wave-mean flow interaction on the temperature field of the mean Eulerian circulation.

The equivalent temperature changes due to the induced circulation can now be compared to the changes produced by the mean eddy heat flux convergence (divergence):

$$\Delta T = \frac{\Delta t}{C_p} \left( -\overline{R_w T} - \frac{1}{p} \frac{\partial}{\partial z} \overline{C_p (p_w T)} - \frac{1}{a \sin \theta} \frac{\partial}{\partial \theta} (C_p \overline{V_\theta T} \sin \theta) \right) \quad (4.11)$$

These temperature changes are shown in Figure 4.6.

Comparison of Figures 4.5 and 4.6 shows that, at least in middle latitudes, regions of warming (cooling) due to the induced circulation roughly correspond to regions of cooling (warming) due to mean eddy heat flux divergence (convergence). However, this correspondence does not hold near the equator, where both the induced circulation and eddy heat flux convergence cooperate to produce a region of warming. This equatorial warming is on the order of 50-90° K above 150 km, and is 1/3 to 1/2 of the warming produced by the mean linear circulation. The equatorial warming due to the induced circulation alone is 40-60° K, and is roughly 1/4 to 1/3 of the warming due to the mean Eulerian circulation.

It is important to emphasize that the above discussion of temperature changes due to the different circulations is with respect to equivalent and not actual temperature changes. To discuss the actual temperature changes, we need to consider the dissipative effects of molecular viscosity and thermal conductivity. Our detailed heat budget calculations including these effects are not given here.

The non-cancellation of the thermal effects of the induced circulation and the mean eddy heat flux convergence (divergence) is due to the temporal terms  $(\overline{\partial V_\theta^* / \partial t}, \overline{\partial T^* / \partial t})$  on the left-hand side of the governing equations (4.6 and 4.8) for the induced circulation. These

terms signify that the mean acceleration of the induced circulation, in general, is non-zero and is influenced by the detailed time history of the fluctuations of the eddy flux convergences (divergences) and not merely by their mean values. The circumstances under which the acceleration terms will go to zero is, in fact, the content of the so called non-acceleration theorem discussed by several authors in slightly different contexts (Andrews, 1985; Charney and Drazin, 1961; Dunkerton, 1978, 1980.)

FIGURE CAPTIONS FOR CHAPTER IV

Fig. 4.1. The mean linear circulation (see text for definition).

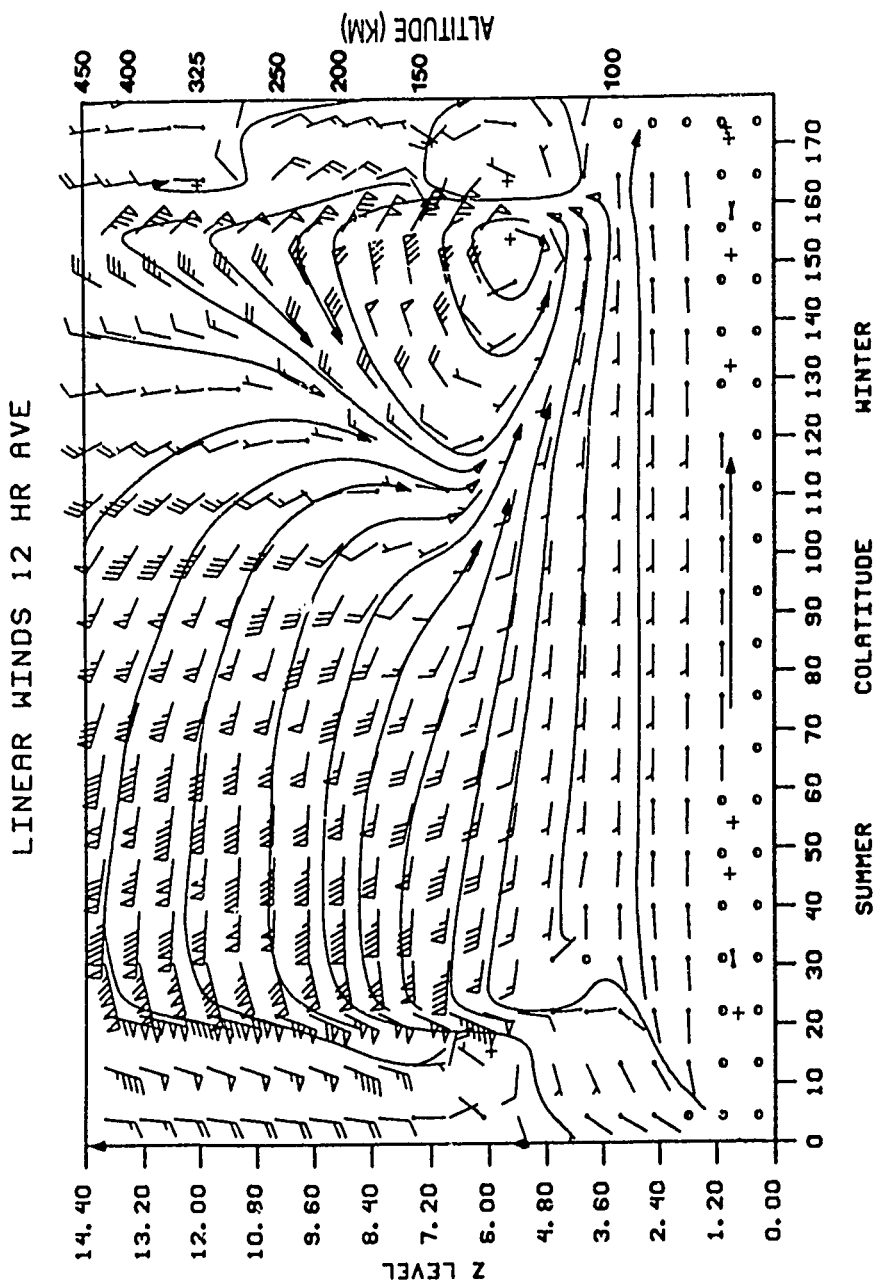
Fig. 4.2. The mean induced circulation (see text for definition).

Fig. 4.3. Heat sources and sinks due to the mean Eulerian circulation expressed as equivalent temperature changes. Notice that the source regions have been eliminated from this figure and from Figures 4.4, 4.5, and 4.6.

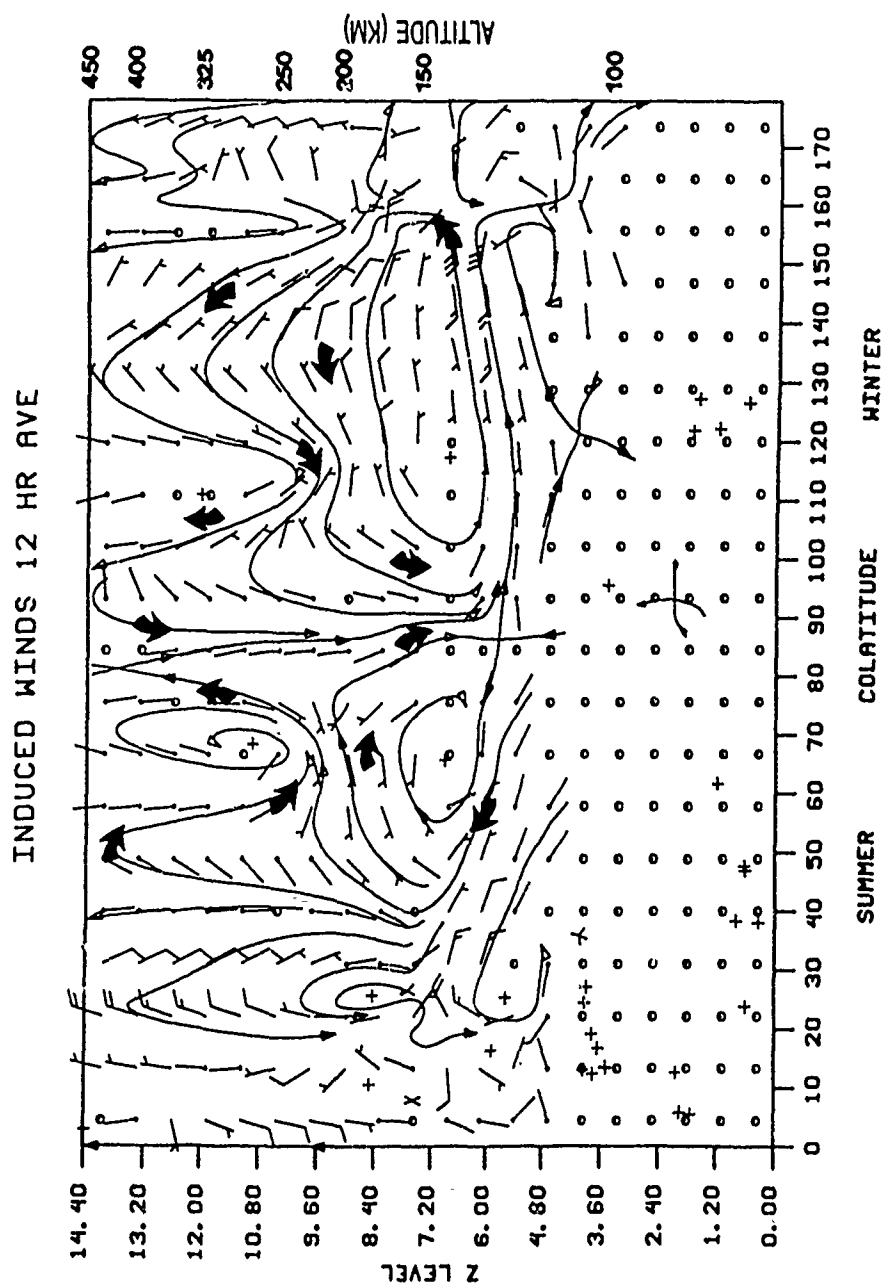
Fig. 4.4. Same as Figure 4.3 except due to the mean linear circulation.

Fig. 4.5. Same as Figure 4.3 except due to the mean induced circulation.

Fig. 4.6. Same as Figure 4.3 except due to the mean eddy heat flux convergences (divergences).

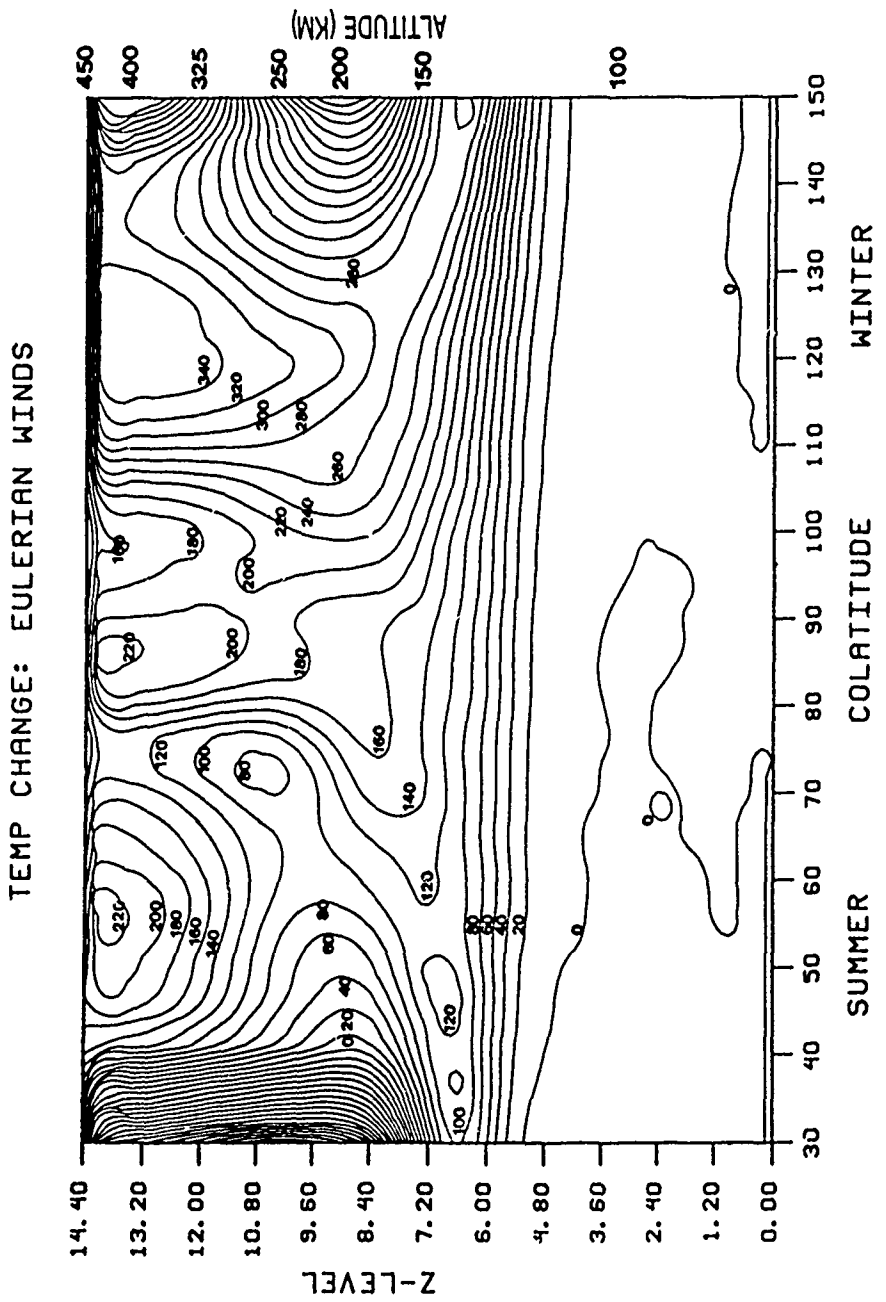


**Figure 4.1**



**Figure 4.2**

Figure 4.3



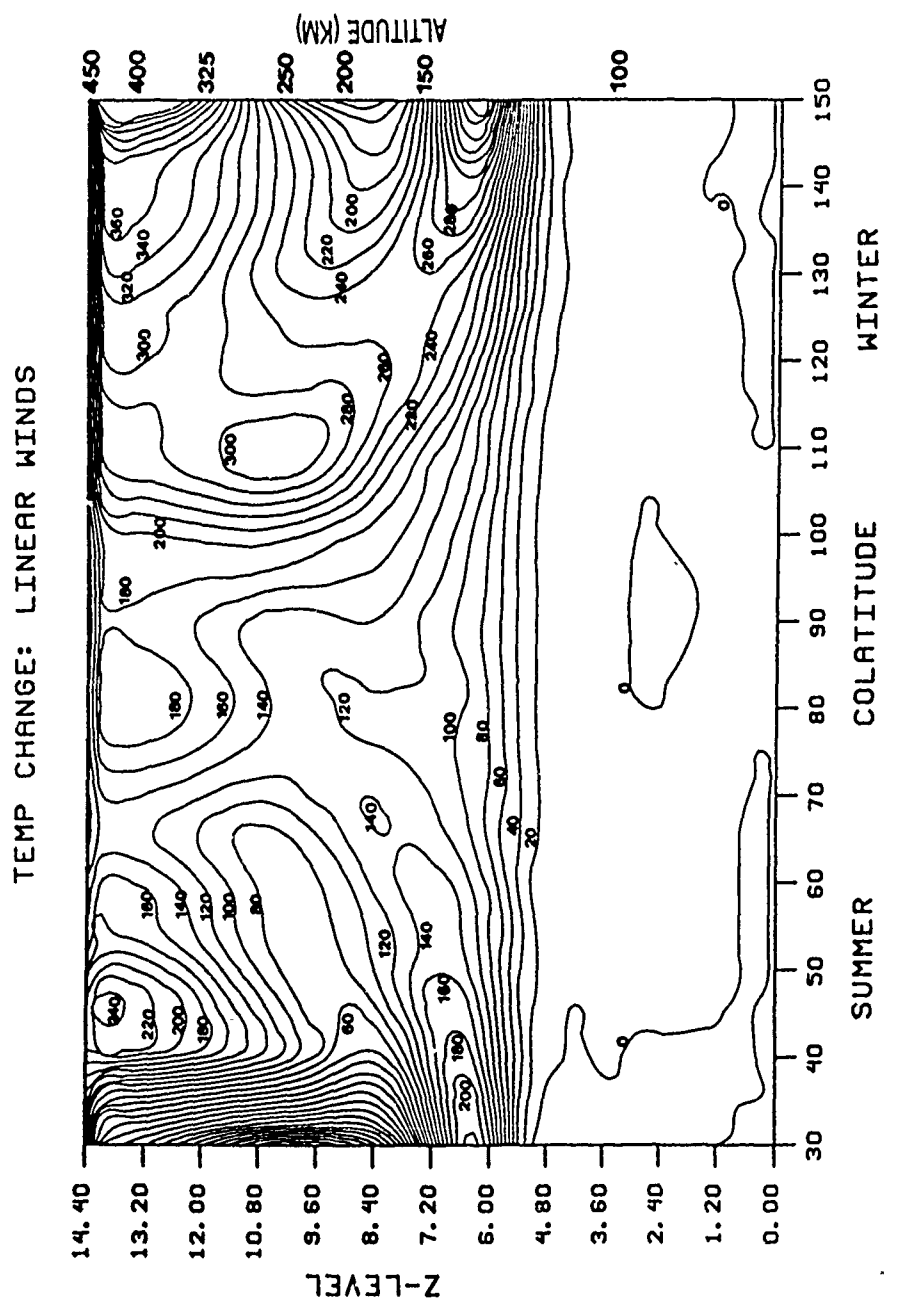


Figure 4.4

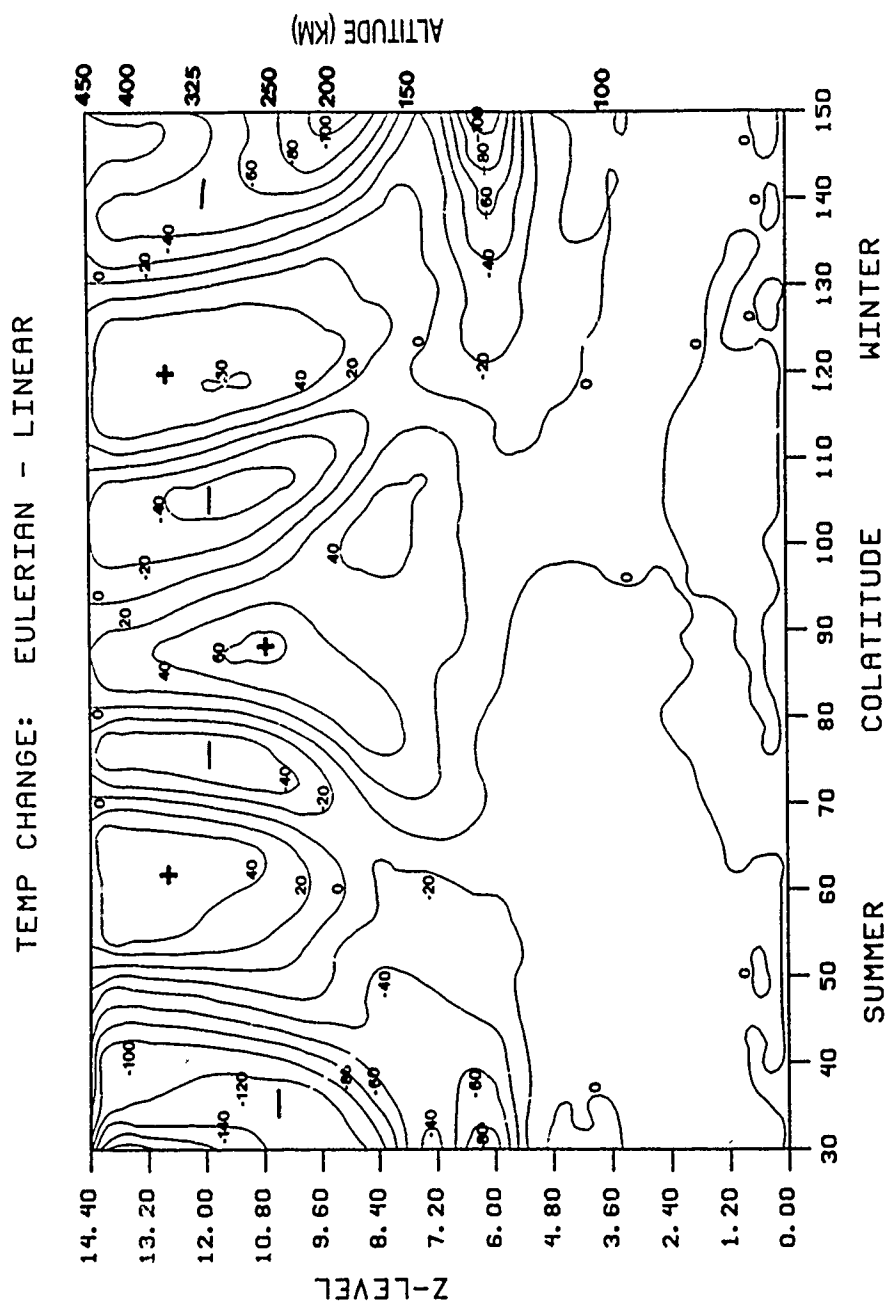
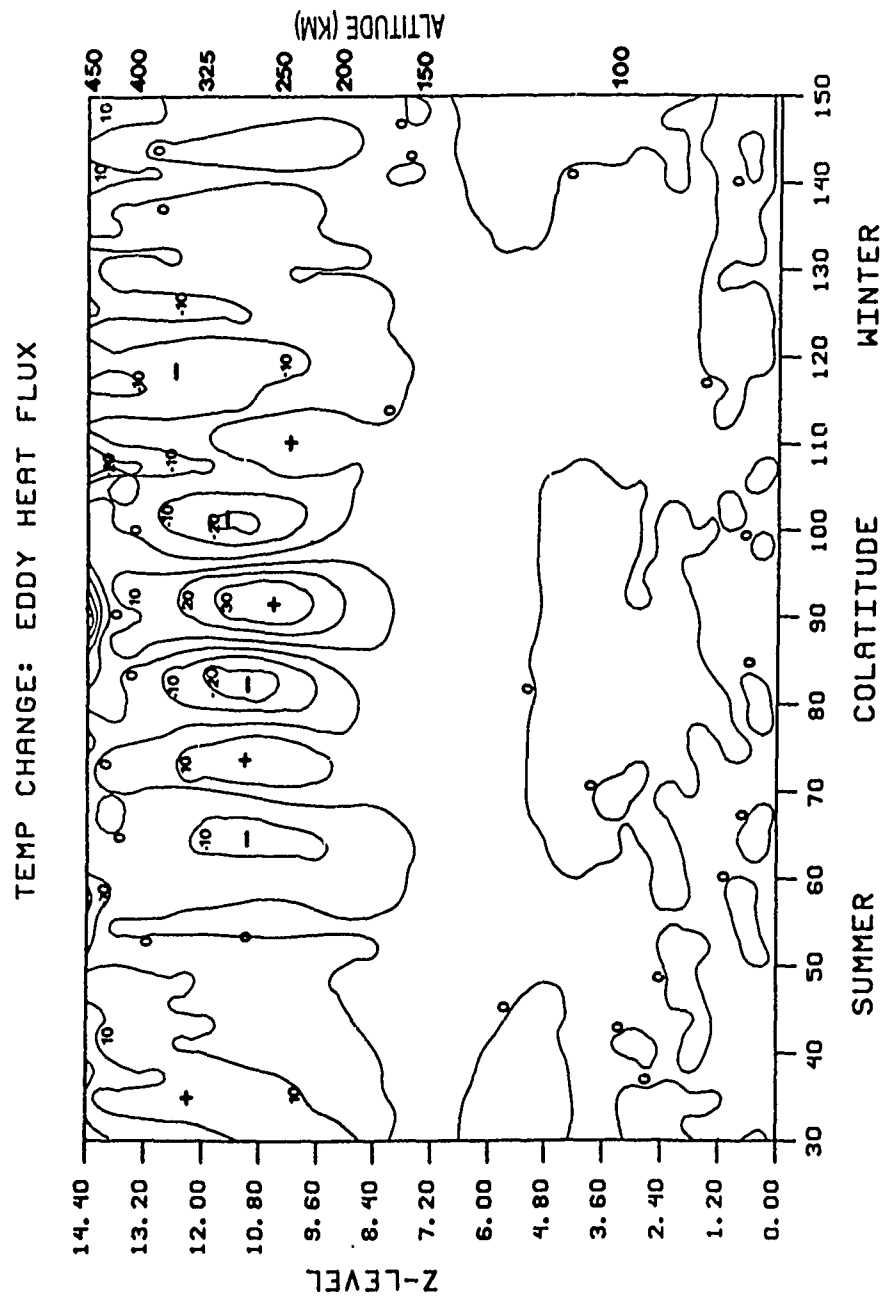


Figure 4.5



**Figure 4.6**

## CHAPTER V

### LAGRANGIAN MOTIONS, EULERIAN MOTIONS, AND STOKES DRIFT

#### 5.1 TRAJECTORY CALCULATIONS

As described in Chapter 3, the storm-time winds vary both in space and time. Because of these variations, the actual trajectory of an identified fluid marker, referred to as the Lagrangian trajectory, will be different from the mean Eulerian trajectory along the streamlines corresponding to the time-averaged wind vectors at fixed points in space.

In this paper, the Lagrangian trajectory calculations are performed using an iterative method. After fixing the starting position of the fluid marker on our model grid, we use the initial velocity field,  $v(t_0)$ , at that position to calculate the displacement,  $v(t_0)\Delta t$ , where  $\Delta t$  is a time increment of 10 minutes. We next find the new grid location of the marker at  $t_0 + \Delta t$ , where its velocity is  $v(t_0 + \Delta t)$ .  $v(t_0)$  and  $v(t_0 + \Delta t)$  are then averaged and used to obtain a better value for the displacement of the marker from its initial position. This procedure is repeated until the displacement from iteration to iteration does not vary significantly. We then use the marker's new position as the starting point for calculating the displacement for the next time increment. The trajectories are calculated in this manner for a maximum time period of 12 hours, and several such trajectories are shown in Figures 5.1 and 5.3.

Figure 5.1 shows the Lagrangian trajectory of the marker started

at 400 km and 70° colatitude. In this example it is assumed that the thermosphere is at rest except for the motion associated with the storm-generated waves. Five such waves are shown to influence the motion of the marker in the 12-hr period of storm simulation. At the end of this period, the marker is found to have moved a horizontal distance of approximately 1.5 degrees in colatitude (~150 km) and upward by about 3 km. This displacement of the marker between its starting and ending positions is marked by an arrow, labelled  $\vec{L}$ , and is its Lagrangian displacement.

Figure 5.2 shows the Lagrangian trajectories of the marker started at a different location (110° colatitude, 257 km altitude). In this case, the marker is influenced both by the waves and the storm-time meridional circulation. We can, therefore, distinguish between the net Lagrangian displacement and the net Eulerian displacement of the marker in a given time interval. In Figure 5.2a this time interval is chosen to be the time of passage of the first wave, and in Figure 5.2b, of the first two waves. In each case, the net Lagrangian and net Eulerian displacements are indicated by the vectors  $\vec{L}$  and  $\vec{E}$ , respectively.

Figure 5.3 gives examples of the Lagrangian and Eulerian motions of markers started at the same altitude (~257 km) but at different colatitudes (40°, 80°, 110°). Figure 5.3a is for the case for storm-generated waves and circulation alone, whereas Figure 5.3b includes the seasonal background meridional circulation as well. Figure 5.3a illustrates the following features: 1) Individual air parcels originat-

ing near the heat source region do not have time to reach the equator in the 12-hr duration of the storm. They can at most travel a horizontal distance of 15° in colatitude (~1500 km). 2) At intermediate colatitudes, air parcels move generally downward and equatorward. 3) Near the equator, the air parcel transport is predominately downward, and is initiated with a time delay of approximately 2 to 3 hours after the beginning of the storm, signalling the first arrival of the storm-generated waves.

The differences in the above description, brought about by the inclusion of the seasonal background winds, are the larger meridional displacements (~35° in colatitude near the heat source region) of air parcels, and the shift in location, away from the equator, of the region of maximum vertical descent.

## 5.2 STOKES RELATIONS

Following Stokes (1847) and Longuet-Higgins (1969), we can relate the difference between the net Lagrangian and the net Eulerian displacements to the Stokes drift (Figure 5.2). To obtain this relation, we start with:

$$\vec{v}(\vec{r}, t) = \vec{v}(\vec{r}_0, t) + \int_{t_0}^t \vec{v}(\vec{r}_0, t') \cdot \nabla \vec{v}(\vec{r}_0, t') dt \quad (5.1)$$

where  $\vec{v}(\vec{r}, t)$  is the Lagrangian velocity,  $\vec{v}(\vec{r}_0, t)$  is the Eulerian velocity and the difference between them is the Stokes drift velocity appearing under the integral sign. Here  $\vec{r}_0, \vec{r}$  are the position

vectors of the fluid marker during a time interval between  $t_0$  and  $t$  with  $\vec{\Delta r} = \vec{r} - \vec{r}_0$ . If we assume that  $\vec{\Delta r}$  is small compared to the local spatial scale of the velocity variations, we can write:

$$\vec{v}(\vec{r}, t) = \vec{v}(\vec{r}_0, t) + \vec{\Delta r} \cdot \nabla \vec{v}(\vec{r}_0, t) \quad (5.2)$$

$$\text{and } \vec{\Delta r} = \int_{t_0}^t \vec{v}(\vec{r}_0, t) dt \quad (5.3)$$

from which equation 5.1 follows. To obtain the Stokes velocity relation, we take the mean over the period  $(t-t_0)$ , denoted by an overbar, and write:

$$\overline{\vec{v}(\vec{r}, t)} = \overline{\vec{v}(\vec{r}_0, t)} + \overline{\int_0^t \vec{v}(\vec{r}_0, t) \cdot \nabla \vec{v}(\vec{r}_0, t) dt} \quad (5.4)$$

$$\text{or } \vec{v}_L = \vec{v}_E + \vec{v}_S \quad (5.5)$$

where  $\vec{v}_L$ ,  $\vec{v}_E$ ,  $\vec{v}_S$  are the mean Lagrangian velocity, the mean Eulerian velocity, and Stokes drift velocity, respectively. In Figure 5.2, we have shown the net displacements with  $\vec{L} = \int \vec{v}_L dt$ ,  $\vec{E} = \int \vec{v}_E dt$ , and  $\vec{S} = \int \vec{v}_S dt$ .

Our trajectory calculations can be used to account for the earliest temperature changes observed near the equator about two to three hours after the beginning of the storm (figure 3.2b). These temperature changes could not have been due to the material transport of fluid from the heat source regions. On the other hand, the earliest

equatorial temperature signal accompanies the arrival of the first storm-generated wave. This wave runs ahead of the meridional circulation that gets established behind. Both the waves and the circulation are agents responsible for the descent of air parcels and the consequent heating of the equatorial thermosphere during the storm. This conclusion is consistent with the role of the induced circulation in the equatorial region, discussed in Chapter 4.

FIGURE CAPTIONS FOR CHAPTER V

Fig. 5.1. Trajectory of fluid marker solely due to storm-generated wave disturbances. The marker is started at 70° colatitude and an altitude of 400 km. The numbers 1 to 5 correspond to the beginning times of the five disturbances influencing the fluid marker. Triangles show the locations of the marker at 2-hour intervals. The vector L denotes the net Lagrangian displacement.

Fig. 5.2. Trajectory of the fluid marker under the influence of storm-time waves and meridional circulation started at 257 km and 110° colatitude. a) The Lagrangian trajectory (solid line) is shown during the passage of the first storm-generated wave with the locations of the marker indicated by triangles at 30 minute intervals. In addition, the hypothetical positions of the marker, if it had moved with the mean Eulerian velocity during this interval, are also indicated with asterisks at 30 minute intervals. The vectors L, E, and S are for the net Lagrangian displacement, the net Eulerian displacement, and the Stokes drift, respectively. b) The same trajectories and vectors are shown during the passage of the first two waves. Note that in this case the mean Eulerian velocity is obtained by averaging over two wave periods.

Fig. 5.3. Examples of Lagrangian and Eulerian motions of markers started at 257 km and at colatitudes of 40°, 80°, and 110°. The solid

lines are the Lagrangian trajectories and the dashed lines are the Eulerian trajectories. The asterisks and triangles in these trajectories are at 2-hr intervals. The triangles are labelled for storm-time in hours to aid in following the marker's path. a) For the case with storm-generated waves and circulation alone. b) For the case that also includes the seasonal background meridional circulation.

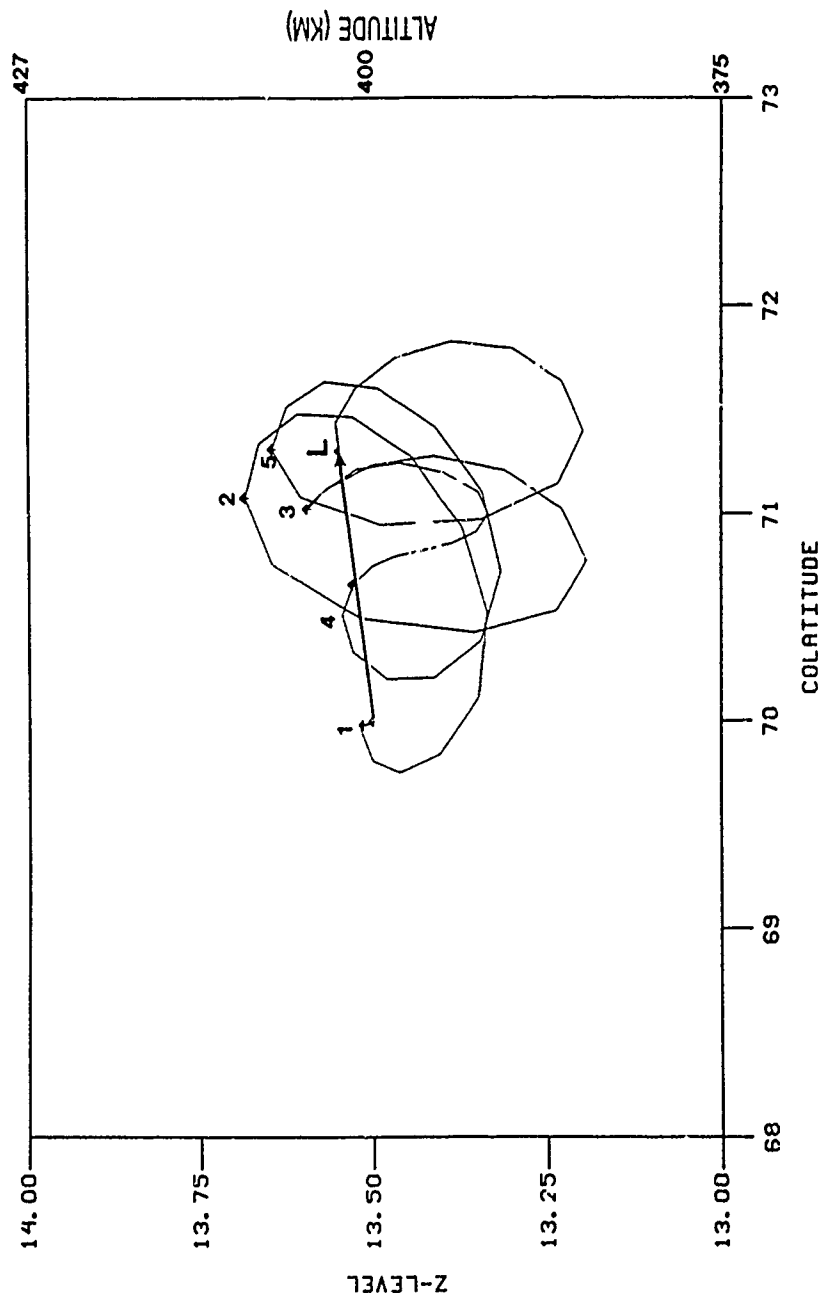


Figure 5.1

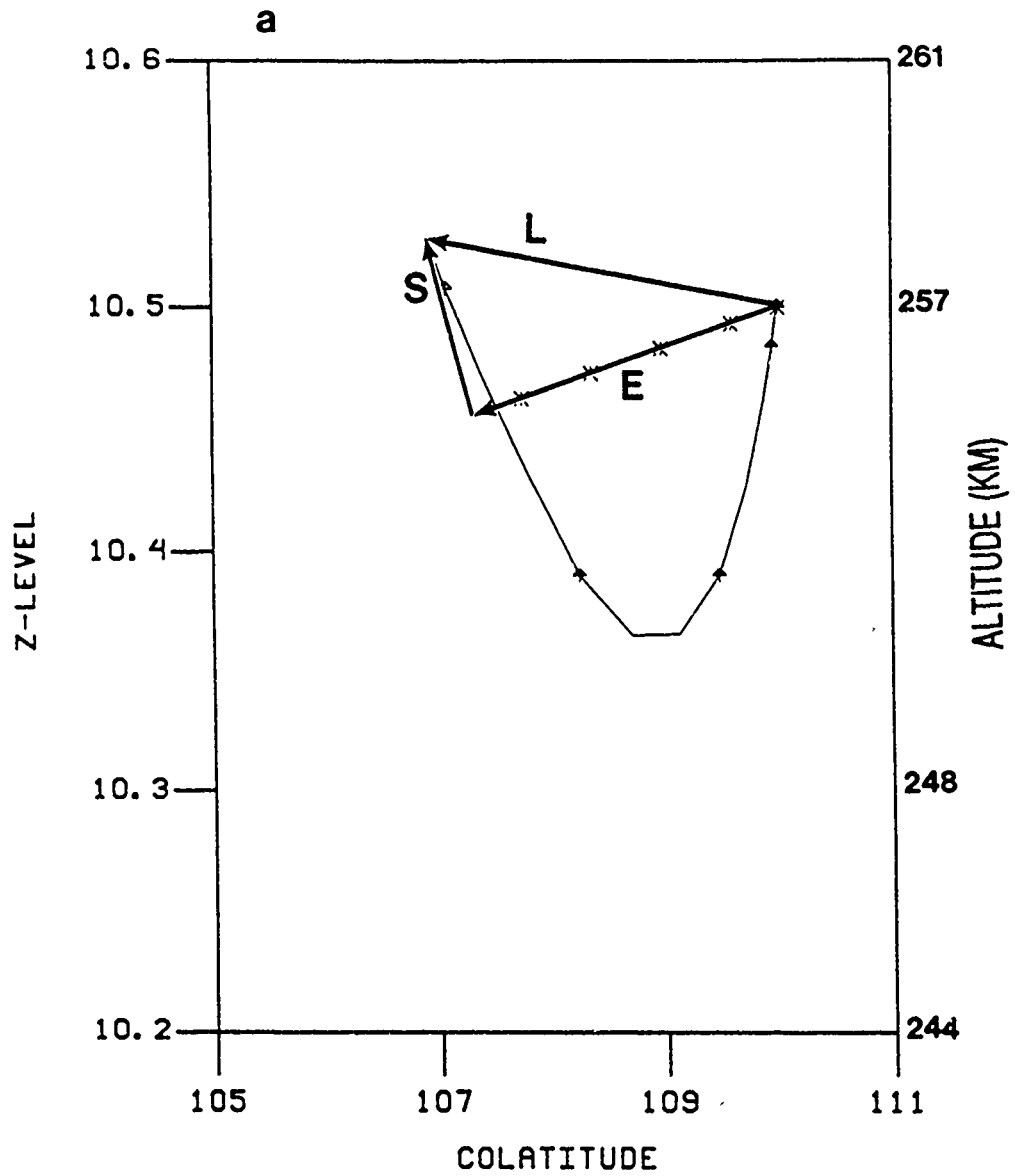


Figure 5.2a

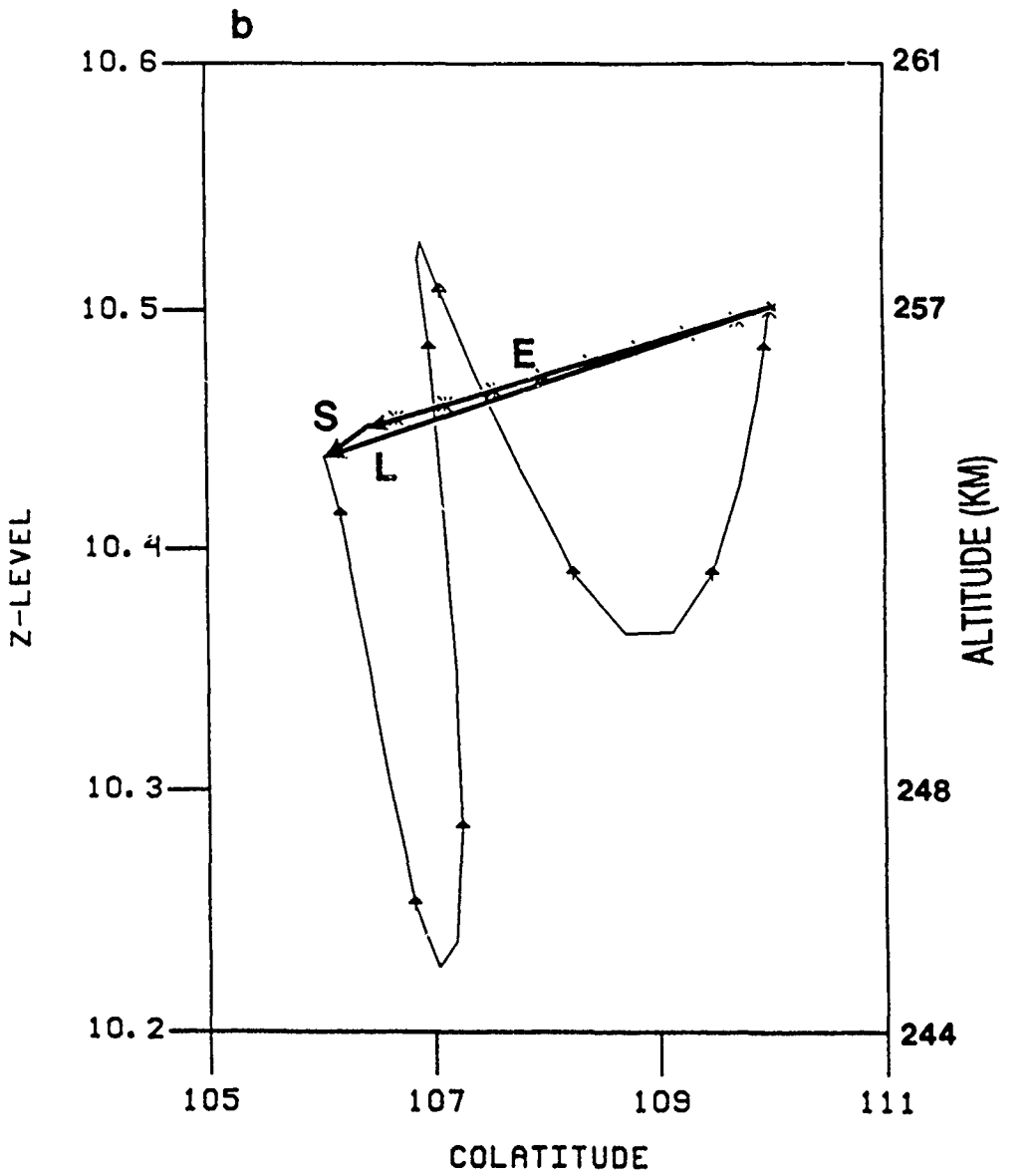


Figure 5.2b

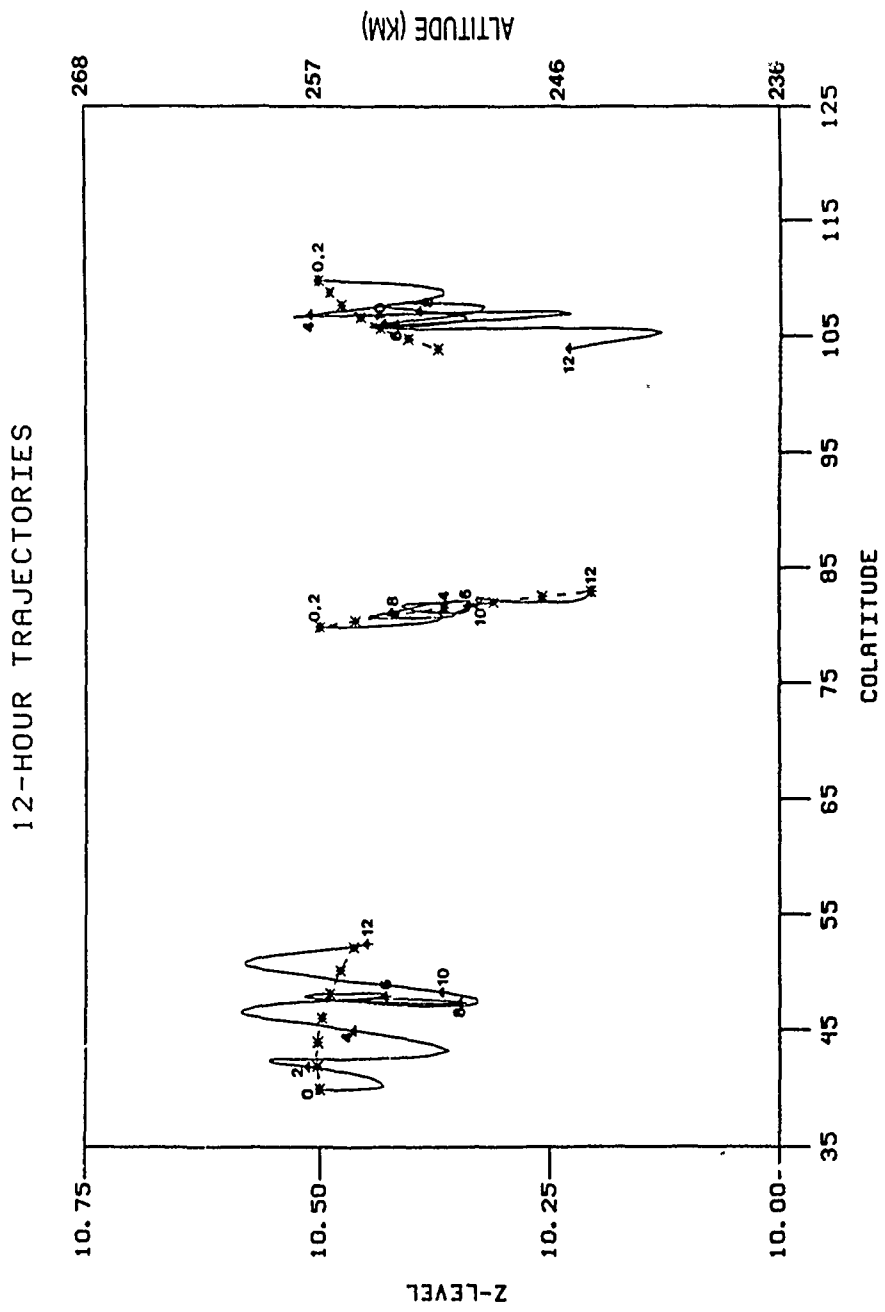
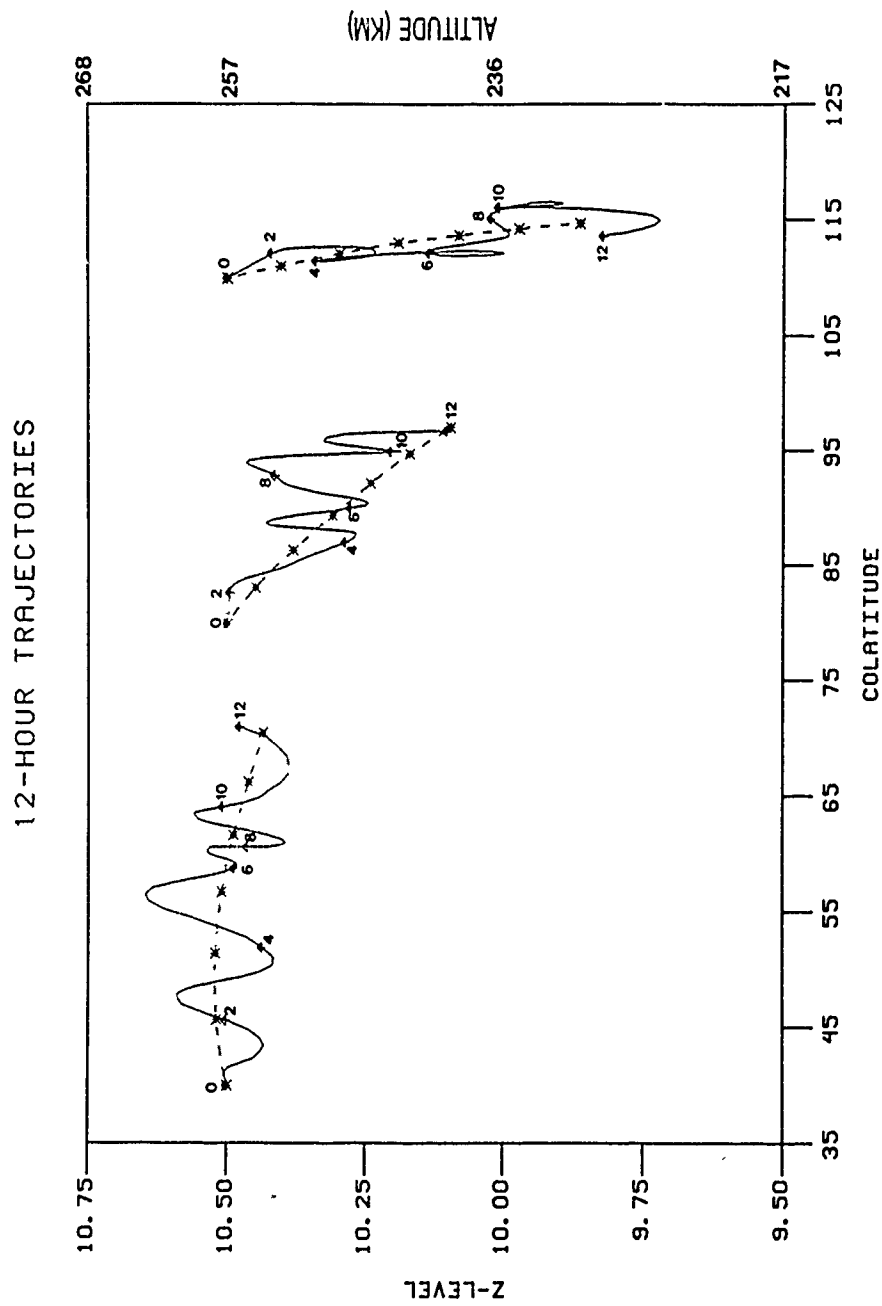


Figure 5.3a



**Figure 5.3b**

## CHAPTER VI

### DISCUSSION AND CONCLUSIONS

In this paper, we have studied the waves and the global meridional circulation generated by a geomagnetic storm. In particular, we have investigated the interaction between the waves and the mean flow using a two-dimensional pole-to-pole model in which the solstitial background winds have been included.

The model storm that we have used consists of a series of substorms which produced four distinct heat pulses lasting through the 12-hour period of storm simulation. Although we have specific examples of such storms, as shown in Figure 2.5a, this type of storm associated with sustained wave activity may not be typical. In another well-documented class of storms, large amplitude waves are generated mainly in the sudden commencement phase (Roble et. al., 1978).

In our model storm, we are able to identify six distinct wave disturbances corresponding to the four pulses in energy input. These wave disturbances are observed to consist of a spectrum of waves which travel equatorward from their sources of origin. When the disturbances are observed to be propagating poleward, their origin can be traced to the opposite hemisphere.

The amplitudes of the disturbances in middle latitudes range between 50-100 m/s in meridional velocity and have a maximum of 7.5 m/s in vertical velocity. Their phase speeds can be as high as 900 m/s. The temperature fluctuations associated with the disturbances are on

the order of 50° K. These wave characteristics are similar to what have been reported from observations (Hernandez and Roble, 1978; Rees et. al., 1984; Roble et. al., 1978).

The apparent periods of the disturbances are found to increase with distance from the wave source, indicating that the disturbances are dispersive. The disturbance amplitudes are reduced and the phase speeds are Doppler-shifted in the direction of the background wind. However, the phase shifts as well as the amplitude reductions are small due to the fact that the phase speeds of the disturbances (450-900 m/s) are large compared to the background wind speeds (10-100 m/s). The phase speeds of the disturbances are also influenced by the temperature

The disturbances tilt with height in a manner consistent with the propagation of energy away from the high-latitude heat source and upward. They are asymmetric in the sense that over a period of the disturbance, the average velocity or net temperature change is not zero. Moreover, the phase relationships between the disturbance parameters are such that over the period of the storm, the net transport of both meridional momentum and heat is equatorward.

The results of the interaction between the waves and the mean flow can be portrayed in terms on the induced circulation. Our results for the induced circulation show that its influence is clearly detectable in the time-averaged equivalent temperature changes due to the storm. In the equatorial region at high altitudes these changes are about 1/4 to 1/3 of the changes due to the mean Eulerian circulation.

The spatial and temporal variations of the storm-time winds are responsible for the difference between the Lagrangian and mean Eulerian trajectories in the storm-time thermosphere. Lagrangian trajectory calculations clearly show that there cannot be material transport of fluid from the source latitudes to the equator. The earliest equatorial motions are induced by storm-generated waves reaching the equator.

## REFERENCES

- Ahn, B., S.-I. Akasofu and Y. Kamide, 1983: The Joule heat production rate and the particle injection rate as a function of the geomagnetic indices AE and AL. *J. Geophys. Res.*, **88**, 6275-6287.
- Andrews, D. G., 1985: Wave, mean-flow interaction in the middle atmosphere. *Adv. Geophys.*, **28**, 249-275.
- \_\_\_\_\_, J. R. Holton and C. B. Leovy, 1987: *Middle Atmosphere Dynamics*, Academic Press, Inc., Orlando, 487 pp.
- Babcock, R. R. and J. V. Evans, 1979: Effects of geomagnetic disturbances on neutral wind and temperatures in the thermosphere observed over Millstone Hill. *J. Geophys. Res.*, **84**, 5349-5354.
- Banks, P. M., 1977: Observations of Joule and particle heating in the auroral zone. *J. Atmos. Terr. Phys.*, **39**, 179-193.
- Blanc, M. and A. D. Richmond, 1980: The ionospheric disturbance dynamo. *J. Geophys. Res.*, **85**, 1669-1686.
- Booker, J.R. and F.P. Bretherton, 1967: The critical layer for internal gravity waves in shear flow. *J. Fluid Mech.*, **27**, 513-539.
- Bretherton, F. P. and C. J. R. Garrett, 1968: Wavetrains in inhomogeneous moving media. *Proc. R. Soc. London Ser.*, **302**, 529-554.
- Buonsanto, M. J., J. E. Salah, K. L. Miller, W. L. Oliver, R. G. Burnside, and P. G. Richards, 1989: Observations of neutral circulation at mid-latitudes during the equinox transition study. *J. Geophys. Res.*, **94**, 16987-16997.

Burnside, R. G., R. A. Behnke, and J. C. G. Walker, 1983: Meridional neutral winds in the thermosphere at Arecibo: Simultaneous incoherent scatter and airglow observations. *J. Geophys. Res.*, **88**, 3181-3189.

Charney, J. G. and P. G. Drazin, 1961: Propagation of planetary-scale disturbances from the lower into the upper atmosphere. *J. Geophys. Res.*, **66**, 83-109.

Crowley, G., B. A. Emery, R. G. Roble, H. C. Carlson, Jr. and D. J. Knipp, 1989a: Thermospheric dynamics during September 18-19, 1984 1. Model simulations. *J. Geophys. Res.*, **94**, 16925-16944.

\_\_\_\_\_, \_\_\_\_\_, \_\_\_\_\_, \_\_\_\_\_, J. E. Salah, V. B. Wickwar, K. L. Miller, W. L. Oliver, R. G. Burnside and F. A. Marcos, 1989b: Thermospheric dynamics during September 18-19, 1984 2. Validation of the NCAR thermospheric general circulation model. *J. Geophys. Res.*, **94**, 16945-16959.

Dickinson, R.E., E. C. Ridley and R. G. Roble, 1975: Meridional circulation in the thermosphere I. Equinox conditions. *J. Atmos. Sci.*, **32**, 1737-1754.

\_\_\_\_\_, \_\_\_\_\_ and \_\_\_\_\_, 1977: Meridional circulation in the thermosphere II. Solstice conditions. *J. Atmos. Sci.*, **34**, 178-192.

\_\_\_\_\_, \_\_\_\_\_ and \_\_\_\_\_, 1980: A three-dimensional general circulation model of the thermosphere. *J. Geophys. Res.*, **86**, 1499-1512.

- \_\_\_\_\_, \_\_\_\_\_ and \_\_\_\_\_, 1984: Thermospheric general circulation with coupled dynamics and composition. *J. Atmos. Sci.*, 41, 205-219.
- Dunkerton, T. J., 1978: On the mean meridional mass motions of the stratosphere and mesosphere. *J. Atmos. Sci.*, 35, 2325-2333.
- \_\_\_\_\_, 1980: A Lagrangian mean theory of wave, mean-flow interaction with applications to nonacceleration and its breakdown. *Rev. Geophys. Space Phys.*, 18, 387-400.
- Francis, S. H., 1975: Global propagation of atmospheric gravity waves: A review. *J. Atmos. Terr. Phys.*, 37, 1011-1054.
- Fuller-Rowell, T. J. and D. Rees, 1981: A three-dimensional, time-dependent simulation of the global dynamical response of the thermosphere to a geomagnetic substorm. *J. Atmos. Terr. Phys.*, 43, 701-721.
- \_\_\_\_\_, and \_\_\_\_\_, 1984: Interpretation of an anticipated long-lived vortex in the lower thermosphere following simulation of an isolated substorm. *Planet. Space Sci.*, 32, 69-85.
- Georges, T. M., 1968: HF doppler studies of traveling ionospheric disturbances. *J. Atmos. Terr. Phys.*, 30, 735-746.
- Gossard, E.E. and W.H. Hooke, 1975: *Waves in the Atmosphere*, Elsevier Sci. Pub. Co., Amsterdam, 97-100.
- Hays, P. B., and R. G. Roble, 1971: Direct observations of thermospheric winds during geomagnetic storms. *J. Geophys. Res.*, 76, 5316-5321.

- Hernandez, G. and R. G. Roble, 1976: Direct measurements of nighttime thermospheric winds and temperatures 2. Geomagnetic storm. *J. Geophys. Res.*, 81, 5173-5181.
- \_\_\_\_\_ and \_\_\_\_\_, 1978: Observations of large-scale thermospheric waves during geomagnetic storms. *J. Geophys. Res.*, 83, 5531-5539.
- \_\_\_\_\_ and \_\_\_\_\_, 1984: The geomagnetic quiet nighttime thermospheric wind pattern over Fritz Peak Observatory during solar cycle minimum and maximum. *J. Geophys. Res.*, 89, 327-337.
- Hines, C. O., 1960: Internal atmospheric gravity waves at ionospheric heights. *Can. J. Phys.*, 38, 1441-1481.
- Hines, C.O., 1968: An effect of molecular dissipation in upper atmospheric gravity waves. *J. of Atmos. and Terr. Phys.*, 30, 845-849.
- \_\_\_\_\_, 1974: *The Upper Atmosphere in Motion*, Geophysical Monograph 18, American Geophysical Union, Washington, D.C., 1027pp.
- Holton, J. R., 1975: *The Dynamical Meteorology of the Stratosphere and Mesosphere*, Meteor. Monogr., No. 37, Amer. Meteor. Soc., 216 pp.
- Hunsucker, R. D., 1982: Atmospheric gravity waves generated in the high-latitude ionosphere: A review. *Rev. of Geophys. and Space Phys.*, 20, 293-315.
- Jacchia, L. G., 1971: Revised static models of the thermosphere and exosphere with empirical temperature profiles. *Spec. Rep. 332, Smithson. Astrophys. Observ.*, Cambridge, Mass.
- Kamide, Y., J.D. Craven, L.A. Frank, B.-H. Ahn, S.-I. Akasofu, 1986: Modeling substorm current systems using conductivity distributions inferred from DE auroral images. *J. Geophys. Sci.*, 103, 11235-11256.

Killeen, T. L., 1987: Energetics and dynamics of the earth's thermosphere. *Reviews of Geophys.*, 25, 3, 433-454.

\_\_\_\_\_, R. W. Smith, P. B. Hays, N. W. Spencer, L. E. Wharton, and F. G. McCormac, 1984: Neutral winds in the high-latitude winter F region: Coordinated observations from ground and space, *Geophys. Res. Lett.*, 11, 311-314.

\_\_\_\_\_, R. G. Roble, R. W. Smith, N. W. Spencer, J. W. Meriwether, Jr., D. Rees, G. Hernandez, P. B. Hays, L. L. Cogger, D. P. Sipler, M. A. Biondi, and C. A. Tepley, 1986: Mean neutral circulation in the winter polar F region. *J. Geophys. Res.*, 91, 1633-1649. Knipp, D.J., 1989: Quantifying and reducing uncertainty in the assimilative mapping of ionospheric electrodynamics, PhD dissertation, University of California, Los Angeles.

Larsen, T. F. and I. S. Mikkelsen, 1983: The dynamic response of the high-latitude thermosphere and geostrophic adjustment. *J. Geophys. Res.*, 88, 3158-3168.

Longuet-Higgins, M. S., 1969: On the transport of mass by time-varying ocean currents. *Deep-Sea Research*, 16, 431-447.

Mazaudier, C., R. Bernard, S. V. Venkateswaran, 1985: Saint Santin radar observations of lower thermospheric storms. *J. Geophys. Res.*, 90, 2885-2895, correction *J. Geophys. Res.*, 90, 6685-6686.

Mazaudier, C., A. Richmond and D. Brinkman, 1987: On thermospheric winds produced by auroral heating during magnetic storms and associated dynamo electric fields. *Annales Geophysicae*, 5, 443-448.

- Killeen, T. L., 1987: Energetics and dynamics of the earth's thermosphere. *Reviews of Geophys.*, 25, 3, 433-454.
- \_\_\_\_\_, R. W. Smith, P. B. Hays, N. W. Spencer, L. E. Wharton, and F. G. McCormac, 1984: Neutral winds in the high-latitude winter F region: Coordinated observations from ground and space, *Geophys. Res. Lett.*, 11, 311-314.
- \_\_\_\_\_, R. G. Roble, R. W. Smith, N. W. Spencer, J. W. Meriwether, Jr., D. Rees, G. Hernandez, P. B. Hays, L. L. Cogger, D. P. Sipler, M. A. Biondi, and C. A. Tepley, 1986: Mean neutral circulation in the winter polar F region. *J. Geophys. Res.*, 91, 1633-1649.
- Knipp, D.J., 1989: Quantifying and reducing uncertainty in the assimilative mapping of ionospheric electrodynamics, PhD dissertation, University of California, Los Angeles.
- Larsen, T. F. and I. S. Mikkelsen, 1983: The dynamic response of the high-latitude thermosphere and geostrophic adjustment. *J. Geophys. Res.*, 88, 3158-3168.
- Longuet-Higgins, M. S., 1969: On the transport of mass by time-varying ocean currents. *Deep-Sea Research*, 16, 431-447.
- Mazaudier, C., R. Bernard, S. V. Venkateswaran, 1985: Saint Santin radar observations of lower thermospheric storms. *J. Geophys. Res.*, 90, 2885-2895, correction *J. Geophys. Res.*, 90, 6685-6686.
- Mazaudier, C., A. Richmond and D. Brinkman, 1987: On thermospheric winds produced by auroral heating during magnetic storms and associated dynamo electric fields. *Annales Geophysicae*, 5, 443-448.

- \_\_\_\_\_, R. E. Dickinson and E. C. Ridley, 1977: Seasonal and solar cycle variations of the zonal mean circulation in the thermosphere. *J. Geophys. Res.*, 82, 5493-5504.
- \_\_\_\_\_, A. D. Richmond, W. L. Oliver and R. M. Harper, 1978: Ionospheric effects of a gravity wave launched by the September 18, 1974, sudden commencement. *J. Geophys. Res.*, 83, 999-1009.
- \_\_\_\_\_, R. E. Dickinson and E. C. Ridley, 1982: Global circulation and temperature structure of the thermosphere with high-latitude plasma convection. *J. Geophys. Res.*, 87, 1599-1614.
- \_\_\_\_\_, \_\_\_\_\_, \_\_\_\_\_, B. A. Emery, P. B. Hays, T. L. Killeen and N. W. Spencer, 1983: The high latitude circulation and temperature structure of the thermosphere near solstice. *Planet. Space Sci.*, 31, 1479-1499.
- \_\_\_\_\_, J. M. Forbes and F. A. Marcos, 1987: Thermospheric dynamics during the March 22, 1979, magnetic storm, I. Model simulations. *J. Geophys. Res.*, 92, 6045-6068.
- Stokes, G. G., 1847: On the theory of oscillatory waves. *Trans. Cambridge Phil. Soc.*, 8, 441-455.
- Testud, J., 1970: Gravity waves generated during magnetic substorms. *J. Atmos. Terr. Phys.*, 32, 1793-1805.
- Walterscheid, R. L. and D. J. Boucher, 1984: A simple model of the transient response of the thermosphere to impulsive forcing. *J. Geophys. Sci.*, 1062-1072.